GROWTH AND CHARACTERIZATION OF WIDE BANDGAP SEMICONDUCTOR OXIDE THIN FILMS

by

Susmita Ghose, B.S, M.S.

A dissertation submitted to the Graduate Council of
Texas State University in partial fulfillment
of the requirements for the degree of
Doctor of Philosophy
with a Major in Materials Science, Engineering, and Commercialization
August, 2017

Committee Members:

Ravi Droopad, Chair

Clois E. Powell

Wilhelmus Geerts

Maggie Chen

Tom Zirkle

FAIR USE AND AUTHOR'S PERMISSION STATEMENT

Fair Use

Duplication Permission

DEDICATION

I would like to dedicate this dissertation to my parents for all the guidance, encouragement and support throughout my life.

ACKNOWLEDGEMENTS

First, I would like to thank and express my deepest admiration to my supervisor Prof. Dr. Ravi Droopad for his continuous support, encouragement, expertise, patience and supervision throughout my PhD research work. I am very grateful to him for allowing me to work in his lab with excellent facilities and giving me an opportunity to explore this research work based on my interest. Without his proper guidance and support, it would not be possible to complete this research work within the time frame.

I am also thankful to Dr. Juan Salvador and Dr. Manuel Caro (post-doctoral scientists of Droopad's research lab) for their initial help, inspiration, guidance and encouragement from the time I joined this research group. I appreciate their patience during the training and teaching on the MBE system as well as various technical scientific discussions. A special thanks to Nate England, Eric Schires and Dr. Casey Smith for their assistance on different technical measurements.

I would also like to acknowledge my colleagues viz. Shafiqur Rahman, Khem Raj Baral from Droopad's research group who collaborated with me for some of the experimental work and data analysis. In particular, I appreciate Shafiq's contribution on the PLD growth. I would like to thank Dr. Robert Klie and Liang Hong from University of Illinois for providing TEM images used in this dissertation.

I would also like to acknowledge the financial support from the Materials Science, Engineering & Commercialization (MSEC) program and doctoral research support fellowship from Texas State University. The program gave me an excellent opportunity to

learn different work ethics that improved my ability be an effective team member. I also want to thank my committee members, Dr. Clois E. Powell, Dr. Maggie Chen, Dr. Wilhelmus Geerts and Dr. Tom Zirkle for their supervision and valuable suggestions.

I am always grateful to my family members for their perpetual motivation, encouragement and blessings for the achievement of my goals. Special thanks to my parents for their continuous supports and keeping faith in me.

TABLE OF CONTENTS

Page

LIST OF TABLES

Table **Page**

LIST OF FIGURES

Figure **Page**

ABSTRACT

Wide bandgap semiconductors are receiving extensive attention due to their exceptional physical and chemical properties making them useful for high efficiency and high power electronic devices. Comparing other conventional wide bandgap materials, monoclinic β-Ga_2O_3 also represents an outstanding semiconductor oxide for next generation of UV optoelectronics and high temperature sensors due to its wide band gap (~4.9eV). This new semiconductor material has higher breakdown voltage (8MV/cm) and n-type conductivity which make it more suitable for potential application as high power electronics. The properties and potential applications of these wide bandgap materials have not yet fully explored. In this study, the growth and characterization of single crystal β-Ga_2O_3 thin films grown on c-plane sapphire (Al_2O_3) substrate using two different techniques; molecular beam epitaxy (MBE) and pulsed laser deposition (PLD) techniques has been investigated. The influence of the growth parameters of MBE and PLD on crystalline quality and surface has been explored. Two methods have been used to grow Ga_2O_3 using MBE; one method is to use elemental Ga and the second is the use of a polycrystalline Ga_2O_3 compound source with and without an oxygen source. Using the elemental Ga source, growth rate of β-Ga_2O_3 thin films was limited due to the formation and desorption of Ga_2O molecules. In order to mitigate this problem, a compound Ga_2O_3 source has been introduced and used for the growth of crystalline β-Ga_2O_3 thin films without the need for additional oxygen since this source produces Ga-O molecules and additional oxygen. Two different alloys $(InGa)_2O_3$ and $(AlGa)_2O_3$ has been grown on c-

plane sapphire substrate by pulsed laser deposition technique to tune the bandgap of the oxide thin films from 3.5-8.6 eV suitable for applications such as wavelength-tunable optical devices, solid-state lighting and high electron mobility transistors (HEMTs).

The crystallinity, chemical bonding, surface morphology and optical properties have been systematically evaluated by a number of *in-situ* and *ex-situ* techniques. The crystalline Ga_2O_3 films showed pure phase of $(\bar{2}01)$ plane orientation and in-plane XRD phi-scan exhibited the six-fold rotational symmetry for β-Ga_2O_3 when grown on sapphire substrate. The alloys exhibit different phases has been stabilized depending on the compositions. Finally, a metal-semiconductor-metal (MSM) structure deep-ultraviolet (DUV) photodetector has been fabricated on β-Ga_2O_3 film grown with an optimized growth condition has been demonstrated. This photodetector exhibited high resistance as well as small dark current with expected photoresponse for 254 nm UV light irradiation suggesting β-Ga_2O_3 thin films as a potential candidate for deep-UV photodetectors. While the grown Ga_2O_3 shows high resistivity, the electrical properties of $(In_{0.6}Ga_{0.4})_2O_3$ and $(In_{0.8}Ga_{0.2})_2O_3$ alloys show low resistivity with a high carrier concentration and increasing mobility with In content.

I. INTRODUCTION

Since the 1950s semiconductor materials have been used for devices and have continued to be used in present-day electronic technology that includes computer microprocessor, solar cells, and power amplifiers among others. Silicon (Si), the second most abundant element, is an inexpensive semiconductor and has properties such as being mechanically strong and non-toxic that makes it suitable for the fabrication of a variety of devices. Due to the evolution of Si-based device technology, it is now possible to make high density miniature transistors on a single piece of silicon; this increases in density is responsible for the present boom in information technology [1]. The increase in transistor density is due to scaling according to Moore's law and has reached the limits of planar device technology. Additionally, a major disadvantage of Si is that it has an indirect bandgap that makes it inefficient in its use for optical devices. Specifically, for opto-electronics devices that includes LED and laser its potential becomes limited due to a low intrinsic quantum efficiency and detection of photons [2], [3]. In addition, Si devices is also limited for high power and high-temperature applications. On the other hand, materials with wide bandgap are more suitable than Si for power devices because of their high breakdown voltage [4], [5]. Moreover, direct bandgap materials would make efficient opto-electronic devices with the wavelengths that depends on the bandgap.

Wide bandgap semiconductors such as GaN, SiC can be used in heterostructures with similar alloys to fabricate high power electronics due to their exceptional physical and chemical properties [6], [7] and because of their direct bandgaps, are becoming important for making optical devices for white light illumination, color displays, blue-violet laser diodes and UV or deep UV light sources with high efficiency and larger breakdown voltage

compare to devices made from silicon [8], [9]. Another promising field for wide bandgap semiconductor is in the electronic industry that requires device operating at high frequency and high power as well as under extreme environment [8]. Since high-quality SiC and GaN substrates are expensive, power devices based on these materials are not favorable to mass production opening the possibility for new materials to enter into the market [9].

Recently transparent conducting oxides (TCOs) have attracted strong attention due to their important electrical and optical properties [10]. The term "Transparent Conducting Oxide" originated from the unique combination of high transparency and electrical conductivity properties. Typically, materials having low electrical resistivity (10^{-4}-10^{-7} Ω cm) are not able to transmit visible light while most of the transparent materials have high electrical resistivity (>10^{10} Ω cm) act as electrical insulators. Hence, a single material with a combination of both of these properties becomes very unique and can be used to develop transparent optoelectronic devices. TCOs can be divided into two different classes and those are (i) wide band gap TCOs (WB-TCO), and (ii) narrow band gap TCOs (NB-TCO) (Fig. 1.1) [11].

WB-TCOs such as ZnO and SnO_2 have large band gaps (>3 eV), which give these materials transparencies to visible light. By doping these materials extrinsically, electron carrier concentrations can be modified which changes their intrinsic n-type conductivity [12]. In contrast, stoichiometric NB-TCOs are not transparent. However, a blue-shift of their optical band gap, E_{opt}, can be induced by means of doping providing optical transparency (Fig. 1.1). This interesting phenomenon is known as the Moss–Burstein effect [13].

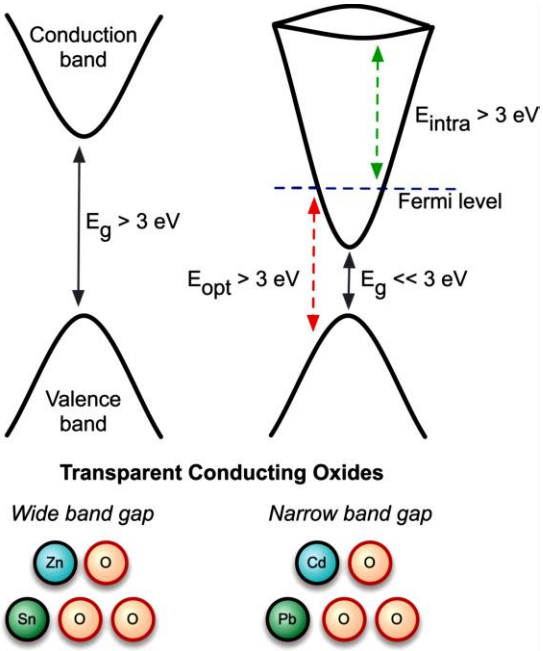

Figure 1.1: Schematic diagram of different TCOs: (a) Wide bandgap TCOs, (b) Narrow bandgap TCOs, where the Fermi level denotes the electron chemical potential for highly doped n-type materials [11].

Besides electrical conductivity and optical transparency, TCOs can extend their functionality incorporating additional properties such as photoconductivity, dielectric constant, catalysis, and electronic structure. This flexibility makes TCOs very attractive and promising materials for diverse applications such as flat-panel displays, optical windows, high temperature chemical gas sensors, and dielectric layers [10], [14]. Much effort is currently being paid by researchers to further understand and optimize known TCOs. There is a need to also develop other novel materials with desired characteristics, viz, high mobility, indium-free materials, p-type materials at a lower cost. Moreover, over the past decade there has been considerable interest on TCOs for diodes and transistors because of applications in flexible and transparent electronics. An amorphous oxides with high electron mobility helps to overcome the shortcomings concerning energy efficiency and cut-off frequencies of amorphous silicon but it is expected that crystalline materials

will result in higher mobilities [15].

However, while most of the transparent conductive oxides such as In_2O_3, SnO_2, ZnO and ITO are useful for numerous applications, their small band gaps (~3eV) are not suitable for opto-electronic devices operating in the UV wavelength region [10] representing a significant limitation in this field. Gallium oxide (Ga_2O_3) represents an outstanding transparent semiconductor oxide which is considered to possess the widest bandgap (~4.9eV) among the TCOs making it highly transparent from the visible to UV wavelengths [4], [9]. Ga_2O_3 has five different crystal structures with the most stable being the β phase. A comparison on important properties of materials between major semiconductors and β-Ga_2O_3 has been shown in Table 1.

Table 1: Material properties of important semiconductors and β-Ga_2O_3 [16].

	Si	**GaAs**	**4H-SiC**	**GaN**	**Diamond**	**β-Ga_2O_3**
Bandgap, E_g (eV)	1.1	1.4	3.3	3.4	5.5	~4.9
Electron mobility, μ ($cm^2V^{-1}S^{-1}$)	1400	8000	1000	1200	2000	300
Breakdown field, E_b ($MVcm^{-1}$)	0.3	0.4	2.5	3.3	10	8
Relative dielectric constant, ε	11.8	12.9	9.7	9.0	5.5	10
Baliga's FOM, $\varepsilon\mu E_b^3$	1	15	340	870	24664	3444
Thermal conductivity ($Wcm^{-1}K^{-1}$)	1.5	0.55	2.7	2.1	10	0.23 [010] 0.13 [100]

The plot in fig. 1.2 (a) shows the breakdown electric field of important materials as a function of their bandgap. From interpolation of the relationship between bandgaps and breakdown electric fields, β-Ga_2O_3 is expected to have a breakdown electric field of 8 MV/cm, which is higher than Si, GaN or SiC, the conventional semiconductor materials

for high-power device applications [16]. Because of this characteristic the use of β-Ga_2O_3 is progressing significantly in the high-power electronics field. Fig 1.2 (b) shows a plot of the theoretical limits of on-resistances vs. breakdown voltage calculated from the given parameters in Table 1 for well-known materials. This indicates that with the same breakdown voltage, β-Ga_2O_3 devices can exhibit lower on-resistance, and thus lower conduction loss compared to Si, SiC, and GaN devices [16].

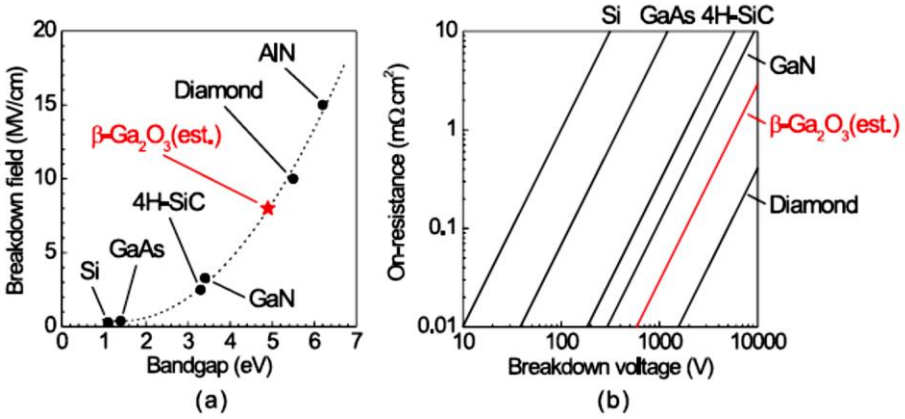

Figure 1.2: (a) Breakdown field as a function of bandgap, (b) theoretical limits of on-resistances vs. breakdown voltage plot for conventional semiconductors and β-Ga_2O_3 [16].

Additionally, the Baliga figure of merit (BFOM) of β-Ga_2O_3 is higher than that of 4H-SiC and GaN with an expected maximum bulk electron mobility of 300 cm^2/Vs. The BFOM corresponds to the lowest specific on-resistance of a vertical electronic device which makes β-Ga_2O_3 an excellent candidate for low loss, high-voltage switching applications such as high-breakdown Schottky diodes and field-effect transistors [16].

β-Ga_2O_3 based field-effect transistors (FETs) and Schottky barrier diodes have been studied by various group [9], [16]–[18]. Higashiwaki *et al.* [16] has reported on the fabrication of metal oxide semiconductor FETs (MOSFETs) and metal semiconductor FETs (MESFETs) on (010) β-Ga_2O_3 substrate [16]. They revealed good characteristics of

the transistor operation including a high on/off ratio (~10^4) and a high breakdown voltage of 370 V. Schottky barrier diodes has been fabricated by Sasaki *et al.* [19] where a Pt contact was used on the (010) β-Ga_2O_3 crystal. They demonstrated a breakdown voltage of ~150 V, an ideality factor close to unity and a Schottky barrier height of 1.3-1.5 eV [17]. Ga_2O_3 is predicted to be a superior power device material than SiC and GaN in terms of device performance as well as cost effectiveness [9].

Another important feature of β-Ga_2O_3 is the possibility of fabricating large single-crystal β-Ga_2O_3 substrates using melt-growth methods including float-zone (FZ) and edge-defined film-fed growth (EFG) [20], [21]. It is thus more suitable for low-cost mass production at lower energy consumption than producing SiC and GaN wafers since these cannot be grown by melt growth but requires much more expensive and complicated growth processes. This is an important advantage of Ga_2O_3 over conventional wide bandgap semiconductors such as SiC, GaN, and diamond for the mass production of power devices [22], [23].

In addition, depending on the growth conditions, it is possible to vary the Ga_2O_3 conductivity from insulator to conductor [24] making it more suitable for prospective applications in luminescent phosphors, high temperature sensors, antireflection coatings, and UV optoelectronics [10]. Recently, UV photodetectors have become very important because of their wide applications including various commercial and military applications for space and astronomical research, missile launch detection, UV radiation calibration and monitoring, environmental monitoring, and optical communication [25], [26].

In the field of DUV photodetectors, other wide bandgap materials such as AlGaN, ZnMgO, diamond have recently been used but the shortcomings such as rigorous growth

methods, low-crystalline quality, low responsivity (<1A/W), low external quantum efficiency (EQE) (~10%) and higher dark current of these materials limit the utilization of these devices [27], [28]. Because of its wide bandgap of ~4.9 eV, Ga_2O_3 represents a promising candidate for UV photodetector technology allowing it to be used in the solar-blind spectrum region. Higher thermal stability, and intrinsic solar blindness have also been demonstrated using Ga_2O_3 because of its high breakdown electric field [4]. This chemically and thermally stable transparent semiconductor oxide exhibits lower dark current which is a major requirement for UV photodetectors [4]. Guo, *et al.* have demonstrated a prototype photodetector device based on β-Ga_2O_3 films with a metal-semiconductor-metal structure on (0001) Al_2O_3 substrates with the Ga_2O_3 layer grown by molecular beam epitaxy [27]. Expected photoresponse under 254 nm UV light irradiation has been exhibited by such device further indicating β-Ga_2O_3 as a potential candidate for solar-blind photodetectors [27].

The objective of this thesis is to study the growth and properties of wide bandgap transparent conducting oxide, β-Ga_2O_3 thin film as a promising candidate for high power semiconducting device and opto-electronic device application. The optimization of the growth conditions to improve β-Ga_2O_3 properties is critical to the development of this technologically important class of material. The outcome of this study will increase the understanding of this material. Epitaxial single crystal β-Ga_2O_3 thin films will be grown on c-plane (0001) sapphire substrate by PAMBE method using two different sources with oxygen plasma: a compound Ga_2O_3 source material and the second using an elemental Ga. The properties of the Ga_2O_3 films, including chemical composition, optical properties, and surface morphology, will be investigated and compared between these two MBE growth

methods. Additional studies will be carried on layers grown using pulsed laser deposition (PLD) technique. Detail growth and characterization of wide bandgap oxide alloys such as $(InGa)_2O_3$ and $(AlGa)_2O_3$ will be developed by the PLD technique. The development of alloy growth will enable the tunability of the bandgap and the fabrication of high electron mobility device structures.

1.1 Literature Review

1.1.1 Crystal Structure of Ga_2O_3

Ga_2O_3 can be crystallized in five different structures and those are α, β, γ, δ and ε phases. Among them the monoclinic β-Ga_2O_3 phase is the most chemically and thermally (melting point at 1780°C) stable structure which is the most appropriate for device applications [10]. Corundum structure α-Ga_2O_3 is the second metastable polymorph that is stable at lower temperature when deposited on sapphire substrates [29]. It has been reported that the heteroepitaxial growth of defective-spinel structure γ-Ga_2O_3 thin films is possible [30]. The metastable crystalline phase formation strongly depends on the substrate lattice and growth temperature. Usually, for β-Ga_2O_3 thin films formation, high growth temperatures are required for both homoepitaxial and heteroepitaxial growth on foreign substrates [22]. This research is mostly focused on β-Ga_2O_3 thin films. The lattice parameters of monoclinic β-Ga_2O_3 are a =12.23Å, b=3.04Å, and c=5.80Å with a lattice angle β =103.7° and space group C2/m [22].

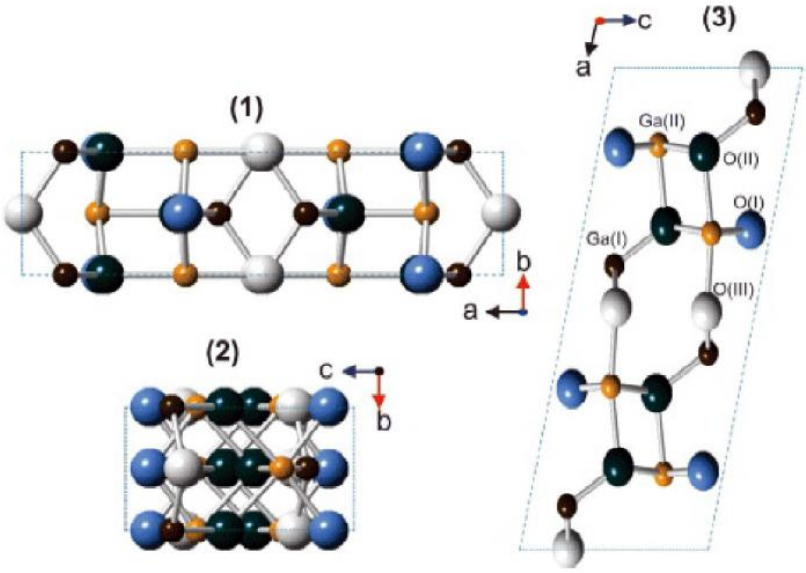

Figure 1.3: Unit cell of β-Ga_2O_3. It has two inequivalent Ga sites: Ga(I), Ga(II) and three inequivalent O-sites: O(I), O(II) and O(III). Illustrated the projection of β-Ga_2O_3 unit cell along the c-(1), a-(2) and b-axis (3).

Figure 1.3 shows the unit cell of β-Ga_2O_3. There are two crystallographically inequivalent Ga positions, one with tetrahedral geometry Ga (I) and another with octahedral geometry Ga (II). The arrangement of oxygen ions is in a "distorted cubic" closed packing array. It contains three crystallographically different locations signified as O(I), O(II) and O(III), respectively. One is coordinated tetrahedrally and two oxygen atoms are coordinated trigonally [31]. Average interionic distances are: tetrahedral Ga-O, 1.83 Å; octahedral Ga-O, 2.00 Å; tetrahedron edge O-O, 3.02 Å; and octahedron edge O-O, 2.84 Å [32].

Kohn *et al.* [33] reported the lattice parameters of the β polymorph of Ga_2O_3, and Geller [32] determined that the structure in space group C2/m. It was concluded with the support of the Negative tests for piezo- and pyroelectricity that, C2/m was the most feasible space group for the crystal. Lower morphological symmetry of the β-Ga_2O_3 crystals than

that of the established point group 2/m was pointed out by Walton and Chase [34] and supported by optical and SEM studies. According to their suggestion, the crystal cell of β-Ga_2O_3 has the pseudo symmetrical triclinic structure with the proper space group P1. However, other scientists who were working in this field questioned this conclusion because numerous investigations had been carried on β-Ga_2O_3 crystals where no deviation had been found from the monoclinic structure of this crystal. Hence, if there is any deviation from the more symmetric structure, certainly that must be an insignificant deviation [31].

Ahman *et al* [35] published the latest and precise study on the crystal structure of β-Ga_2O_3. Although there is a small difference in the results from the previously published data of Konh [33] and Geller [32], the accuracy of that study was almost ten times more appropriate than in the previous works. There is a clear indication of a C-centered monoclinic cell which has space group C2/m according to X-ray diffraction symmetry and systematic extinctions. In contrast, no additional enhancement has been reported on the improvement of the structure in space group P1 [31].

1.1.2 Material Properties of β-Ga_2O_3

The β-phase is the most well-studied and familiar polymorph of gallium oxide with the reported bandgap of ~4.9 eV. For this phase, a relatively easy and most recognized technology is n-type doping. In Ga_2O_3, Sn and Si atoms are identified as shallow donors which have small activation energies. Controlled doping results in the wide range of electron densities (n) of 10^{15}-10^{19} cm^{-3} [36], [37]. In contrast, effective hole conduction in Ga_2O_3 has not been reported so far. Acceptor atoms with a small activation energy is difficult to find out because of the wide bandgap of Ga_2O_3. Moreover, first principles

calculation of the Ga_2O_3 band structure predicted a very small effective p-type conductivity in Ga_2O_3 due to a very limited hole mobility [38]. Nevertheless, in the worst condition, tight localization of holes at definite positions in bulk Ga_2O_3 was also expected [39]. Ga_2O_3 thermal conductivity shows a strong dependence on the crystal orientation because of its crystal structure asymmetry shown in figure 2.1. In the [010] direction, the maximum thermal conductivity (22.8W $(m\ K)^{-1}$) is two times higher compared to the [100] direction. However, the thermal conductivity of Ga_2O_3 in the [010] direction is still much lower compared to other semiconductors [22]. Basic properties of β-Ga_2O_3 are reported in Table 2.

Table 2: Basic properties of β-Ga_2O_3 material [31].

Property	**Value**
Direct Bandgap	~4.9eV
Melting point	1725°C
Dielectric constant	6.5-7.6
Refractive index	1.97
Thermal conductivity	[100]: 13.6W/mK [010]: 22.8W/mK [$\bar{2}$01]: 13.3±1.0W/mK
Density	$5.95\times10^3 kg/m^3$
Specific heat capacity	$0.49\times10^3 J/kgK$

For $n=10^{15}$-10^{16} cm^{-3}, bulk electron mobility of Ga_2O_3 can be obtained by the extrapolated experimental results which is a comparatively large value of about 300 $cm^2V^{-1}s^{-1}$ and vertical power transistors and diodes usually uses that for the drift layers [40]. There is an agreement of this relatively high mobility of β-Ga_2O_3 with theoretical calculations which reveals its electron effective mass is 0.23-0.34m_o (m_o: free electron

mass) comparable with those of typical wide bandgap (3-4 eV) semiconductors [9].

1.1.3 Growth Method and Defect Structure of β-Ga_2O_3

To fabricate the β-Ga_2O_3 thin films, various techniques have been used to date including plasma-enhanced atomic layer deposition [41], sputtering [42], chemical-vapor deposition (CVD) [43], metalorganic CVD [44], molecular-beam epitaxy (MBE) [16], pulsed laser deposition (PLD) [45] and plasma-assisted MBE (PAMBE) [46], [47]. This research will be focused on MBE technique which is mostly used for single crystalline β-Ga_2O_3 growth. Additional studies will be carried using pulsed laser deposition.

MBE is well-known for providing an ultrahigh vacuum atmosphere and highly pure source materials to significantly diminish the impurity levels of the films grown by this technique. Usually, to provide Ga and dopant (Si, Sn) fluxes typical Knudsen effusion cells are used. Pure oxygen is not efficient since practically all oxygen molecules desorb [31]. Hence, two other sources are used including RF plasma [46], [47] or ozone [40] sources. The advantage of the ozone MBE technique is a higher growth rate up to 0.7 μm/hr [40]. However, in Ga_2O_3 (010) films it is difficult to precisely control the densities of the intentional doping since the background pressure (>10^{-4}Torr) is high [31]. Also, the growth rate depends on the crystallographic orientation. The Ga_2O_3 growth rate on the (100) plane was reported by Sasaki *et al.* [40] with the value of one-tenth of that on the (010) and (310) planes.

Plasma assisted molecular beam epitaxy (PAMBE) represents an appropriate technology for the growth of high quality β-Ga_2O_3 single crystalline thin films, because it is well known for: (1) the reduction of the film impurity levels with an ultrahigh vacuum environment using high purity source materials and (2) in situ monitoring of atomic-layer

growth by reflection high energy electron diffraction (RHEED). The lower unintended impurity levels in the epitaxial films allow for the investigation of the unexplained conduction mechanism with reproducible doping control through the improvement of the crystalline quality [10], [47]. The maximum growth rate of the Ga_2O_3 films grown by PAMBE has been reported as 132 nm/hr [31].

Pulsed laser deposition (PLD) technique is one of the promising technique for the growth of Ga_2O_3 thin films and the usage of this technique is increasing in recent days for Ga_2O_3 growth because it provides consistent composition of target to the grown film completely with high kinetic energies of ablated species. Another advantage of using PLD technique for oxide growth is having the ability to use wide variety of gases with high background pressure to provide stoichiometry composition. Fei-Peng *et al.* [48] fabricated a solar-blind photodetector based on Ga_2O_3 grown by PLD at various substrate temperatures (400 to 1000 °C) on sapphire substrate. They investigated the structural, optical and electrical properties of the grown thin films and found that, the crystallinity is influenced by the substrate temperature with the film grown at 800°C showed higher crystal quality compare to those grow at low temperature. The ratio of oxygen to gallium in the thin films is increased with increasing the substrate temperature from 800 to 1000°C indicated reduced oxygen vacancies and defects. Therefore, their fabricated device showed better performance with the substrate temperature of 800°C. Growth rate of the PLD grown Ga_2O_3 is higher than that of MBE with lower substrate temperature because the ablated species have high kinetic energy [49]. When the Ga_2O_3 thin film are deposited by PLD technique, the growth is also influenced by the oxygen pressure and they showed a rapid change in the surface morphologies and roughness of Ga_2O_3 with increasing oxygen

pressure [50].

In prior reports, a variety of substrates including glass, quartz, Si, GaAs, BeO, and sapphire (Al_2O_3) were used to deposit β-Ga_2O_3. Among them, sapphire exhibits the smallest lattice mismatch while providing an electrically insulating substrate which is also transparent into the deep UV [10].

It has been reported that monoclinic β-Ga_2O_3 films can be grown epitaxially on sapphire along different directions including (0001), $(11\bar{2}3)$ and $(11\bar{2}0)$ and their epitaxial relationship are [51]:

$(20\bar{1})$ β-Ga_2O_3 || (0001) $A1_2O_3$
(310) β-Ga_2O_3 || $(11\bar{2}3)$ $A1_2O_3$
$(\bar{1}12)$ β-Ga_2O_3 || $(11\bar{2}3)$ $A1_2O_3$
(111) β-Ga_2O_3 || $(11\bar{2}0)$ Al_2O_3

} <132> β-Ga_2O_3 || $<1\bar{1}00>$ Al_2O_3

Schematically a projected geometrical epitaxial relationship has been reported [27] among the $(\bar{2}01)$ plane of β-Ga_2O_3 thin film and the (0001) Al_2O_3 substrate which is shown in figure 1.4 (a). The arrangement of oxygen atoms in the c-plane (0001) plane of sapphire substrate is the same as in the $(\bar{2}01)$ plane of β-Ga_2O_3. Moreover, it is shown that, four lattice planes of β-Ga_2O_3 in the [010] direction are closely matched with three lattice planes of Al_2O_3 in the $[01\bar{1}0]$ direction, and two lattice planes of β-Ga_2O_3 in the $[\bar{2}01]$ direction are closely matched with three lattice planes of Al_2O_3 in the $[2\bar{1}\bar{1}0]$ direction [52]. By the domain variation principle, the lattice mismatches are found to be −1.6% and + 3.13% respectively. So that, gallium "does not feel" any difference when making bonds to the oxygen atom layer between the Al_2O_3 (0001) and the β-Ga_2O_3 $(\bar{2}01)$ during the formation of β-Ga_2O_3 on the Al_2O_3 (0001) substrate which suggests the growth mode to be domain matching epitaxy [27].

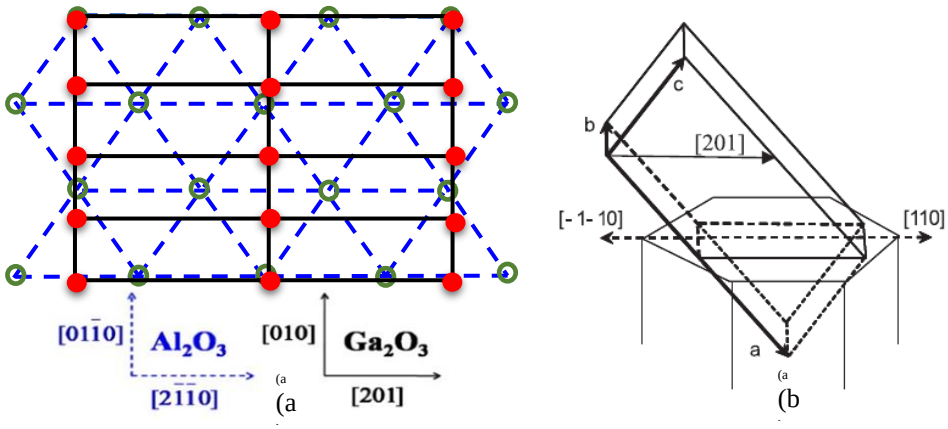

Figure 1.4: (a) Schematically projected geometrical epitaxial relationship among the ($\bar{2}$01) plane of β-Ga_2O_3 thin film and the (0001) Al_2O_3 substrate. The film and substrate lattices are intentionally offset a little for clarity, (b) positional relation among the unit cell of β-Ga_2O_3 and sapphire recognized as hexagonal cylinder. β-Ga_2O_3($\bar{2}$01) plane is parallel to the (0001) sapphire.

Figure 1.4 (b) shows that the [$\bar{2}$01] β-Ga_2O_3 direction is vertical to the sapphire {100} planes resulting in six crystal types depositing on the c-plane (0001) sapphire and from the [1$\bar{1}$0] direction rotated 60° each. The arrangement of oxygen atoms on the substrate surface is very influential for the β-Ga_2O_3 crystal orientation when growing on Al_2O_3 (0001) indicating the highly precise crystalline growth of β-Ga_2O_3 thin film on Sapphire (0001) [53].

Figure 1.5 (a) and (b) shows cross-sectional high resolution transmission electron microscopy (HRTEM) images of β-Ga_2O_3 film grown on sapphire substrate and their correlated electron diffraction pattern respectively. The enlarged view (Figure 1.5 (a) inset) of HRTEM image shows the interplanar spaces which correspond to the characteristic d-spacing of the β-Ga_2O_3 ($\bar{2}$01) film plane (~0.47 nm) [54]. It is also clear from this figure that no structural defects and dumbbell interstitials is detected in epitaxial β-Ga_2O_3 thin films indicative of excellent crystallinity of the β-Ga_2O_3 films [4], [55].

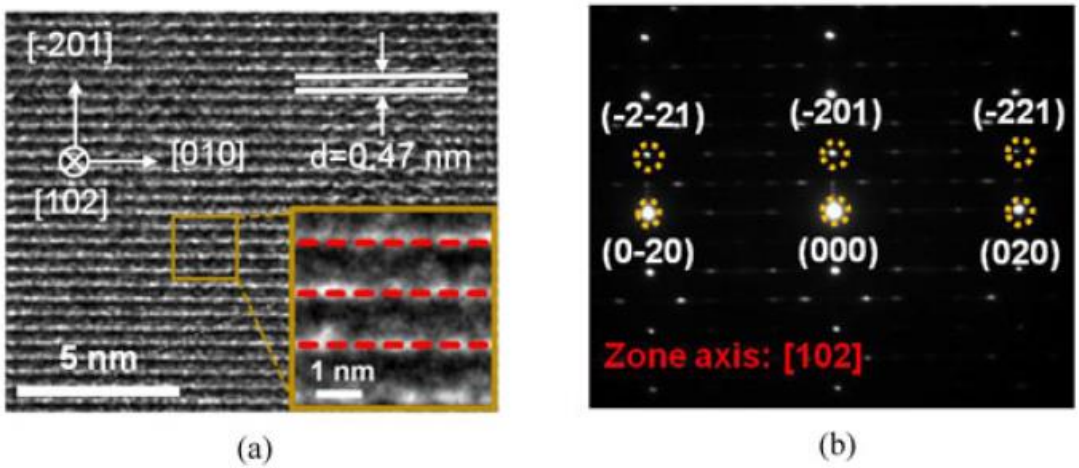

Figure 1.5: (a) HRTEM cross-sectional images of the β-Ga_2O_3 deposited on a sapphire substrate. The inset displays an enlarged portion of the HRTEM image. (b) Corresponding electron diffraction patterns of the β-Ga_2O_3 films [4].

1.1.4 Conductivity Control and Doping

An important condition for a semiconductor device usage is substitutional doping. In most cases, doping of both n-type and p-type polarities are vital. The success of doping any material with given polarity requires three conditions [56];

- The dopant solubility in the lattice
- The dopant level shallowness
- Compensation lacking of the dopant by an intrinsic defect

In another way, the intrinsic defect (the vacancy) formation energy can be expressed as a function of the Fermi energy (E_f) [57]:

$$\Delta H\left(E_f\right) = qE_f + \Delta E$$

Where ΔH is the formation energy. From this relationship, there might be a Fermi energy at which the defect formation energy is zero, as shown in figure 1.6. If a dopant is able to shift the Fermi level to this specific energy, referred to as the pinning energy, hence

vacancies will be created spontaneously [56].

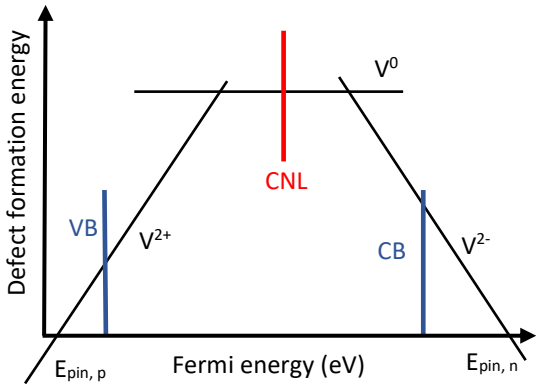

Figure 1.6: The doping pinning levels principle for n and p-type dopants upon the band diagram. The semiconductor can be doped when the pinning level located inside the bands; the semiconductor cannot simply be doped when it falls in the gap [56].

For n-type and p-type doping, there is a corresponding pinning energy (denoted by $E_{pin,\,n}$ and $E_{pin,\,p}$). In thermodynamic equilibrium, it will not be possible to move the Fermi level further away from these two pinning energies. When the pinning energies are located in the valence or conduction band (not into the gap), then doping is possible. It is worth noting that, defect compensation will be different for n-type and p-type doping [56].

Excellent n-type conductivity has been shown for β-Ga_2O_3 when fabricated with specific conditions. The n-type semiconductivity is typically attributed to oxygen vacancies. The Ga_2O_3 crystals fabricated by floating zone technique exhibits controlled conductivity by using doping atoms or by changing the gas ambient [31]. Ueda and Hosono et. al. [37] reported that depending on the amount of oxygen during the growth, Ga_2O_3 crystal showed controlled conductivity from 10^{-9} to 38 $\Omega^{-1}cm^{-1}$ [31].

Due to the dependency of the conductivity of β-Ga_2O_3 crystals on the partial

pressure of oxygen in growth or annealing atmospheres, existence of oxygen vacancies is required for n-type conductivity [31] although Varley and co-workers [38] have questioned this assumption. Considering the hybrid functional theory of oxygen vacancies and several impurities in the β-Ga_2O_3, they conducted first-principle calculations which revealed that, oxygen vacancy cannot lead to n-type conductivity because it acts as a deep donor whose ionization energy is above 1 eV. Authors proposed that, the reason for increased electrical conductivity is hydrogen in β-Ga_2O_3 which is an unintentional doping as shown in figure 1.7 [38].

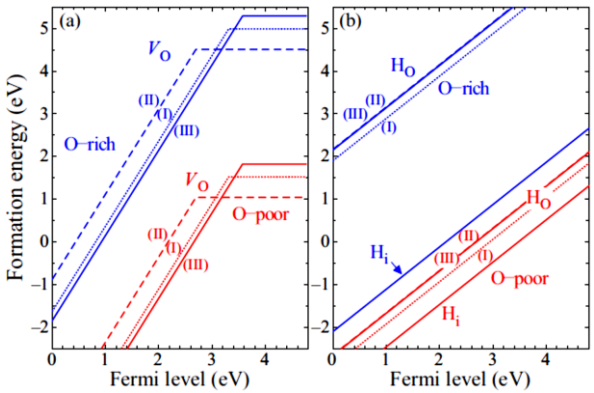

Figure 1.7: Formation energy is plotted as a function of Fermi level for the oxygen vacancy (a) and H impurities (b) in β-Ga_2O_3. O-rich and O-poor conditions values are shown. The labels (I), (II), and (III) denote the three inequivalent O sites [38].

The use of different elements for doping is possible affecting the concentration of free electrons and electrical conductivity. For example, Ga site can be substituted by group IV elements (Si, Ge and Sn) or O site can be substituted by group VII elements (Cl and F) playing as shallow donors (figure 1.8) [38]. Si and Ge have preference to the Ga(I) site tetrahedral coordination and Sn has preference to the Ga(II) site octahedral coordination. F and Cl both have preference to the O(I) site threefold coordination [31].

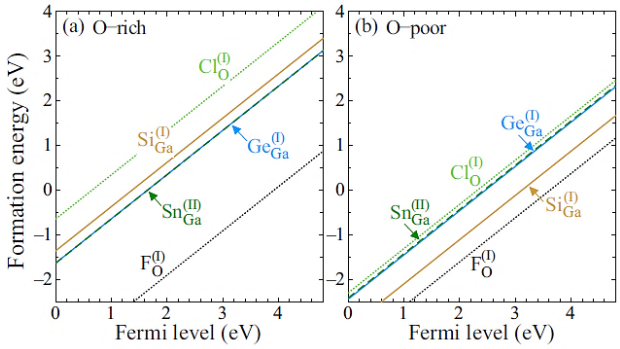

Figure 1.8: Formation energy is plotted as a function of Fermi level for several shallow donor impurities in β-Ga_2O_3 under (a) O-rich and (b) O-poor conditions. The labels (I) and (II) denote to the inequivalent Ga or O sites; the lowest-energy site results are shown only [38].

Suzuki *et al.* [58] and Ueda *et al.* [37] reported the effects of Sn doped Ga_2O_3 crystals grown by Float-Zone method. Float-Zone method grown Ga_2O_3 crystal exhibited high conductivity when Ga_2O_3 rods were doped with Sn (2-10 mol.%). It has been reported that, conductivities of 0.96 $\Omega^{-1}cm^{-1}$ and 56 $\Omega^{-1}cm^{-1}$ with mobility in the range of 50-100 cm^2/Vs were found while producing the crystal under oxygen environment [37], [58]. SnO_2 doped Ga_2O_3 crystals exhibited blue coloration [37]. K. Sasaki *et al.* [40] reported on ozone MBE grown Sn doped Ga_2O_3 films. Ga metal and SnO_2 powder heated in normal Knudsen cells were used to evaporate Ga and Sn in an MBE system with a mixture of ozone (5%)-oxygen (95%) gas used as the oxygen source. Semi-insulating (010) Ga_2O_3 substrate doped with Mg was used to grow a 0.7 μm thick Sn doped Ga_2O_3 film. By changing the temperature of the SnO_2 K-cell, the carrier concentration of the grown β-Ga_2O_3 epitaxial films was controlled precisely over the range from 10^{16}-10^{19} cm^{-3}. With reduced concentration of carriers, the electron mobility increased [40].

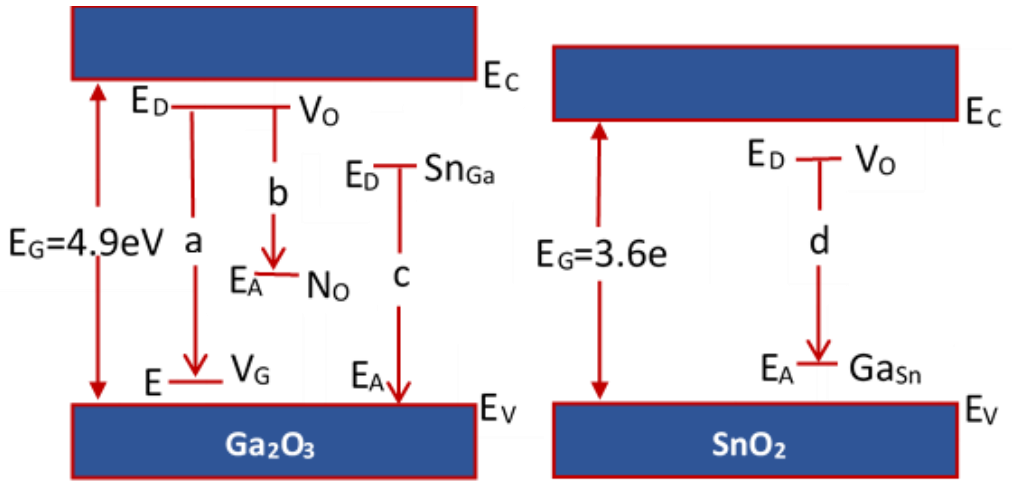

Figure 1.9: Schematic illustration of radiative transitions observed in β-Ga_2O_3 and SnO_2 [59].

A proposed schematic diagram (figure 1.9) was given by Maximenko, *et al.* [59] on several radiative transitions observed in β-Ga_2O_3 and SnO_2. The blue emission which is related to the recombination process (a), results from the recombination between trapped electron through oxygen vacancies at donor levels (E_D-V_O) and holes captured through gallium vacancies at acceptor levels in β-Ga_2O_3 (E-V_C). The recombination process (b) (the red emission) arises when transitions occur among trapped electrons through oxygen vacancies and captured holes by nitrogen impurities on deep acceptor levels (E_A-N_O). (c) Recombination from donor levels, introduced when Sn atoms incorporate in Ga tetrahedral sites of β-Ga_2O_3 (E_D-Sn_{Ga}), to acceptor levels at the topmost part of the valannce band (E_A). Transitions between trapped electrons by oxygen vacancies and captured holes introduced by Ga impurities (E_D-V_O) on deep acceptor levels (E_A-Ga_{Sn}) lead to the recombination channel (d) related to the red emission in SnO_2 showed in figure 1.9 [59].

Silicon acts as an effective dopant for Ga_2O_3 crystal as well. Atomic radii of Ga^{3+} and Si^{4+} have a relative difference of about -40% which is significant when comparing with the relative difference of atomic radii for Ge^{4+} (-16%) and Sn^{4+} (+14%) [60]. Taking the

atomic radius into consideration, in the cationic site of Ga^{3+}, Ge^{4+} and Sn^{4+} possibly a better fit than Si^{4+}. But as a n-type dopant, Si shows great advantage for growth by the melt technique because Ge and Sn tend to evaporate at a high rate unlike Si. Using Float-Zone method, Si doped Ga_2O_3 crystals were produced by Villora and coworkers [60]. When the Si concentration increases in the feed rod, the conductivity also increases continuously from 0.03 $\Omega^{-1}cm^{-1}$ (undoped crystals) to 50 $\Omega^{-1}cm^{-1}$ (highly doped crystals). The concentration of free-carriers exhibits a range of values three orders of magnitude (10^{16}-10^{18} cm^{-3}) with silicon doping, while the mobility oscillated around 100 cm^2/Vs.

With available sapphire (0001) and β-Ga_2O_3 (100) substrates, Si doped β-Ga_2O_3 thin film were grown by metal organic vapor phase epitaxy (MOVPE) [61]. Trimethylgallium, water vapors, and tetraethylorthosilicate were used as gallium, oxygen and silicon precursors, respectively. The growth temperature was varied from 800-850°C with a fixed base pressure of 5 and 10 mbar. The incorporation of Si showed a maximum value of approximately 5×10^{19} cm^{-3} by SIMS measurements while low conductivity was determined from Hall and CV measurements for both as-grown and annealed films [61].

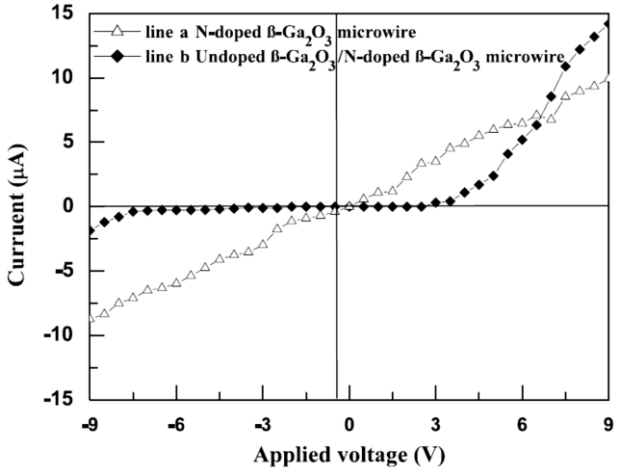

Figure 1.10: I -V measurement performed on a i) N-doped β-Ga_2O_3 microwire, ii) undoped β-Ga_2O_3/N-doped β-Ga_2O_3 microwire junction [62].

Still there is a dispute on the feasibility of p-type conductivity in Ga_2O_3. Achieving p-type conductivity in Ga_2O_3 nanowires by doping with nitrogen was claimed by Liu *et al.* [62]. Their conclusion on p-type conductivity of Ga_2O_3 was based only on I-V measurements (figure 1.10). However, they did not provide any profound analysis of concentration and carrier mobility. Zhang and co-workers performed a theoretical modeling which disclosed that a shallow acceptor impurity level at the top of the valence band is formed by nitrogen, shifting the Fermi level at the impurity level [31]. Ga_2O_3 single crystal growth using Ge and Ti dopants by the floating zone method showed p- and n-type conductivities according to Tomm et. al. [63] 10^5 cm^{-3} hole concentrations at room temperature were achieved, but for feasible applications this doping level is still very low [63].

Theoretical calculations [39] showed that it is impossible to grow β-Ga_2O_3 with p-type conductivity because holes have robust self-localization as a result of the ionicity of metallic oxides. Even if a substitutional dopant is able to provide a positive hole successfully, it is closely localized around a single oxygen atom preventing it to move inside the crystal lattice, even in the presence of an applied electric field [64]. So, it can be estimated that, at room temperature the hole mobility would give a very small value of 10^{-6} cm^2/Vs indicating insignificant p-type conductivity of Ga_2O_3, even if it is possible to introduce holes into the material [31].

Using density functional theory, Guo, *et al.* [65] showed the influence of photocatalytic activity and doping on the band edges of β-Ga_2O_3 for doping with nonmetal elements such as C, N, F, Si, P, S, Cl, Se, Br, and I. When doping with C, Si and P, few impurity states are confined in the center of the band gap which are responsible for

detrimental effect on photocatalysis due to the reduction of the semiconductors efficiency by the gap states acting as recombination centers (figure 1.11). Substitutional F on O sites does not narrow the band-gap. According to figure 1.11, doping with N, S, Cl, Br, I and Se are supposed to improve the ability of photo-reduction of Ga_2O_3. Doping with Se shifts the absorption edge from the UV to visible wavelength range [65].

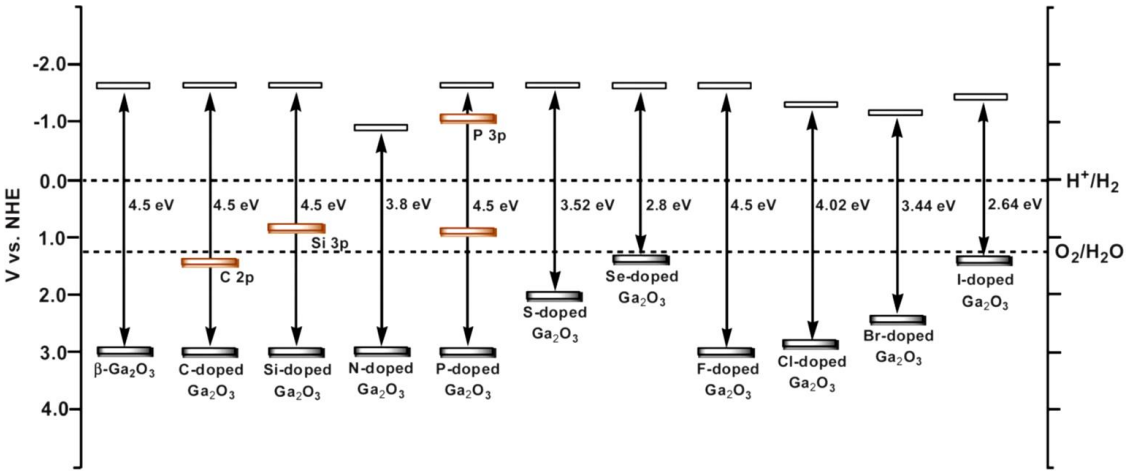

Figure 1.11: Schematic representation of the calculated VBM and CBM positions of X-doped Ga_2O_3 with reference to those of pure Ga_2O_3 [65].

1.1.5 Alloy of $(In_xGa_{1-x})_2O_3$ and $(Al_yGa_{1-y})_2O_3$

The alloy of (In-Ga-Al-O) is very promising for future semiconducting device as it is possible to tune the bandgap from 3.5-8.6eV which can cover the 144-354 nm wavelength range. As the (In-Ga-Al-O) alloy can cover nearly the complete UV spectrum, it can be a potential candidate for UV opto-electronics devices such as UV-identification, microorganism destructions for air or water purification, optical sensors and analytical instrumentations, solid-state lighting, medical imaging of cells, light therapy in medicine, forensic analysis and drug detection. The crystal structure of Al_2O_3, Ga_2O_3 and In_2O_3 is shown in figure 1.12.

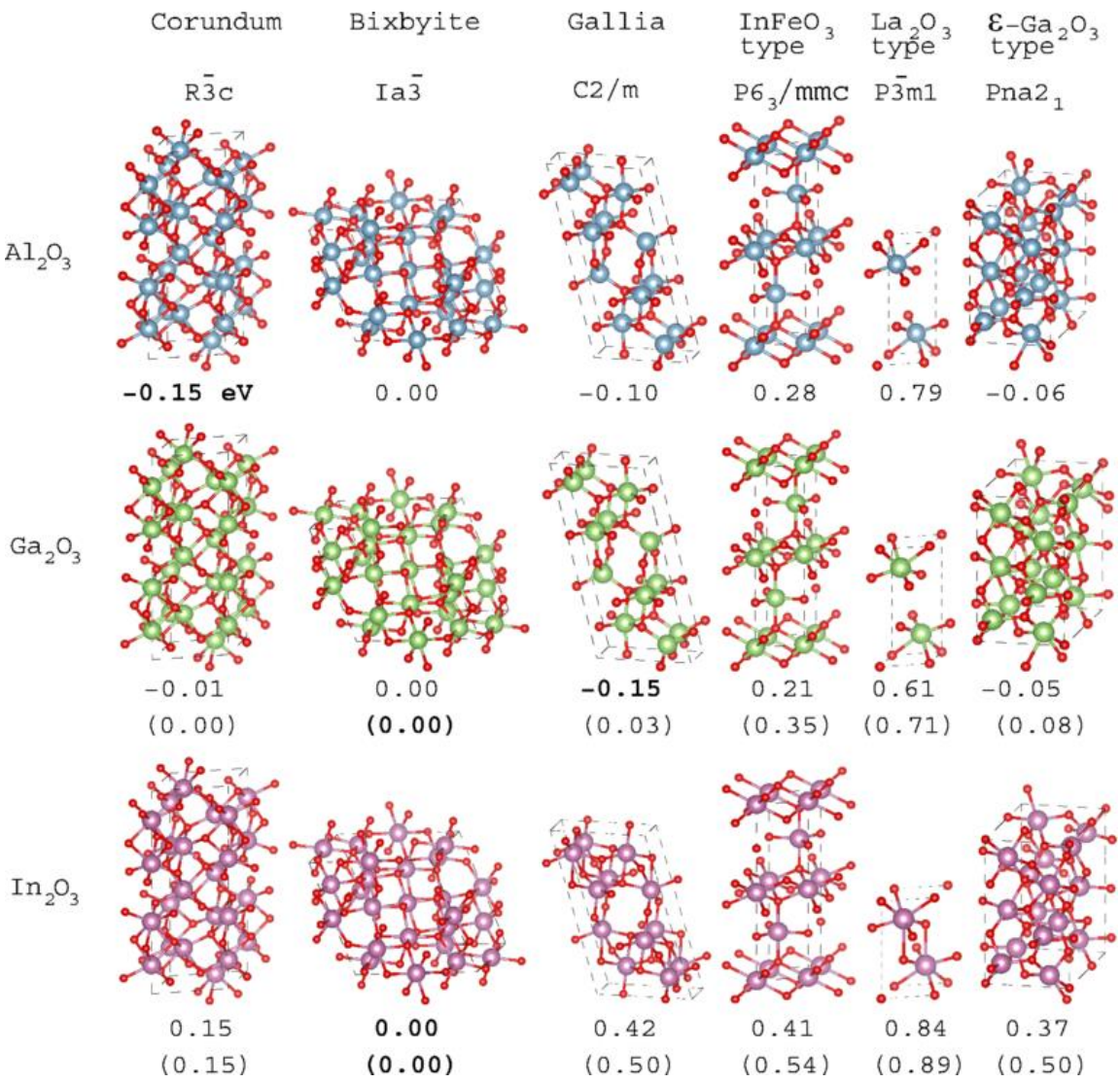

Figure 1.12: Different crystal structures of Al_2O_3, Ga_2O_3 and In_2O_3 [66].

The $(In_xGa_{1-x})_2O_3$ alloy has Ga_2O_3 and In_2O_3 components which have different lattice structure. In_2O_3 has bixbyite cubic structure which is stable at room temperature with 16 In_2O_3 per unit cell where the dimension of the cell is 10.11 Å. The cation sited are divided into two ways: octahedral and tetrahedral. The $(In_xGa_{1-x})_2O_3$ alloy shows three different structure and those are monoclinic, mixed phase or cubic structure depending on the composition of the alloy. The study of XRD (x-ray diffraction) [67] and hyperfine interaction of Cd in In-doped β-Ga_2O_3 [68] verified that In ions prefer to occupy the

octahedral sites and thus In atomic orbitals contribute significantly to the conduction band edge as expected and demonstrated by Binet *et al.* [69].

The initial work on $(In_xGa_{1-x})_2O_3$ alloy by D. Edwards *et al*. [67] reported a decrease of In_2O_3 solubility limit (from 44.1 mol% to 41.4 mol%) in the β-gallia structure when the temperature was increased from 1000-1400°C. Binet *et al*. [69] showed the enhancement of $(In_xGa_{1-x})_2O_3$ samples by coprecipitation and annealed at 1400°C where β-gallia phase was found for $x<0.4$. Wang *et al*. [70] reported on $(In_xGa_{1-x})_2O_3$ films with x=0.0-1.1 grown by MOCVD with the conclusion that carrier scattering is determined by the existence of ionized or neutral impurity scattering centers not by the lattice distortion or high-angle grain boundaries. Oshima *et al*. [71] have damonstrated MBE grown $(In_xGa_{1-x})_2O_3$ thin films with a buffer layer of Ga_2O_3 on a Al_2O_3 (0001) substrate. When the alloy was grown with high substrate temperature of 700-800°C, In segregation and phase separation was observed for x=0.08 but lower substrate (≤600°C) temperature is effective for the phase separation suppression. Nanowires based on $(In_xGa_{1-x})_2O_3$ alloy have also been investigated. Linn *et al*. [72] reported on nanowires based on tunable growth of In-doped Ga_2O_3 (Ga_2O_3:In) and Ga-doped In_2O_3 (In_2O_3:Ga) on Au coated Si substrate by modulated water vapor in Ar with the temperatures of 700-750°C.

For the alloy of $(Al_yGa_{1-y})_2O_3$ the components Al_2O_3 and Ga_2O_3 have corundum and monoclinic crystal structure respectively with the same electronic structure. The investigation of this alloy is continuing and a complete picture is needed to understand its full potential. Oshima *et al*. [73] reported the growth of β-$(Al_yGa_{1-y})_2O_3$ films on β-Ga_2O_3 (100) single crystal substrate using PAMBE. With the Al content of x=0.61, coherent growth was achieved but when the Al content is below than x=0.4, step-flow growth was

observed. Ito *et al*. [74] has grown corundum structured α-$(Al_yGa_{1-y})_2O_3$ films on c-plane sapphire substrate by spray-assisted mist CVD. However, the detail investigation on the bandgap engineering of this $(Al_yGa_{1-y})_2O_3$ was not performed probably because the wavelength range of most spectrometers are limited. In order to solve this problem for high Al content alloy, it was recently revealed that, the bandgap of this alloy can be measured by using the onset of inelastic energy loss in core-level atomic spectra from x-ray photoelectron spectroscopy measurements [75]–[77]. In the inelastic collision, the plasmon in the bulk and at surface excitation and single particle excitation were caused by band-to-band transitions. As the fundamental lower limit of inelastic loss can be defined as the bandgap energy, so that, the onset of the inelastic energy loss could be equivalent to bandgap energy of thin films [77].

II. GROWTH METHODS AND CHARACTERIZATION TECHNIQUES

In this chapter, the two different deposition techniques viz. molecular beam epitaxy (MBE) and pulsed laser deposition (PLD) are described as this study covers both growth techniques to grow β-Ga_2O_3. In this research, the crystal structure and preferred orientation of the thin films were investigated using X-ray diffraction measurements on a Rigaku SmartLab system with a Cu rotating anode. Four-bounce channel-cut Ge (220) crystals were used to obtain Cu Kα radiation and to eliminate vertical divergence. Aberration-corrected JEOL JEM-ARM200CF scanning transmission electron microscopy (STEM) equipped with a cold field-emission source and an Oxford X-max 100TLE windowless SDD X-ray detector were utilized for crystal structure, microstructural and interfacial analysis at atomic resolutions. Epitaxial relationships between Ga_2O_3 and Al_2O_3 and the quality of interface was determined by both high-angle annular dark-field (HAADF) and annular bright-field (ABF) images acquired at 200 kV, with a collection semi angle from 90 to 170 mrad and 11 to 22 mrad respectively. The cross-section sample was polished using Allied High Tech MultiPrep polishing system and then thinned down to electron transparency (<100 nm) using Fischione IonMill. The surface morphology and roughness were measured using a Park XE7 atomic force microscope (AFM). Chemical compositions and Ga oxidation states were investigated using x-ray photoelectron spectroscopy (XPS) with a Mg x-ray source. Refractive indices and film thicknesses were measured by a variable angle spectroscopic ellipsometry (SE) using J.A. Wollam, M-2000 ellipsometer and optical transparency were determined using a Shimadzu UV-2501 UV-Vis spectrometer. Finally, the electrical characterization was done by means of a Keysight

B1500A semiconductor device analyzer.

2.1 Film Deposition Techniques

2.1.1 Molecular Beam Epitaxy

Molecular beam epitaxy (MBE) is a physical vapor deposition technique that has unique *in-situ* diagnostic capability and used to grow excellent quality single-crystal epitaxial films. This technique was developed to deposit the GaAs and GaAs/AlGaAs compound semiconductor material in the 1960's at Bell Telephone Laboratories by J. R. Arthur and Alfred Y. Cho [78], [79] for investigating and understanding the nature of epitaxial thin film growth on an atomic level. It has since been applied to the growth of thin films of various semiconductor materials as well as metals and dielectrics. The advantage of using MBE technique to grow thin films is the capability of substituting cations randomly in a single growth of compound materials by removing the necessity of changing target or other discrete steps of multiple run growth that are needed for other deposition tools. Moreover, it has an exact layer-by-layer control on the growth resulting in having complete surface termination control of the growing film comparing to sputtering or pulsed laser deposition technique [80].

A MBE system consists of one or more growth chambers with individual associated pumping system and load-lock to load and unload the samples or wafer into or from the MBE system without significantly affecting the vacuum condition of the growth chambers. In this way, growth chambers can be used efficiently with increased quality of operations by separating the equipment. The schematic diagram of a MBE chamber is shown in figure 2.1. The oxide growth chamber used in this study is shown in figure 2.2 and has a base pressure of about 10^{-10} torr through a combination of turbo and cryopump, source of

materials called effusion cells which provides highly directional evaporation of material, a cryoshroud surrounding the growth region, ion gauge to measure the pressure of the chamber, manipulator to hold the substrate and heater, mechanical shutter to block the molecular beam if needed, *in-situ* RHEED (reflection high energy electron diffraction) to monitor the real time growth and a quadrupole mass analyzer to detect specific background gas species in the chamber.

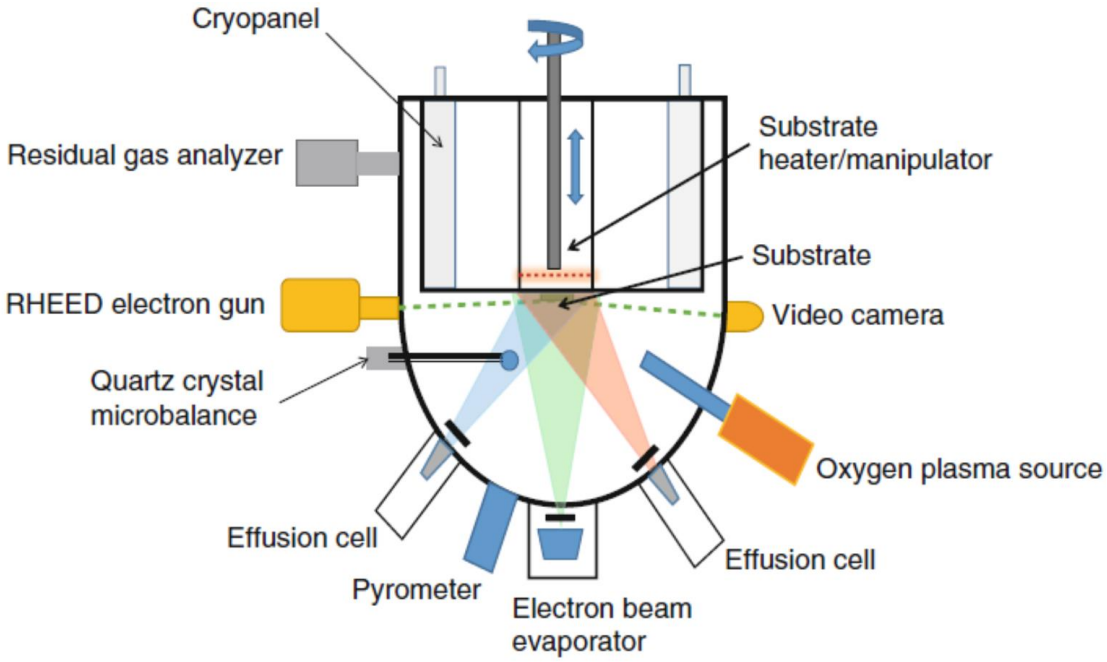

Figure 2.1: Schematic diagram of MBE system.

In principle, the MBE technique involves highly controlled thermal evaporation of source materials from effusion cells directed to the substrate in a chamber with ultrahigh vacuum condition to achieve epitaxial growth of materials. The lower background gas pressure is needed to diminish the unintentional contamination resulting in relatively slower deposition rate of epitaxial growth [81], [82]. Because of this high vacuum condition, the mean free path of molecular beam and gases are greater (couple of order of

magnitude) than the distance between source and substrate (typically 20 cm). Mainly, the reactions occurred on the surface of the substrate by incorporating the source beam into the growing film. The shutters of the source are mostly made of molybdenum and tantalum which are used to grow complicated multilayer structures with different compositions in a monolayer level that are highly controlled by turning on or off the beams very quickly. However, the temperature of the high-purity pyrolitic Boron nitride (PBN) crucible which is in the effusion cell control of the atomic beam flux and associated with the vapor pressure of the evaporated source material.

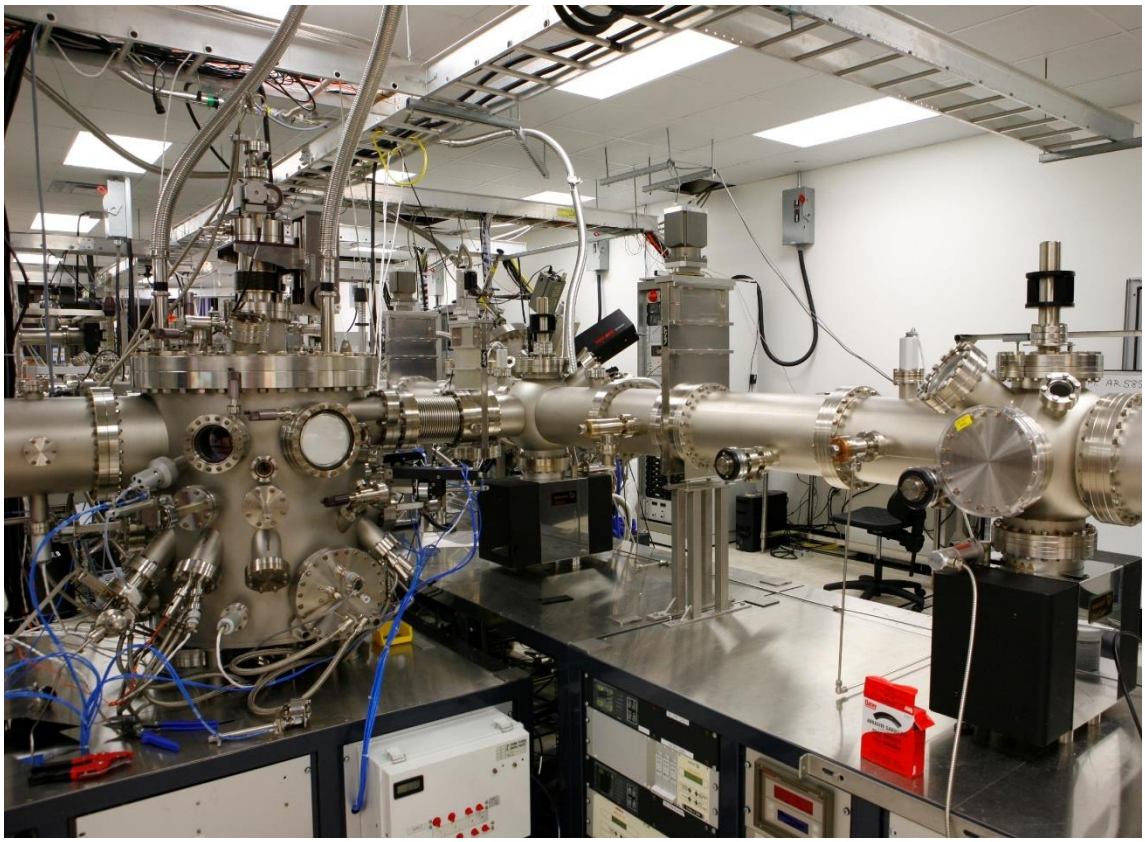

Figure 2.2: Oxide MBE chamber at advanced functional materials laboratory of Texas State University.

In oxide MBE, the source of O_2 can be molecular oxygen or a reactive species either oxygen plasma or ozone or an oxygen/ozone mixture to oxidize the thin films. Among

them, ozone is very toxic and flammable, thus required careful action with additional equipment. Through the oxygen nozzle, the oxygen species are supplied into the chamber and a mass flow controller or a piezoelectric mass controller gas valve can be used to control the flow rate of the oxygen. The oxygen pressure for the growth in MBE is limited due to interaction with hot filaments and degradation. The use of molecular oxygen is limited and can only be used for metal which can easily oxidized. On the other hand, there are some other oxides such as Ga_2O_3, $LaCoO_3$ and $LaNiO_3$ that require a more reactive oxygen source to grow stoichiometric layer. The growth of simple metal oxides where the metal in its highest oxygen state is straightforward as it needs excess oxygen with a single metal flux whereas for the growth of multi-cation oxides (for example the perovskite oxides) is more difficult as it needs two matched metal flux for correct stoichiometry with correct phase. As a result, flux measurements is very important for MBE growth [83].

There are three techniques available to monitor the flux in MBE and those are: (a) a nude ion gauge to measure beam-equivalent pressure, (b) a quartz crystal microbalance, and (c) using atomic absorption spectroscopy. One or two of these techniques are used to measure the flux. When an ion gauge is used for source flux measurement, the gauge is mounted on a retractable arm which can be set to the position of the substrate. By opening and closing the shutter of the effusion cells, ion gauge shows beam equivalent pressure which can be used to calculate the flux using simple equation [84]. When a quartz crystal microbalance is used to measure the flux, it is mounted on a arm which can be brought to the substrate position during flux measurement and variation of the oscillation frequency of a quartz crystal is utilized because deposited materials changes its total mass [85]. Quartz crystal microbalance takes over 30 minutes for stable reading. Because of its sensitivity to

temperature, quartz crystal monitors are usually cooled by water. The accuracy of the flux measurements obtained from ion gauge beam equivalent pressure and quartz crystal microbalance is around 5% which is insufficient for some specific applications. Atomic absorption spectroscopy flux measurement technique is used for those applications that require accuracy in the flux measurement in <1% [86]. In this process, light beam is guided in to the path of the evaporating material and the amount of absorbed light is measured by a detector. The measurement, is element specific element since the light absorption of atoms is specified by wavelength of light. However, this technique of flux measurement requires expensive set-up of instruments.

Generally, a transition metal is one of the components in a complex oxide layer but some of those have very low vapor pressure that make them difficult to evaporate thermally with sufficient flux required for deposition at reasonable growth rates. Transition metal like titanium or vanadium can be thermally evaporated with stable flux but with low flux rate using effusion cell at 2000°C while there are some other transition metals like niobium and ruthenium are not able to produce significant flux with a 2000°C effusion cell temperature. Electron beam evaporation is also included in an oxide MBE chamber and is used for these type of transition metals with low vapor pressure though it has poor flux stability and reproducibility [87]. There is also a concern of using the effusion cells at high temperature due to availability of suitable crucible material.

2.1.2 Pulsed Laser Deposition

Pulsed laser deposition (PLD) is a technique which can be used to deposit oxide thin films including heterostructures combining different oxide interfaces utilizing a series of high power pulsed laser focused onto the source material to transfer the desired composition to

the substrate under high vacuum [88], [89]. PLD technique was discovered during the growth of high Tc superconductors growth by the researchers at Bell Communications Research and developed into a very versatile and important deposition technique for the complex oxide thin films [90], [91]. A schematic diagram of the basic PLD is shown in figure 2.3.

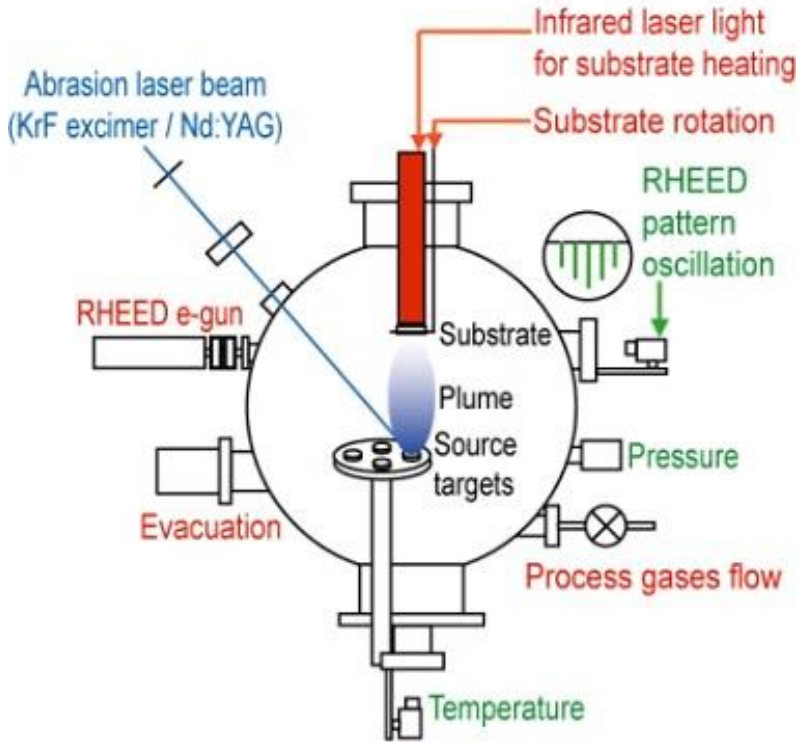

Figure 2.3: Schematic diagram of a PLD system [92].

PLD technique has several advantages making it favorable for the deposition of complex materials. The first advantage is the possibility of transferring the stoichiometry of the target material under optimized condition to the substrate due to the absorption of high laser energy by a small portion of target that creates a plume containing ablated material. Hence, there is no need to control precisely the evaporation rate individually for the elements of a compound material as the stoichiometry of the film is the same as that of

the target. The second advantage of using a PLD is having the capability of using background gases with a flexibility to adjust over a wide range of pressure that could be from ultrahigh vacuum to several Pascal during the growth. This provides another parameter to optimize the growth process for the oxide growth. The third advantage is the deposition of the multicomponent film using a single stoichiometric target with several elements or different targets for every element with the help of a programmable rotation system of target to facilitate complex multilayer growths.

In principle, a pulsed laser from the high-power KrF excimer source with 248 nm wavelength is excited and hit the target (source material) to deposit onto the substrate surface. The laser usually focused onto the target by means of a quartz lens that is located outside of the vacuum chamber. Due to the high energy of the laser, atoms from the target are evaporated hyper-thermally by every laser pulse and transported to the substrate with high kinetic energy (5-100 eV) making it possible to deposit material at lower substrate temperature since there is enough energy for sufficient surface diffusion.

The main components of a PLD system are the substrate manipulator and target holder. The substrate manipulator also consists of a heater to increase the substrate temperature for the growth of single crystal epitaxial thin films. Most of the PLD systems use target rotation system and laser scanning/rastering to alleviate irregular target erosion. As the laser makes the targets very hot, the target holders are typically water-cooled. Targets have disc shape and there are several ways (mechanical clamping, bonding, or magnets) to mount the target onto the target holder which allow for easy accessibility and easy mounting or dismounting. The PLD system used in this research for the growth shown in figure 2.4.

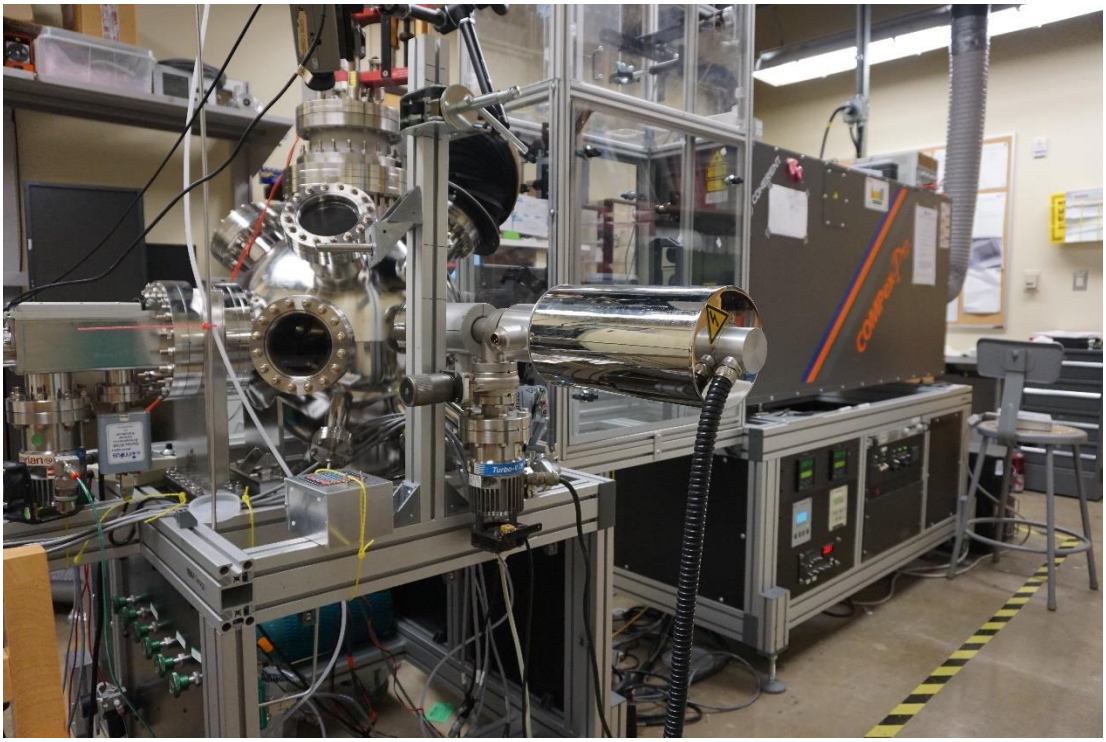

Figure 2.4: PLD system installed at Texas State University.

The most expensive and important hardware piece is laser in a PLD system where the laser wavelength is chosen so that it is absorbed by the target material and can provide high energy densities greater than 1 J/cm^2. Usually PLD system uses excimer lasers with either KrF (248 nm) or XeCl (308 nm) because the optical wavelength required for successful deposition is in the range of 200-400 nm due to the need for creating the necessary plume from the target [89]. Optical elements are required between the growth chamber and the laser to focus and guide the laser beam. Other critical elements in the PLD system are the geometry of the growth chamber along with relative positions of the target, the beam focal point and the substrate. The required angle between the target and the laser port (through where laser enters into the chamber) is 45°. Also, the distance between substrate and target is very crucial for the stoichiometric growth in PLD process. For

uniform deposition, a rotating substrate stage is used. The system also has a differentially pumped RHEED so that the crystal surface structure can be monitored during growth.

For the growth of complex oxide thin films, several processing parameters such as laser fluence, repetition rate, the substrate temperature and the oxygen partial pressure are important parameters that can influence the composition and microstructure of the films [89]. The laser fluence is critical for target stoichiometry while the repetition rate has an important influence on the morphology [93].

2.1.3 Target Preparation

The ceramic targets need to be prepared for the thin film deposition by PLD technique. In this research, the preparations of the targets were done by widely used technique known as ceramic sintering which is based on solid state reaction between the materials. The first step of the standard ceramic synthesis process is mixing the oxide nano powders in different weight/atomic ratio for required mole fraction in alloys by using ultrasonic ball milling for 10-30min. After that, the mix powder was pressed by a hydraulic press machine to make ceramic disk for 10 hours with pressure of 10000 lb. The ceramic pellet was annealed by a high temperature furnace at 1000-1200°C for 10-20 hours for the solid-state reaction. Porosity and density of ceramic pellet depend on the sintering process as the size and shape of the pores decreases and becomes spherical respectively during sintering. The targets for the thin film depositions were formed with the dense and hard ceramic pallet by polishing the surface using a sand paper. Finally, the targets were evaluated by the XRD measurements for further confirmation of the composition and loaded into the PLD chamber for the deposition.

2.2 Structural Characterization

2.2.1 Reflection High Energy Electron Diffraction

Reflection high energy electron diffraction (RHEED) is a unique *in-situ* surface characterization technique for real time monitoring of the growth. The basic principle of RHEED based on high energy electron diffraction from the surface of the material. This process has the sensitivity to surface morphology and allows the investigation of the crystal symmetry and atomic reconstructions on the material surface.

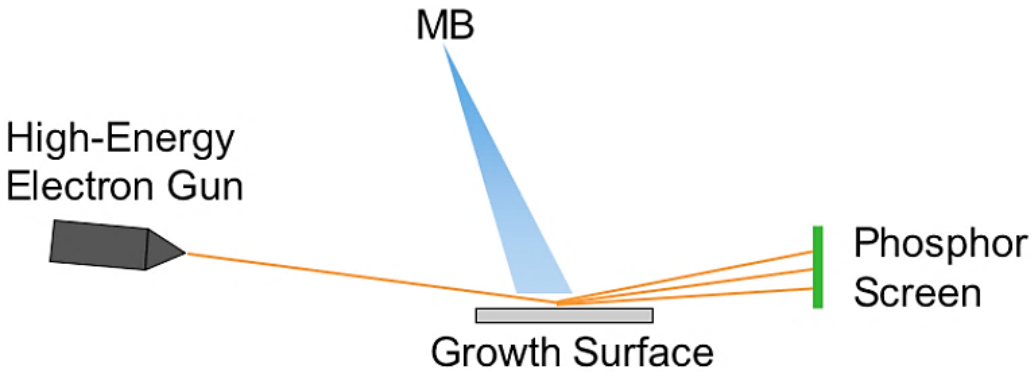

Figure 2.5: Pictorial description of a RHEED operation and diffraction geometry during MBE growth.

The basic components of the RHEED system are an electron gun to generate electrons and camera to collect the diffraction pattern from a phosphor screen (figure 2.5).

The process of RHEED involves the high energy (~10-30 kV) electrons emitted from the electron gun that are incident upon the sample surface at glancing angle (~1-3°) and a series of diffracted beams are viewed on an opposing phosphor-coated screen which are then collected by a charge coupled device (CCD) camera detector to make visible on a computer for analysis. This geometry setup does not interrupt the line of sight between evaporation source and substrate, so that it can be performed at the same time during growth to monitor in real time the growth process [83]. Atomic arrangement on the surface

of the sample are responsible for the RHEED pattern. Traditionally, RHEED is used with MBE technique. However, it is utilized with PLD system together with differential pumping to reduce the effect of high oxygen pressure during growth.

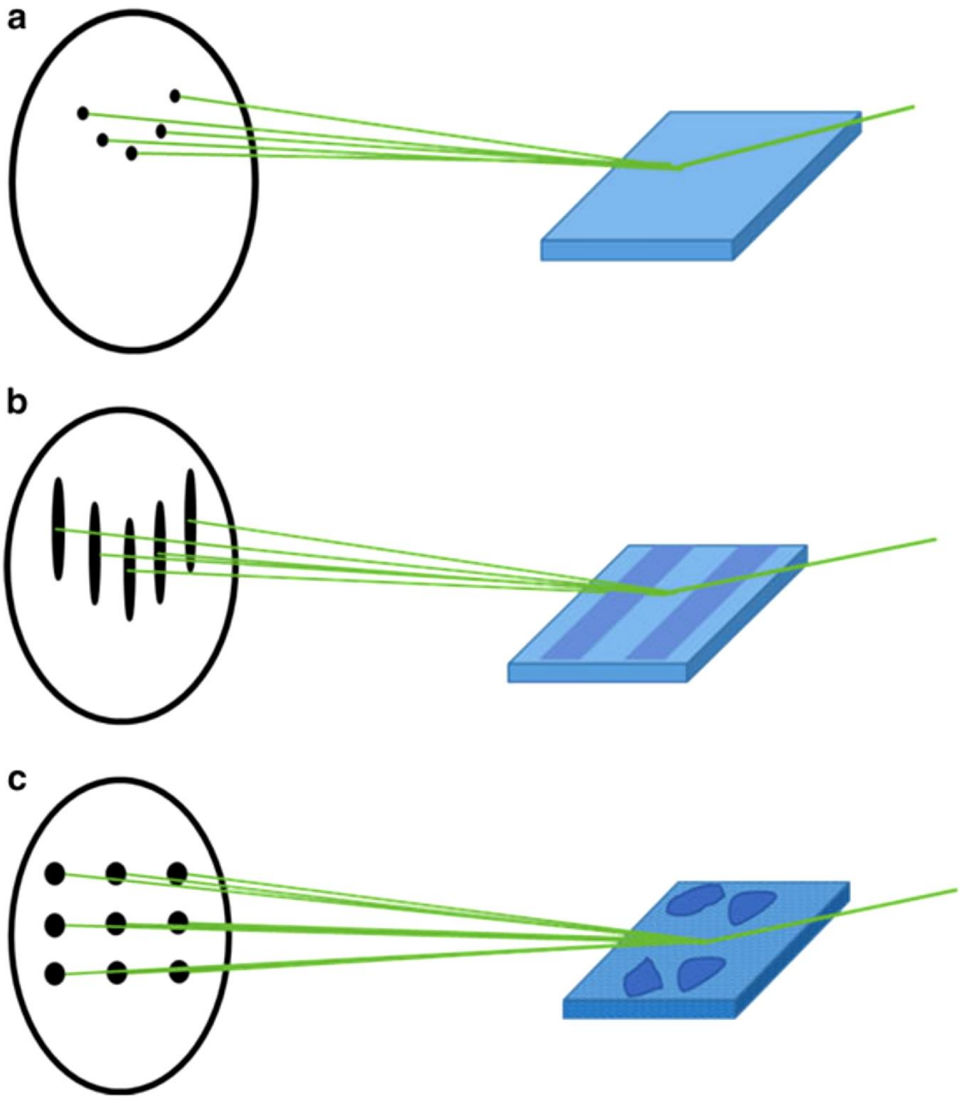

Figure 2.6: RHEED characteristic patterns from different surfaces based on quality of flatness. (a) when flat regions on the flat surface are broader than the coherence length of the effective incident electrons. (b) when the flat surface contains uncorrelated terraces with widths which are narrow compare to coherence length. (c) when the surface is rough along with islands which shows transmission diffraction pattern [83].

RHEED can be used to determine the crystal structure of the surface with corresponding crystal orientation (figure 2.6). However, there are several other applications

of RHEED and the most widely used one is to use the RHEED oscillation [94] to monitor the intensity of the specular spot when a layer by layer epitaxial film is growing. The intensity of the spot is minimum for the half of a layer growth and maximum for single complete layer (one monolayer) of material deposition. The number of layer of material that has been deposited can be counted precisely by plotting the RHEED intensity oscillations. The period of oscillation represents the growth rate of the film. Individual elemental fluxes can also be calibrated by using RHEED intensity oscillations for multicomponent oxides such as $SrTiO_3$ [95] and $YBa_2Cu_3O_x$ [96]. The growth mode (flat layer by layer or island growth) of the film can also be determined by the RHEED. Schematic RHEED patterns for different kind of surfaces is shown in figure 2.3. A "spotty" pattern along a circular arc (the zeroth Laue zone) can be seen for flat surface while Laue zone spots spread out into streaks for a typical flat surface which has uncorrelated short lateral terrace widths. A two-dimensional diffraction spots array is appeared for the rough surface where some electrons are transmitted through the islands [97].

2.2.2 X-ray Diffraction

X-ray diffraction (XRD) is a non-destructive powerful analytical technique is used to study the crystal properties by collecting the structural information of materials including powder to thin films [98]. This fundamental technique is used to identify the crystalline phases with information about unit cell dimensions, chemical compositions and physical properties of the materials. A beam of x-rays resulting in diffraction in various specific directions in this XRD process. The wavelength of the incident x-rays is fixed and a crystallographic arrangement of the crystal atomic planes are determined by every diffracted angle where atomic planes are defined by the periodic arrangement of atoms in

the crystal. The basic criteria for interference is the Bragg's condition which is given by the following equation [98]:

$$2d \sin\theta = n\lambda$$

In this equation, θ is the incident angle of x-rays, d is the spacing between the atomic planes of the crystal, λ is the wavelength of the x-rays, and n is the integer representing the order of the diffraction peaks. Bragg's law can be described by figure 2.7.

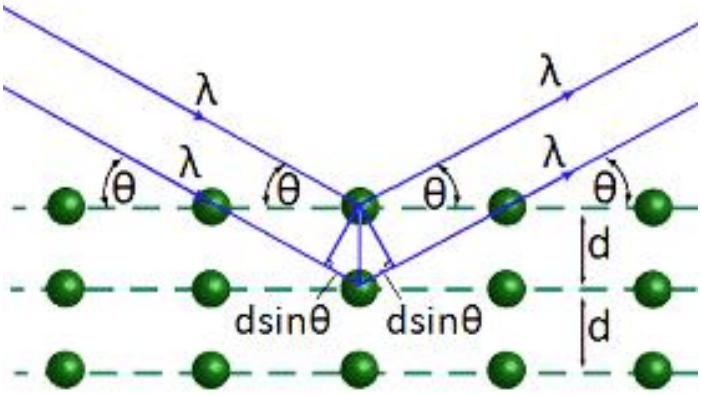

Figure 2.7: Schematic diagram of demonstrating Bragg's law and here, λ is the x-ray wavelength, n is an integer, θ is the incident angle and d is the lattice spacing of the crystal.

The incident parallel x-ray beam is incident onto a regular array of crystal atoms with an incident angle of θ and diffracted from the parallel planes of crystal atoms [99]. Due to the different path travel, two consecutive reflected beams possess a phase difference. The reflected beams interference constructively only when the geometry satisfies the Bragg's condition (equation 2.1) that is, the path difference which is multiple integer of the x-ray wavelengths [100]. Usually, generated characteristics x-ray spectrum is plotted as diffracted x-ray intensity versus 2θ graph. The obtained spectrum is analyzed by comparing with the x-ray crystallographic library or database to obtain the orientation and composition of the layers in the grown structure. By using the above Bragg's equation,

crystal properties such as atomic structure, lattice constant, and disorders can be determined.

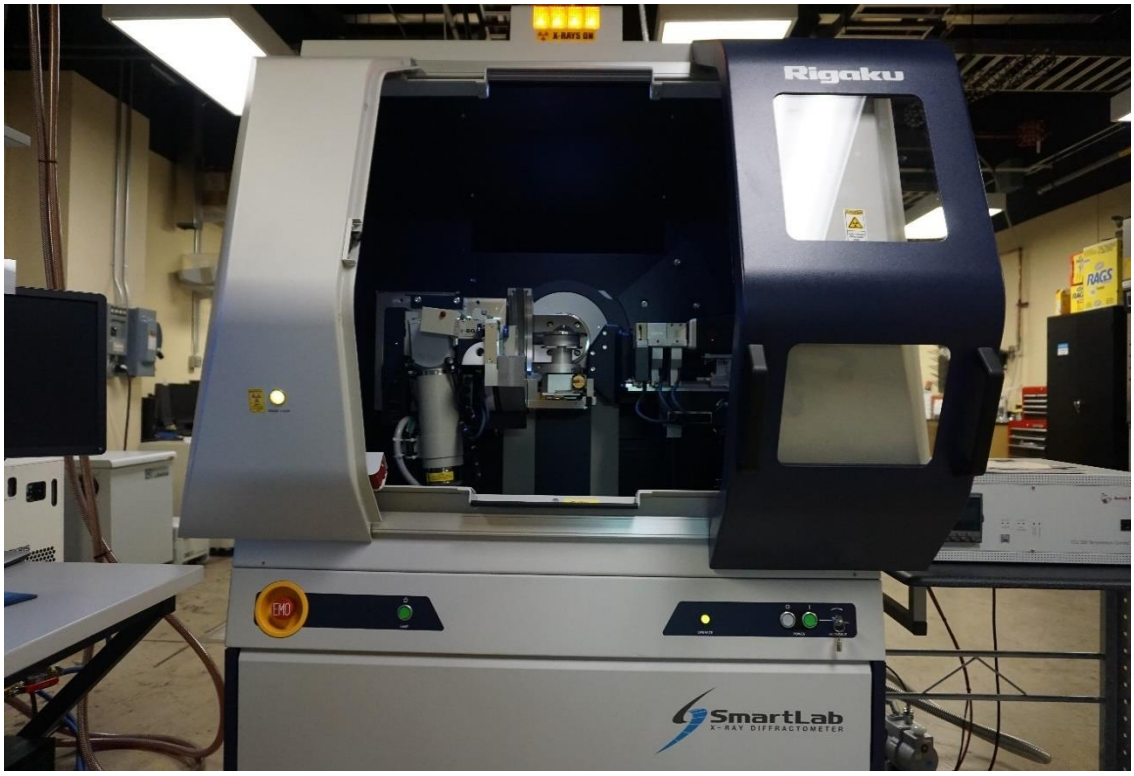

Figure 2.8: Highly functional Rigaku SmartLab XRD system of Texas State University.

In this study, a Rigaku SmartLab X-ray diffractometer (figure 2.8) is used to measure the XRD spectrum for grown films. It consists of Cu Kα source with a wavelength λ = 1.540562 Å operates at 40 kV and 44 mA, a goniometer stage where the sample is mounted and a detector to collect the diffracted X-rays. With the help of the various x-ray scattering methods provided by the system, different XRD measurements were carried out including θ-2θ, high resolution rocking curve and in-plane phi (φ) scan.

2.2.3 X-ray Photoelectron Spectroscopy

X-ray Photoelectron Spectroscopy (XPS) is a powerful technique to analyze the chemical nature of compounds using x-rays in an ultrahigh vacuum environment. A variety

of information for a sample can be investigated with this technique including elemental composition, chemical bonding, band structure and offsets. In principle, when soft x-rays, Al Kα (1486.6 eV) or Mg Kα (1253.6 eV) interact with core electrons, photoelectrons are ejected from the electronic shell due to the collision between x-rays and electrons [101]. An Auger electron is generated when an electron from valence shell filled the hole caused by the missing inner core electron in the electronic shell to conserve energy. A certain kinetic energy is released by the electrons corresponding to the characteristic binding energy of the electron from the atomic shell. The kinetic energies of the electrons are collected by the detector and is used to determine the binding energies of the electrons. The basic equation for XPS measurements is given below [101], [102]:

$$E_B = h\nu - E_K - \phi$$

Here, E_B is the characteristics binding energy and E_K is the kinetic energy of ejected electron, hv is the x-ray photon energy and Φ is the work function. Schematic illustration of XPS working principal is shown in figure 2.9.

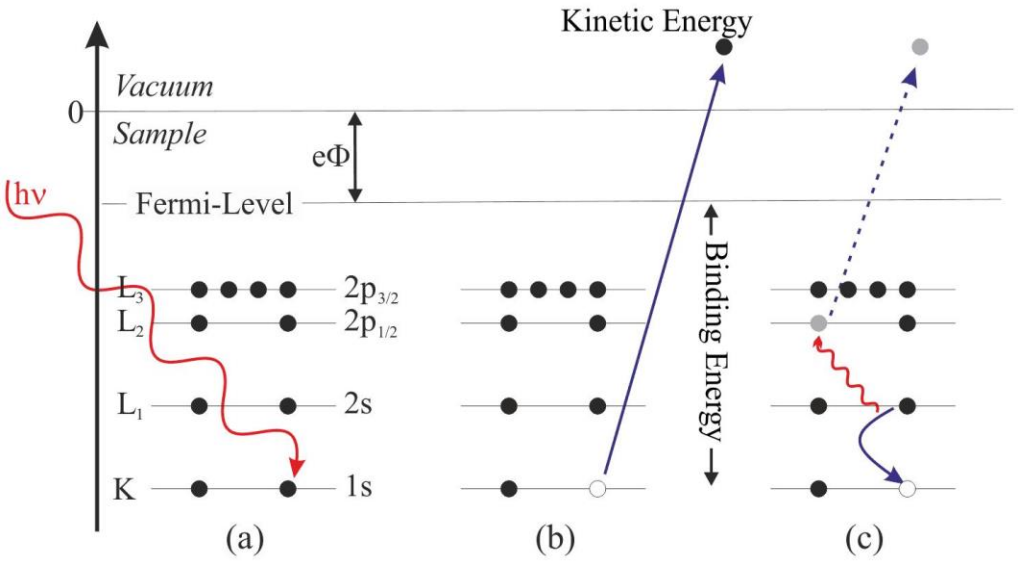

Figure 2.9: Basic working principle of photoelectron emission and Auger relaxation effect of XPS [103].

During measurements, samples are grounded to prevent the charge build up on insulating samples that can cause shifting of XPS spectrum to higher binding energy [104], [105]. Consequently, the measured kinetic energy of the electrons obtained will be different than the actual value. As carbon is the most common element that found in every air exposed sample, it is used to calibrate the energy position whereas when the XPS measurements are carried out *in-situ* immediately after growth, the oxygen peak is used as the reference.

To analyze the measured XPS spectra, a computer with data acquisition and processing software is used to determine the elements with other relevant properties of the sample. Though the collected measurements are the kinetic energy of the electrons, typical XPS spectrum is plotted as a function of binding energy of the electrons because kinetic energy represents the incident x-ray energy whereas, characteristic binding energy represents individual elements which is not related to the system. Because of the electron redistribution around the constituent atoms of the crystal, the binding energy changes with energy shifts representing the differences in the chemical bonding which is used to extract information about the oxidation or chemical state of the sample [106].

The XPS measurements were carried out using a SPECS X-Ray dual angle source viz. Mg Kα (1253.6 eV) and an energy analyzer made by Scienta (figure 2.10). A Shirley background is used to fit the measured data and acquire peak intensities. The deconvolution of obtained spectra were carried out by the summation of Gaussian line shapes which define individual components of the measured peaks with detail information of the chemical interactions properties.

Figure 2.10: SPECS XPS system of Texas State University.

2.3 Surface Morphology

2.3.1 Atomic Force Microscopy

Atomic Force Microscope (AFM) is the most used high resolution scanning probe technique to analyze the surface morphology or topography for both conducting and insulating samples [107]. AFM analysis reveals various properties of the materials including surface roughness and morphology.

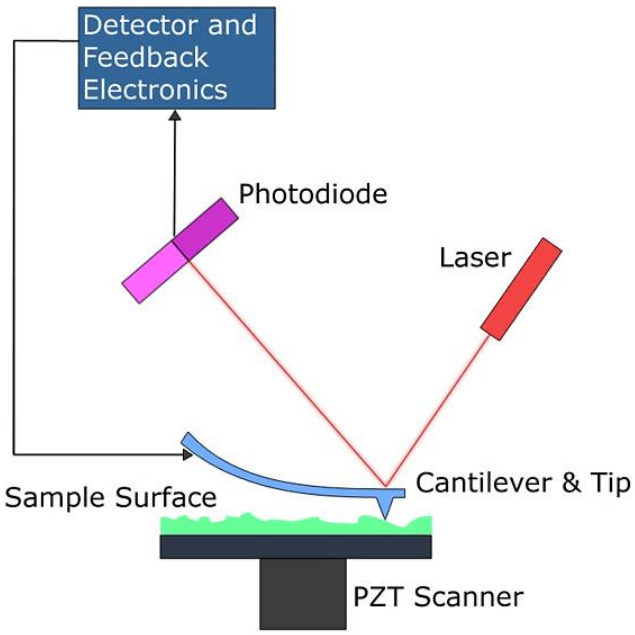

Figure 2.11: The schematic diagram of AFM [108].

The schematic diagram is shown in figure 2.11 which shows that it consists of a sample stage, photo detector, laser diode, cantilever with sharp tip and a feedback control unit which produces the corresponding image of the sample surface morphology. The sharp AFM tip is attached to the end of the cantilever used to scan across the sample surface. The deviation of the cantilever in the direction towards or away from the sample surface depends on attractive or repulsive forces experienced from the surface atoms. The working principle of AFM is based on this atomic attraction and repulsive force mapping between the atoms of the AFM tip and sample surface [109], [110]. The weak interaction force that is Van der Waals force is utilized by the AFM technique during the scan when the probing tip is very closed to the sample surface and caused vertical deflection of cantilever. Cantilever deflection measurement required a very sensitive technique due to the small force (the order of nano-Newton) between sample and probe resulting in the use of a laser based optical technique. With the use of a feedback electric current, the transformation of

deflection signals in-to the physical surface morphology is possible [111], [112]. In this study, the AFM measurements of the thin films were carried out using Park XE7 Atomic Force Microscope shown in figure 2.12.

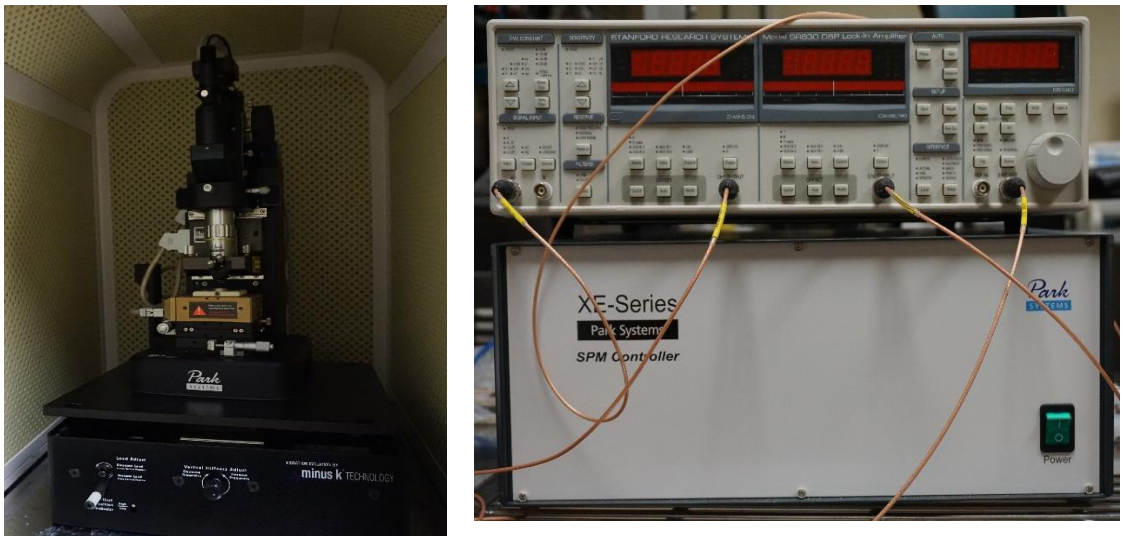

Figure 2.12: Park XE7 AFM system of Texas State University

2.4 Optical Characterization

2.4.1 Spectroscopy Ellipsometry

Ellipsometry is a widely-used technique to determine the optical constants as well as the thickness of the thin films ranging from sub-nanometers to few microns utilizing polarized light. It measures the change in polarization of the incident light after reflecting or transmitting from the surface of the sample. It can provide information about the optical properties of the measured sample which causes a modification of the incident polarization state that depends on the various optical properties of the sample including complex reflection index, dielectric constant or thickness [113]. Angstrom resolution can be achieved by ellipsometry due to its capability of using phase information with the polarization state of light despite the inherent diffraction limitation of optical techniques

[114].

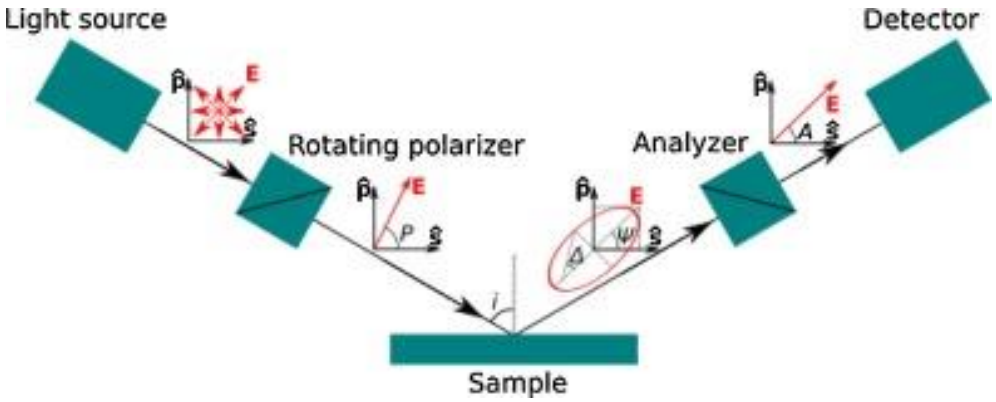

Figure 2.13: The basic configuration of ellipsometry [115].

The basic configuration of ellipsometry is shown in figure 2.13 which includes a light source, polarizer, polarization analyzer and detector. Optical components including polarizer, compensators and phase modulators are used to make the polarizer and analyzer. In principle, an electromagnetic wave is generated from a light source which is unpolarized light due to its arbitrary orientation and phase. This unpolarized light is converted into linearly polarized light with parallel (p) and perpendicular (s) components of same phase after passing through a polarizer. The linearly polarized light interacts with the sample and reflected to the analyzer and is detected with a changed amplitude and phase for both p- and s-polarized light. As shown figure 2.13, the electromagnetic wave having a random amplitude and phase is measured by ellipsometry representing an 'elliptical' polarized light. Thus, the term 'Ellipsometry' is related to the elliptical polarization [116].

However, the optical constant and thickness cannot be measured directly by the VASE (variable angle spectroscopic ellipsometry) rather it gives complex reflectance ratio (ρ) of the system expressed by the Ψ and Δ can be stated by the basic equation of ellipsometry [113], [117]:

$$\rho = \frac{R_p}{R_s} = \tan(\psi)\exp(i\Delta)$$

Where, R_p ad R_s are the light polarized parallel and perpendicular to the plane respectively, tan (Ψ) represents the amplitude ratio upon reflection and Δ denote the phase shift.

As mentioned before, ellipsometry is an indirect method and hence, the analysis of a model needs to be performed. The measured Ψ and Δ data are fitted with the appropriate models over a range of wavelengths in order to obtain the thickness and other optical parameters. Based on the Fresnel's equations, the model is established to calculate a prediction of response. Fresnel's equation is used to calculate the Ψ and Δ values for the individual material in a multi-layer model with thickness and optical constants (refractive index and dielectric constant [118], [119]. The experimental data for Ψ and Δ values are compared with corresponding calculated Ψ and Δ values and the best fit is found by the estimator named Root Mean Squared Error (RMSE) by varying the parameters of the model during the fitting procedure and given as:

$$RMSE = \sqrt{\frac{1}{2n-m-1}\sum_{i=1}^{n}[(\psi_i^{cal} - \psi_i^{exp})^2 + (\Delta_i^{cal} - \Delta_i^{exp})^2]}$$

Where, n denotes the number of data points in the spectra, m denotes the number of variable parameters in the model, and "exp" and "cal" represent the experimental and calculated data, respectively. The minimum RMSE value provides the information about the parameters such as, thickness, roughness, uniformity and refractive index of the measured sample. In this study, ellipsometry measurements were carried out by M-2000 J.A. Woollam spectroscopic ellipsometry (figure 2.14).

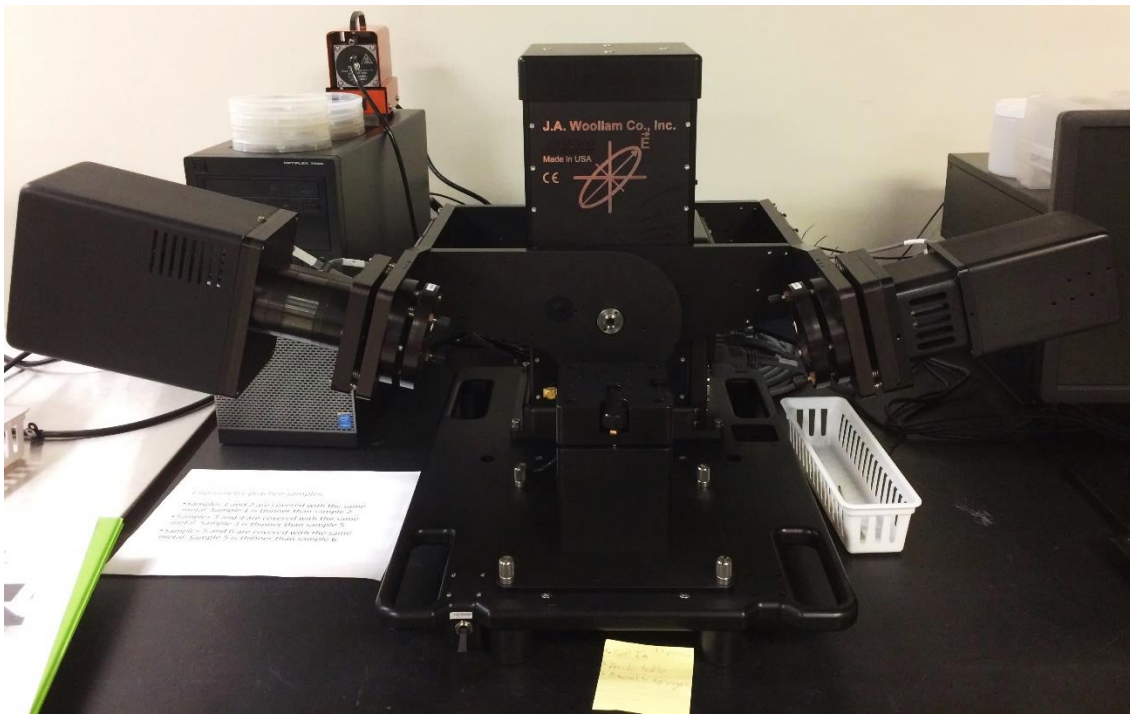

Figure 2.14: J.A. Woollam spectroscopic ellipsometry.

2.4.2 UV-Vis Spectroscopy

In order to measure the transparency of the grown thin films, a Schimadzu UV-VIS-NIR optical spectrophotometer as shown in figure 2.15 with wavelength range of 200-900 nm is used for this study. The measurements were performed on the samples at room temperature to investigate the optical properties (transmittance, absorbance or bandgap).

A small piece of two-sided tape is used to mount the sample carefully in one of the beam paths for the spectrophotometer whereas a sapphire substrate is mounted in the other beam path as a reference. Sometimes no reference sample is used to leave the reference beam path open but in this study, a reference sample is always used for the measurements. Optical transmittance or absorption is determined as a function of wavelength since the monochromatic light is passed through the sample as well as the reference sample (sapphire) and the measured light from the sample is compared to the light in the reference

beam [120].

Figure 2.15: Schimadzu UV-VIS-NIR optical spectrophotometer.

The bandgap is calculated from the obtained transmittance of the measured sample and for that at first, the absorption coefficient (α) is determined by using the absorption data (A) at every wavelength with the following equation:

$$\alpha = \frac{A}{\lambda}$$

As wavelength, λ is in nm, it was multiplied by 10^{-7} to obtain the absorption coefficient in cm^{-1}.

The absorption of the thin films with the direct bandgap follows the power law which is used to determine the bandgap given below [121]:

$$(\alpha h\upsilon) = B(h\upsilon - E_g)^{1/2}$$

Where, hυ is the energy of the incident photon, B denotes the absorption edge width parameter and E_g denotes the band gap. Using Tauc plot analysis, the bandgap of the thin film is calculated by plotting of $(\alpha h\upsilon)^2$ versus hυ and by extrapolating the linear part of that graph, the bandgap value can be determined. Transmittance data can also be used to

calculate other optical properties such as extinction coefficient, dielectric constant and refractive index.

2.5 Electrical Characterization

To determine the electrical properties of the grown thin films, Au (100 nm)/Ti (50 nm) circular electrodes were deposited on the surface of the thin film through a shadow mask by electron beam deposition technique. After that, the fabricated devices were thermally annealed for 10 min at 450°C in an Ar atmosphere. The current-voltage (I-V) characteristics of the thin films were measured by means of a Keysight B1500A semiconductor device analyzer (figure 2.16) at room temperature.

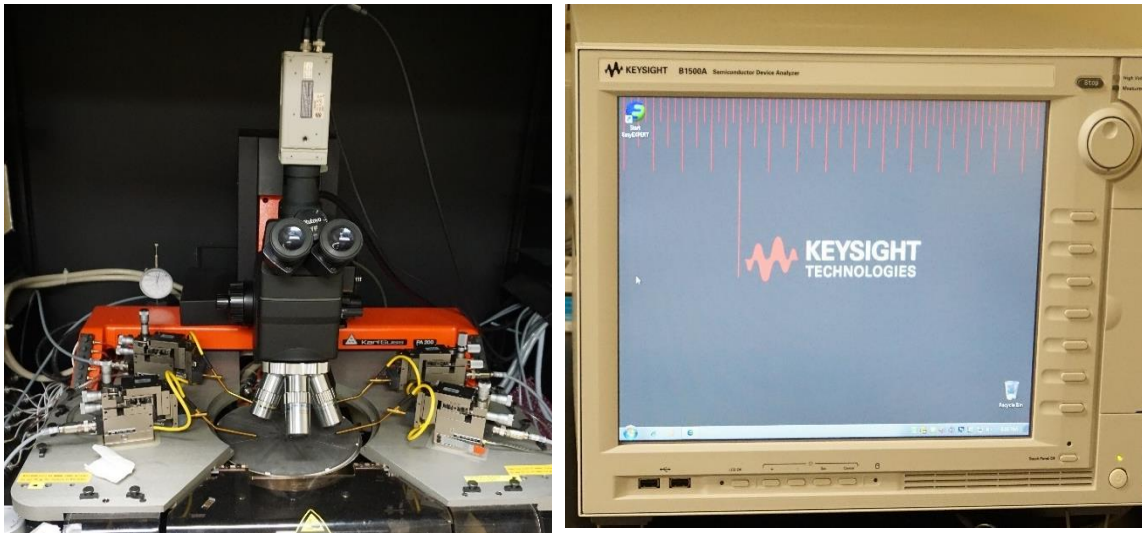

Figure 2.16: Keysight B1500A semiconductor device analyzer of Texas State University.

III. HETEROEPITAXIAL GROWTH OF β-Ga_2O_3 THIN FILMS

3.1 Introduction

The growth of Ga_2O_3 thin films requires a source of gallium and oxygen to completely oxidize the Ga atoms on the surface. This could be metallic Ga from an effusion source and a form of activated oxygen that is very reactive so that the oxidation can be completed at a low substrate temperature. In a conventional PAMBE technique, plasma-activated oxygen flux is used to oxidize evaporated gallium (Ga) flux on a heated substrate to form a layer of Ga_2O_3. Typically, oxygen-rich condition is used to provide an overpressure of oxygen to the growth surface for stoichiometry control during the growth of β-Ga_2O_3 whereas Ga-rich growth condition can be used for reducing Ga vacancies formation which act as compensating acceptors in β-Ga_2O_3 [122], [123]. The reactions for the formation of the film growth and suboxide are: $2Ga + 1O \rightarrow Ga_2O$ and $2Ga + 3O \rightarrow Ga_2O_3$. According to Vogt *et al*. [122], competition between the accumulation of Ga_2O_3 and desorption of volatile Ga_2O determine the growth rate of the film. Besides, the growth rate depends on the availability of oxygen species which constitutes a big challenge for the growth of thick layers of β-Ga_2O_3 by PAMBE [122]. To reduce the formation and desorption of Ga_2O an increase of oxygen flux is required. Also, the introduction of more reactive oxygen species such as ozone or plasma can reduce the desorption of Ga_2O and consequently increase the growth rate of the β-Ga_2O_3 film. However, there is a limitation on the partial pressure of oxygen that can be introduced into an MBE chamber, due to the risk of oxidation of filaments as well as exposure of the source materials in the effusion cells. To avoid this problem, the use of a Ga_2O_3 compound source would provide oxidized

Ga species to the growing surface in the form of Ga_2O which would remove the requirement for a high oxygen pressure necessary to oxidize metallic Ga at the surface. An analysis of the heats of formation suggests that the use of Ga_2O molecules and oxygen would result in the growth of the crystalline Ga_2O_3 thin films at a much lower temperature. It has been shown that, in comparison with using elemental Ga source, Ga_2O_3 compound source provides a relatively higher growth rate [10]. A similar technique was used for the growth of thick $BaSnO_3$ by MBE where SnO_2 source has been used instead of elemental Sn source to overcome the high overpressure of Sn and difficulty of incorporation into the ternary film [124]. Prior reports on the growth of an oxide thin film using Ga_2O_3 compound source with the films being amorphous [106], [125] were aimed for gate dielectric applications resulting in Fermi Level unpinning of GaAs surfaces. So, an in-depth study of the properties β-Ga_2O_3 thin films grown using a Ga_2O_3 compound source also the subject of this investigation. To complement the study of the properties of β-Ga_2O_3 thin films, a PLD technique was used because, unlike MBE where the oxygen partial pressure is limited during growth, oxygen partial pressure up to the millitorr level can be used. The increased oxygen pressure helps to maintain the stoichiometric composition of the films.

In this chapter, the growth and properties of high quality β-Ga_2O_3 epitaxial thin films on c-plane sapphire (Al_2O_3) substrates as a function of MBE growth parameters using a Ga_2O_3 compound source and an elemental Ga source is explored. In addition, because of the presence of oxidized Ga and oxygen from the source, the growth of single phase β-Ga_2O_3 using the compound source without the use of any additional oxygen will be investigated. In this approach, the required oxygen needed to form Ga_2O_3 will be obtained through the decomposition of the polycrystalline Ga_2O_3 source and transported to the

substrate surface along with the Ga_2O molecules. To the best of our knowledge there are no reports on the growth of crystalline β-Ga_2O_3 films without the use of an oxygen source by MBE. Part of this chapter also covers the growth and characterization of β-Ga_2O_3 epitaxial thin films by pulsed laser deposition technique.

3.2 Growth of β-Ga_2O_3 Using Ga Elemental Source by PAMBE

3.2.1. Experimental

Growth was carried out in an oxide MBE chamber with a base pressure of < 5×10^{-10} torr using a combination of turbomolecular and cryopumps. Oxygen was supplied from a RF plasma source with a DC bias on the deflector plate to minimize the ions from reaching the substrate. During growth, the chamber cryopanels were cooled with LN_2 with the cryopump valved off when the plasma source was used. The growth was monitored *in situ* using RHEED. In the study, β-Ga_2O_3 films were deposited on single-side polished quarter of 2" c-plane sapphire substrates by PAMBE technique. The sapphire substrate was degreased in acetone for 10 min and thermally cleaned for 15 min at 800° C in the growth chamber. In order to remove the adsorbates from the surface of the substrate, an additional oxygen plasma treatment was used for 40 minutes. To fabricate β-Ga_2O_3 thin films, Ga evaporated from an effusion cell with oxygen plasma generated through the radio frequency (RF) activated radical cell. In this study, substrate temperatures were varied from 650-750° C for Ga elemental source. The oxygen gas flow rate and the input RF plasma power of the radical cell were maintained at 1.24 sccm and 300 W respectively resulting in a chamber pressure of 1×10^{-5} torr during growth.

3.2.2 Results and Discussion

To investigate the surface quality and growth mode of β-Ga_2O_3 thin films, the

sample surface was monitored during growth by RHEED. Upon Ga_2O_3 nucleation on sapphire substrate, the RHEED pattern showed a diffuse background characteristics of amorphous material. As the growth keeps going, the diffuse RHEED pattern gradually became streaky showing a three-fold reconstruction with Kikuchi lines as shown in figure 3.1. The diffused background occurs during the transition from sapphire to Ga_2O_3 probably due to crystalline disorder. Streaky RHEED patterns were observed at the end of growth for all the samples grown at different substrate temperatures meaning that the film materials exhibit a high degree of structural order.

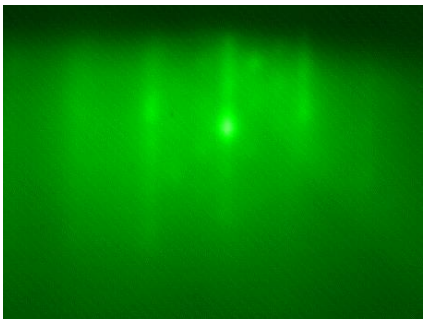

Figure 3.1: RHEED patterns during the growth of β-Ga_2O_3 using elemental Ga source.

To investigate the crystal structure of the grown β-Ga_2O_3 thin films, θ-2θ x-ray diffraction patterns were recorded in the 2θ range of 15-100°. Figure 3.2 shows XRD patterns of the films grown at various temperatures using elemental Ga source. The spectra contain four diffraction peaks corresponding to the $(\bar{2}01)$, $(\bar{4}02)$, $(\bar{6}03)$ and $(\bar{8}04)$ planes of β-Ga_2O_3 at 18.98°, 38.48°, 59.28°, and 82.30°. Apart from these peaks no other peaks representing other Ga_2O_3 phases were found in the scan range. This indicates that the thin films grown on c-plane sapphire represent a pure single phase $(\bar{2}01)$ oriented β-Ga_2O_3 similar to what was reported for β-Ga_2O_3 thin films grown on c-plane sapphire substrates, GaN substrates and a-plane sapphire substrates [53], [126]. For films grown with elemental

Ga, the spectra showed the same set of diffraction peaks when the growth temperature was increased from 650-750° C (figure 3.2). However, the peak intensity assigned to Ga_2O_3 increased with growth thickness as expected and which can be seen from the spectrum shown in figure 3.2 for the 3-hour growth at 700° C. The arrangement of oxygen atoms in the c-plane sapphire substrate is the same as in the $(\bar{2}01)$ plane of β-Ga_2O_3 resulting in the epitaxial relationship in which the $(\bar{2}01)$ β-Ga_2O_3||(0001) sapphire [53]. The gallium atoms bond to the oxygen atom layer of the sapphire substrate with smaller mismatch between the (0001) planes of the sapphire and the $(\bar{2}01)$ plane of β-Ga_2O_3 [126]. The peaks located at 41.78° and 90.88° are respectively the (006) and (0012) diffraction peaks of the c-plane sapphire substrate, respectively.

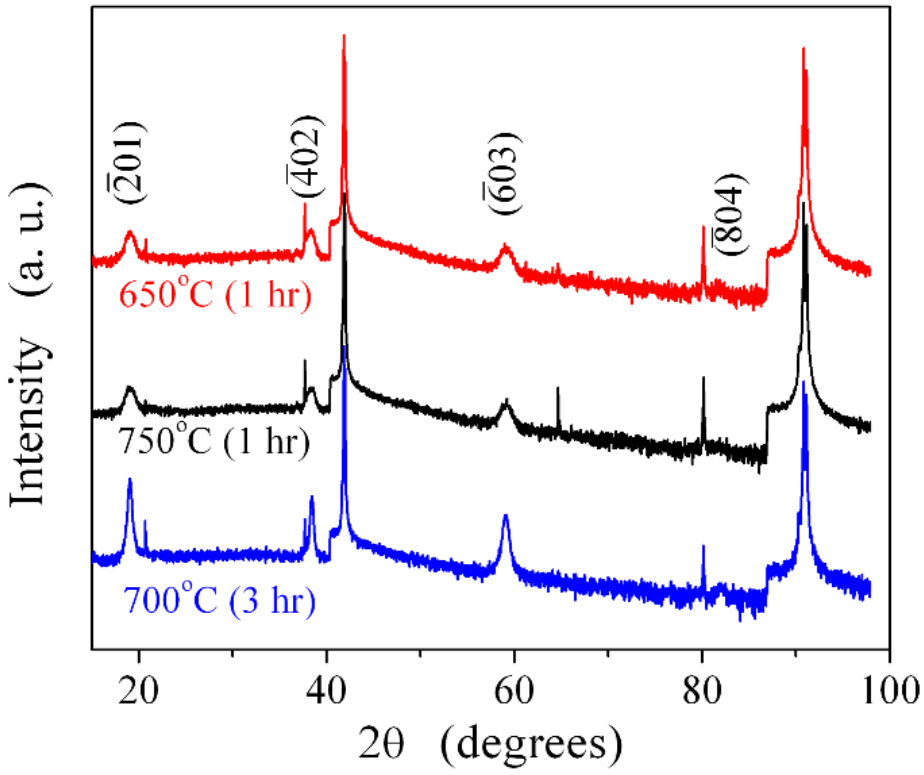

Figure 3.2: XRD patterns of β-Ga_2O_3 thin films grown using elemental Ga source.

To investigate the stoichiometry and oxidation state of the grown β-Ga_2O_3 thin films, x-ray photoelectron spectroscopy was used. Figure 3.3 shows a survey scan for the film grown using the Ga elemental source with only the oxygen peak and Ga related peaks. To determine the oxidation state of Ga, the Ga 2p region was selected and scanned in high resolution as shown in Fig. 3.4 for a Ga_2O_3 film grown using elemental Ga at a temperature of 700° C.

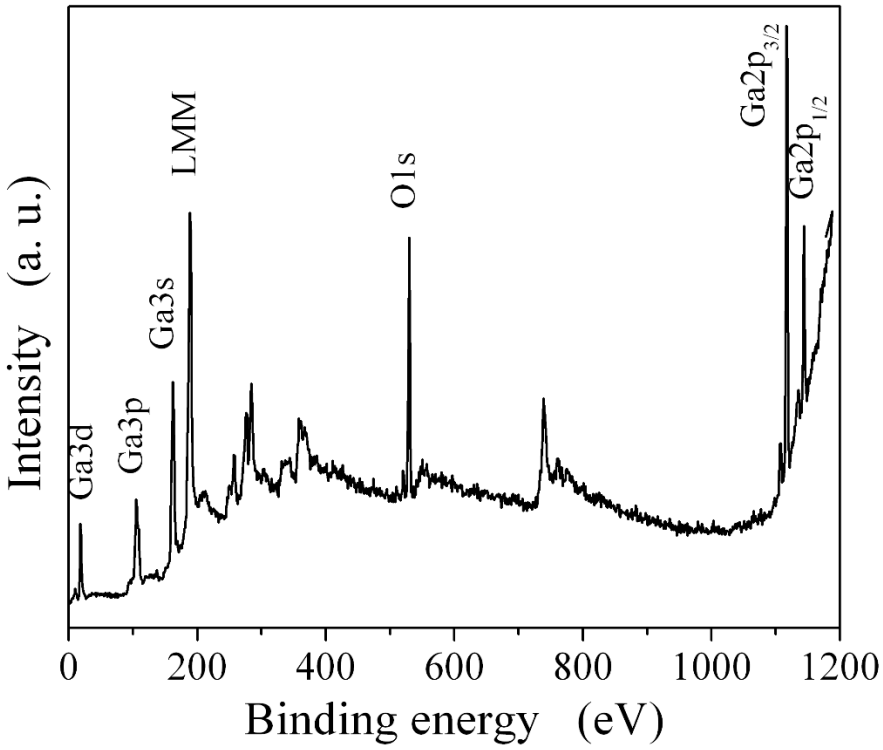

Figure 3.3: XPS survey scans of representative grown β-Ga_2O_3 films.

A sum of two Gaussian peaks on a Shirley background is used for the deconvolution of the XPS spectrum as shown in figure 3.4 The Ga 2p peak shown is a convolution of two peaks that can be assigned to Ga_2O_3 at 1117.32 eV and elemental Ga at 1116.03 eV. A positive shifting in binding energy of the Ga 2p peak indicates the Ga^{3+} oxidation state. Shifting of binding energy occurs because of the redistribution of electrons around the

constituent atoms of the crystal. So, the changes in chemical bonding results in shifting of binding energy which is used to infer information about the oxidation state of the Ga in the oxide film [106]. The elemental Ga in the Ga 2p peak is found because the totality of Ga was not oxidized by the provided oxygen. It is not possible to increase the oxygen pressure above 10^{-5} torr with the MBE technique because of this limitation all the Ga could not be oxidized resulting in a Ga-Ga peak in the Ga 2p scan (figure 3.4). Although the oxidation process is not 100% efficient, XRD results show the film possess a high degree of crystallinity (figure 3.2). The growth using elemental Ga requires higher temperatures for the complete oxidation of the Ga atoms based on the heat of formation.

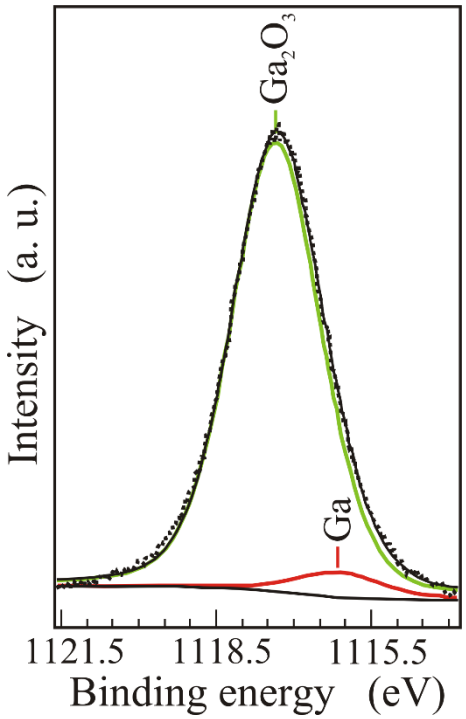

Figure 3.4: XPS of Ga 2p core level spectrum of a grown β-Ga_2O_3 thin films using elemental Ga source. Experimental data is represented by dotted lines.

Figure 3.5 shows a typical O 1s spectrum obtained from the grown films. This can be fitted with a single peak suggesting an oxide film where the Ga is in a predominantly single oxidation state.

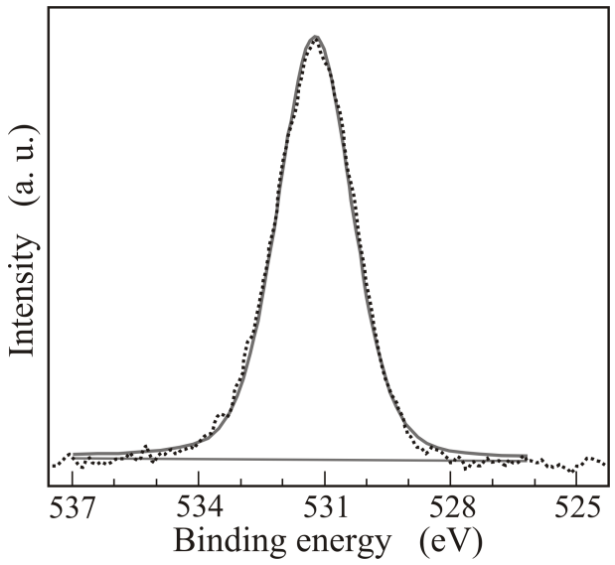

Figure 3.5: O 1s core level spectra of Ga_2O_3 thin films. Experimental data (solid squares) was fitted to a single peak (solid line).

Scanning probe microscopy (Park XE7) in the AFM mode was used to investigate the effect of the growth temperature on the surface morphology. AFM images were acquired at a scanning frequency of 1.5 Hz with a scanning area of 2×2 μm^2. Figure 3.6 shows the AFM topographies of the films surface grown by elemental Ga source at different growth temperatures. The morphological characteristics of thin films highly depends on the growth conditions, including growth temperature and oxygen partial pressure [126]. The surface of the thin films deposited by PAMBE were found flat and smooth without obvious cracks or discontinuities for both sources. The root mean square (RMS) surface roughness of the corresponding films grown using elemental Ga source with growth temperatures of 650, 700 and 750°C are 0.37, 1.11, 0.39 nm respectively [Fig. 3.6(a)-(c)] by PAMBE technique.

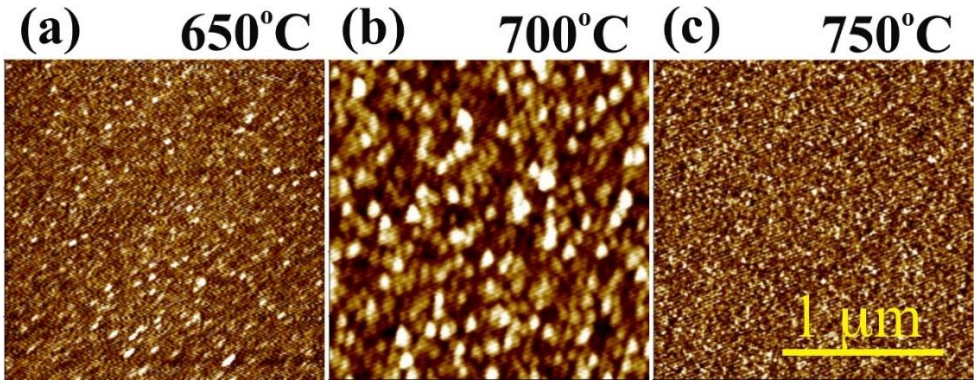

Figure 3.6: 2×2 μm^2AFM images of β-Ga_2O_3 films grown using elemental Ga source.

Optical properties such as the complex index of refraction, the dielectric constants, and the thickness of the films were analyzed using spectroscopic ellipsometry (SE) by determining the ellipsometric parameters Ψ and Δ as a function of wavelength (200-1000 nm) and incident angle (65°,70°, 75°, 80° and 85°) at room temperature. A model of the measured sample was constructed using a four layer structure (analysis software CompleteEase, J.A. Woollam) shown in figure 3.7b. In order to extract the optical properties of the thin film with respect to a substrate/film structure, the optical response of the c-plane Al_2O_3 substrate was first determined and used in the model to determine the optical properties of the β-Ga_2O_3 thin film. Subsequently, the measured ellipsometric data was fitted to the corresponding optical model generated data, depicted in figure 3.7(a). A minimum root mean square error (RMSE) is obtained by varying the parameters of the model during the fitting procedure expressed as [42]:

$$RMSE = \sqrt{\frac{1}{2n-m-1}\sum_{i=1}^{n}\left[(\Psi_i^{cal}-\Psi_i^{exp})^2+(\Delta_i^{cal}-\Delta_i^{exp})^2\right]}$$

Here, n is the number of data points in the spectra, m is the number of variable parameters in the model, and 'exp' and 'cal' denote the experimental and calculated data, respectively.

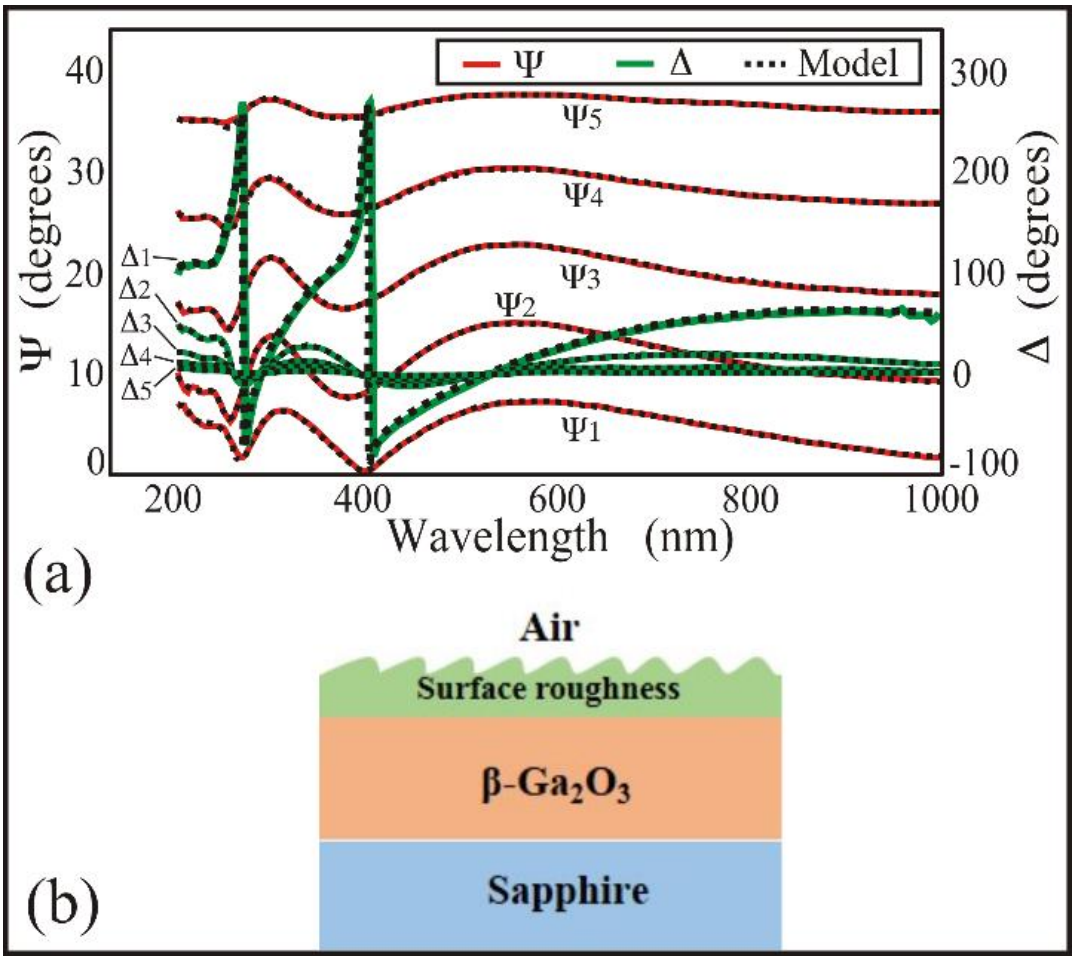

Figure 3.7: (a) Raw SE data (experimental-colored lines) and the corresponding calculated fittings (black dotted lines) as a function of wavelength. Curves Δ_1 and Ψ_1 were taken at an incident angle of 65°, Δ_2 and Ψ_2 at 70°, Δ_3 and Ψ_3 at 75°, Δ_4 and Ψ_4 at 80°, Δ_5 and Ψ_5 at 85°. (b) Four layer model structure for β-Ga_2O_3.

Figure 3.7(b) sketches a four-medium optical model consisting of a semi-infinite c-plane Al_2O_3 substrate/β-Ga_2O_3 film/surface roughness/air ambient structure employed to investigate the β-Ga_2O_3 thin film. The roughness layer was included to simulate the effect of surface roughness of the β-Ga_2O_3 film on the SE measurement. Since the optical constants for the c-plane Al_2O_3 substrate layer have been obtained separately, the free

parameters in the fitting correspond to the β-Ga_2O_3 film thickness, surface roughness layer thickness and the β-Ga_2O_3 optical constants. The β-Ga_2O_3 optical constants are described by the Cauchy dispersion relation model while the surface roughness layer is modeled by a Bruggeman effective medium approximation using a mix of 50% β-Ga_2O_3 and 50% voids [127]. The β-Ga_2O_3 film and surface roughness layer thicknesses are consistent with the profilometer and the AFM RMS roughness measurement respectively.

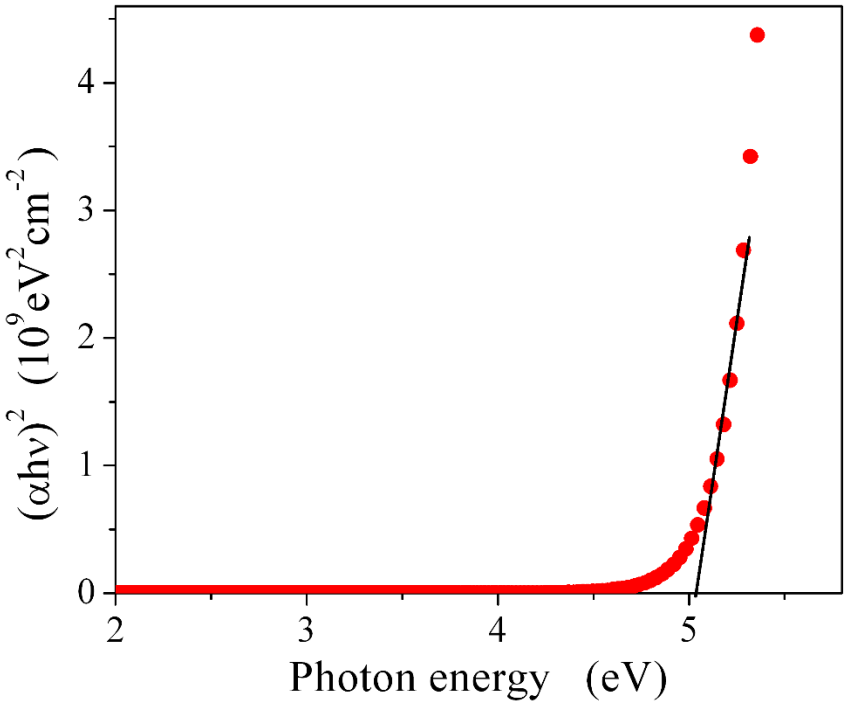

Figure 3.8: Plot of $(\alpha h\nu)^2$ vs photon energy for a β-Ga_2O_3 epilayer deposited on sapphire at 750°C. The optical direct bandgap is estimated by extrapolation to $h\nu = 0$.

In order to derive the quantitative structure-property relationship to better understand the effect of microstructure on the optical properties, a further analysis of the measured optical spectra is performed, shown in figure. 3.8. The absorption of β-Ga_2O_3 follows a power law, since it has a direct band gap expressed as [127]:

$$(\alpha h\upsilon) = B(h\upsilon - E_g)^{1/2}$$

where $h\upsilon$ is the energy of the incident photon, α is the absorption coefficient, B is the absorption edge width parameter and E_g is the bandgap.

It is evident that in the high absorption region, $(\alpha h\nu)^2$ vs $h\nu$ results in a linear plot, suggesting direct allowed transitions across the energy gap of β-Ga_2O_3 films [46], [127] with the band gap values determined by extrapolating the linear region of the plot to $h\nu = 0$. The bandgap found from a film grown at 750°C using the elemental Ga source is ~5.02 eV indicating an excellent optical transparency of the thin film in the UV and visible wavelength region. The corresponding refractive index, n (at a wavelength of 6328 Å) calculated from SE data for this same film is ~1.77 eV. It is worth noting that the measured band gap energy values and the refractive indices in this work are consistent with those reported in the literature for β-Ga_2O_3 [42], [127]. A summary of the derived samples parameters is presented in Table 3.

Table 3. Material characteristics of Ga_2O_3 thin films grown using elemental Ga source.

Growth temperature (°C)	**Thickness (nm)**	**RMS roughness (nm)**	**Band gap (eV)**	**Refractive index at 632 nm**
650	23.22	0.37	4.96	1.76
700	22.64	1.11	4.98	1.77
750	23.22	0.39	5.02	1.77

3.3 Growth of β-Ga_2O_3 Using Ga_2O_3 Compound Source by MBE

3.3.1 Experimental

Heteroepitaxial β-Ga_2O_3 films were grown on single-side c-plane sapphire substrates by MBE. In the present work, compound a polycrystalline Ga_2O_3 source material

(99.999%) evaporating from an iridium crucible in a high temperature effusion cell has been used to investigate the influence of the growth parameters including substrate temperature and oxygen pressure with activated oxygen generated through an RF plasma source. The heteroepitaxial growth of β-Ga_2O_3 using the compound source follows the next reactions:

$$Ga_2O_3 \xrightarrow{heat\ to\ 1750℃} Ga_2O + O_2$$

$$Ga_2O + 2O \rightarrow Ga_2O_3 \text{ or } Ga_2O + O_2 \rightarrow Ga_2O_3$$

The thermal decomposition of the Ga_2O_3 compound source material provides both Ga_2O and oxygen molecules. The oxygen deficiency found in the Ga_2O_3 films grown by means of the elemental Ga source is expected to be drastically reduced when using the compound source since there is no requirement to oxidize metallic Ga atoms. A set of growths was carried out at various substrate temperatures ranging from 500 to 850°C. The crystallinity of the films was monitored *in-situ* using reflection high energy electron diffraction (RHEED) and confirmed by *ex-situ* x-ray diffraction measurements. The chamber pressure was kept at 1×10^{-5} torr during growth which was limited to the partial pressure of the Ga_2O and O_2 species resulting partially from the decomposition of the compound source. In addition, an oxygen flow rate of about 1.2 sccm with the input RF plasma power of 300W was used to supply the additional oxygen. β-Ga_2O_3 thin films were also deposited without any oxygen source on sapphire substrate at substrate temperature of 700°C with the chamber pressure of 5×10^{-6} torr to demonstrate that the compound source provides sufficient oxygen for the nucleation of a crystalline Ga_2O_3 film.

3.3.2 Results and Discussion

The out-of-plane 2θ-ω XRD scans of the Ga_2O_3 thin films grown at various

substrate temperatures using the compound Ga_2O_3 source with a fixed oxygen pressure are shown in figure 3.9 (a). The spectrum taken from Ga_2O_3 layer deposited without any additional oxygen is also shown. At a growth temperature of 500°C, the Ga_2O_3 film appears to be amorphous as evidenced from the XRD spectrum in which the only diffraction peaks are those from the sapphire substrate. A diffuse RHEED pattern during the growth also confirmed this statement. At deposition temperatures ≥ 600°C, the XRD spectra exhibit a set of diffraction peaks located at 18.98°, 38.48°, 59.28° and 82.30° which can be indexed to $(\bar{2}01)$, $(\bar{4}02)$, $(\bar{6}03)$ and $(\bar{8}04)$ planes of β-Ga_2O_3 indicating pure single $(\bar{2}01)$ oriented thin films growth on the c-plane sapphire substrate. This is in agreement with previous reports where β-Ga_2O_3 thin films were grown on c-plane sapphire, a-plane sapphire and GaN substrates [10], [45], [53]. During the growth of β-Ga_2O_3, the gallium atoms bond to the interfacial oxygen atom layer of the sapphire substrate resulting in a better lattice matching between the $(\bar{2}01)$ plane of β-Ga_2O_3 and the (0001) plane of the sapphire [27]. It is worth noting that, there is a possibility of an α-Ga_2O_3 phases to exist since (0006) plane of α-Ga_2O_3 overlaps with the $(\bar{4}02)$ diffraction peak of β-Ga_2O_3 located at 38.48° in the XRD spectrum. According to Oshima *et al.* [128] this can be clarified by examining the ratio of the intensity between the $(\bar{2}01)$ and $(\bar{4}02)$ peaks in the spectrum where the peak corresponding to $(\bar{4}02)$ would be higher than the peak corresponding to $(\bar{2}01)$, if α-Ga_2O_3 (0006) was present. Typically α-Ga_2O_3 phase would be observed at low growth temperatures [49], [128]. At 750°C, the intensity ratio $((\bar{2}01)/(\bar{4}02))$ experimentally found was 2.17 but as growth temperature was decreased this ratio gradually decreased to a value of 0.37 at 600°C. Taking into account the program Powder Cell 2.4 calculation (mentioned in ref [128]), the ideal value of this ratio for a pure β-Ga_2O_3 phase is 2.2. While

at higher growth temperatures the experimental value is close to the ideal intensity ratio, it deviates to lower values when the growth temperature is lowered [51], [129] suggesting an partial formation of the α-Ga_2O_3 phase.

An analysis of the spectra in the figure 3.9 (a) shows a strong dependency of the thickness and phase of the Ga_2O_3 films on growth temperatures above 600°C. Higher substrate temperatures are required for the growth of stable single phase β-Ga_2O_3 possibly due to insufficient energy and mobility of surface adatoms at lower temperature. With the growth temperature of 700-750°C, the high intensity of the planes of β-Ga_2O_3 suggested that enough thermal energy is supplied to the molecules and atoms to increase the surface mobility leading to a $(\bar{2}01)$ crystal orientation. The intensity of the $(\bar{2}01)$ peak and higher order diffraction peaks of β-Ga_2O_3 decreased when the growth temperature is increased to 850°C which may be due to a decrease in film thickness caused by the reduction of the sticking coefficient of the volatile Ga_2O molecules [122]. The decrease in film thickness at this elevated growth temperature was confirmed by spectroscopic ellipsometry measurements. High resolution XRD scans around the $(\bar{2}01)$ plane of β-Ga_2O_3 were performed on the films grown at 700 and 750°C. The corresponding full widths at half maxima (FWHM) are 0.235 and 0.233° respectively. Sharp diffraction peaks are indicative of high crystalline material quality. Figure 3.9 (b) shows the high resolution XRD spectrum for the film grown at a substrate temperature of 700°C. High crystalline Ga_2O_3 films quality was obtained with FWHM comparable to reported values [45], [49]. The crystallinity was further confirmed during growth by monitoring RHEED patterns exhibiting a streaky threefold reconstruction (figure 3.9(b) inset) indicative of epitaxial growth.

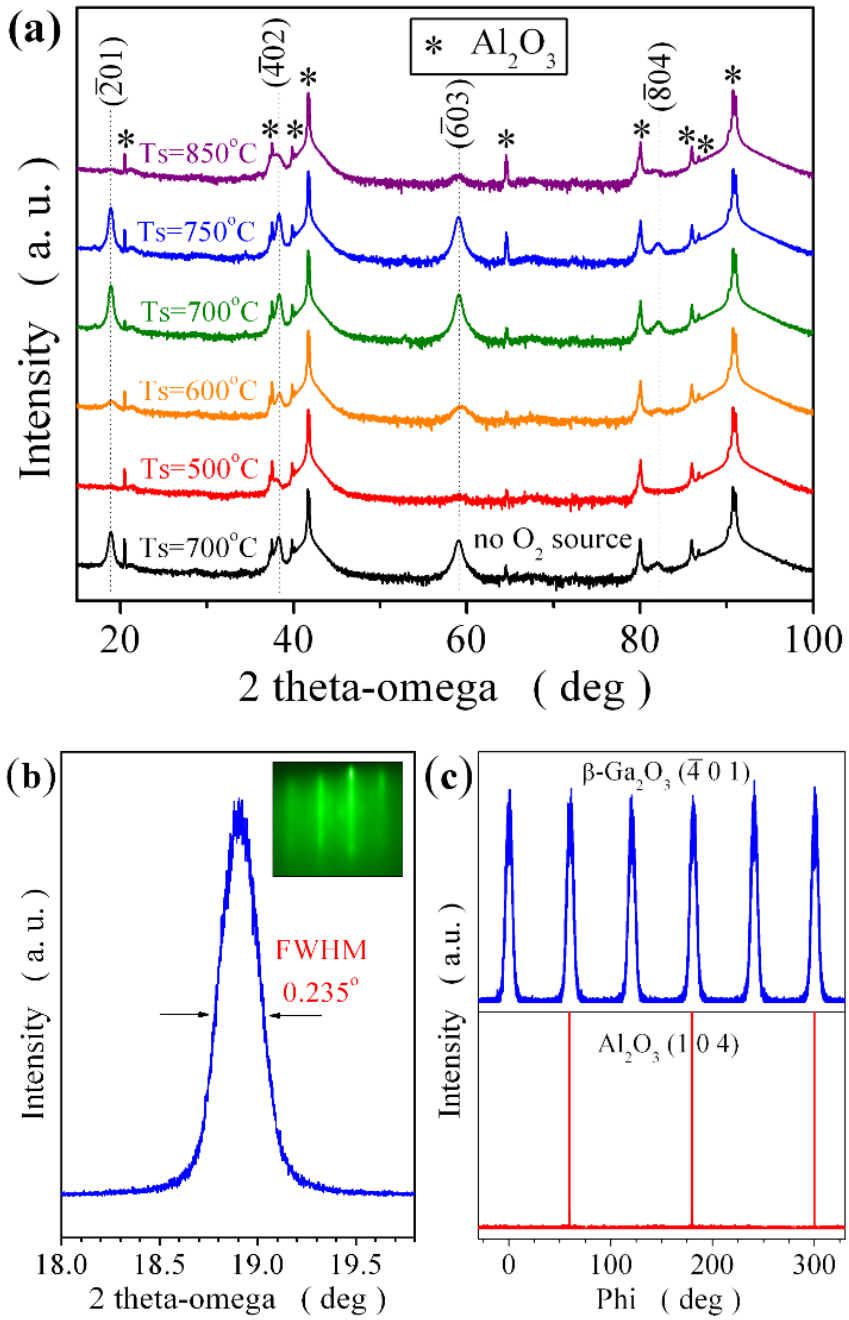

Figure 3.9: (a) XRD 2theta-omega (2θ-ω) spectra of Ga_2O_3 thin films grown at various substrate temperatures on sapphire substrate. Peaks marked as ∗ belong to sapphire (Al_2O_3) substrates; (b) High resolution X-ray rocking curve for $(\bar{2}01)$ plane of β-Ga_2O_3 thin film grown at 700°C. The inset shows a RHEED pattern taken during the growth; (c) XRD Φ-scan for $\{\bar{4}01\}$diffraction peak of β-Ga_2O_3 grown at 700°C substrate temperature with the Φ-scan for {104} diffraction peak of Al_2O_3 substrate.

To determine the epitaxial relationship between β-Ga_2O_3 and the Al_2O_3 substrate, in-plane XRD Φ (phi) scan has been measured for the $\{\bar{4}01\}$ diffraction of β-Ga_2O_3 thin film and the {104} diffraction of the Al_2O_3 substrate shown in figure 3.9 (c) for the growth at 700°C. The Φ scan at $\{\bar{4}01\}$ diffraction plane shows six peaks which are 60° apart from each other indicating the presence of a sixfold in-plane rotational symmetry for β-Ga_2O_3 thin film. However, monoclinic β-Ga_2O_3 $\{\bar{4}01\}$ diffraction planes have two fold in-plane rotational symmetry. It can be concluded that, the grown film contains in-plane rotational domains. Due to the threefold rotational symmetry of the c-plane sapphire (Al_2O_3) surface, it can be concluded that the originally twofold β-Ga_2O_3 films grew epitaxially in the three different directions at the same rates, resulting in the sixfold rotational symmetry [49], [128]. Also shown in figure 3.9 (a), there is an XRD scan for Ga_2O_3 grown at 700°C using the compound oxide source with no additional oxygen, suggesting that the decomposition of the oxide source provides sufficient oxygen necessary for the crystallization of the Ga_2O_3 layer. An examination of the XRD spectra indicates that the crystaal quality of the layers grown with and without oxygen appears to be comparable.

Figure 3.10 (a) shows the low-magnification HAADF image of the β-Ga_2O_3 thin film grown on Al_2O_3 substrate at 700°C. The magnified HAADF image (figure 3.10 (b)) shows that the Ga_2O_3 thin film is single-crystallized. β phase of Ga_2O_3 has been further confirmed by the selected-area electron diffraction patterns along [010] axis shown in figure 3.10 (d) which also confirms the epitaxial growth of the film with orientation relationship of $(\bar{2}01)$β-Ga_2O_3||(0001) Al_2O_3. The atomic-resolution HAADF and ABF (allows observation of oxygen atoms) images (figure 3.10 (e) and 3.10 (c)) are obtained simultaneously and show a sharp interface between Ga_2O_3 and Al_2O_3 without any

precipitation. Energy dispersive spectroscopy (EDS) line scan profile of the yellow arrowed line shown in figure 3.10 (e) across the Ga_2O_3/ Al_2O_3 interface was obtained to investigate the compositional distribution of the Ga_2O_3 thin film [figure 3.10 (f)]. From the EDS line scan, along with the HAADF image, it can be seen that Ga atoms are uniformly distributed in the film and there is no noticeable phase separation or metal agglomerated areas that can be detected. Additionally, the analysis of the STEM images indicates no evidence of α-Ga_2O_3.

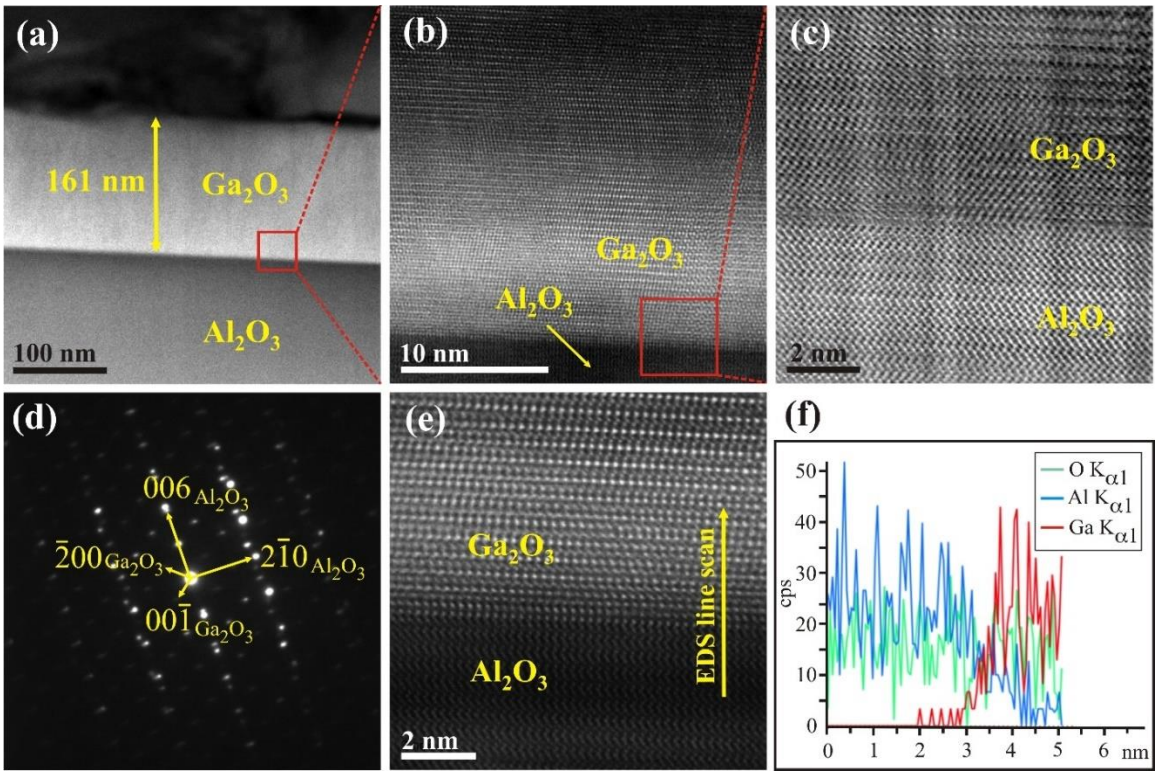

Figure 3.10: (a) Low magnification cross-sectional STEM-HAADF image of Ga_2O_3/Al_2O_3 heterostructure; (b) STEM-HAADF image of Ga_2O_3/Al_2O_3 interface in high magnification; (c) Atomic-resolution HAADF images of the Ga_2O_3/Al_2O_3 interface taken from (b) as marked by a red small square; (d) The SAED pattern of Ga_2O_3 thin film; (e) STEM-HAADF image of Ga_2O_3/Al_2O_3 interface; (f) The EDS line scan profile of the yellow arrowed line shown in (e).

X-ray photoelectron spectroscopy (XPS) was employed to analyze the

stoichiometry and chemical valence state (i.e. oxidation state) of β-Ga_2O_3 films deposited on sapphire substrate using the compound Ga_2O_3 as the source material in the two growth schemes: with oxygen and without additional oxygen. The Ga 3d spectra shown in figure 3.11 and 3.12 were taken immediately after deposition and without exposure to air since the sample can be transferred to the spectroscopy chamber under UHV. In this way, any artifacts due to air exposure can be eliminated.

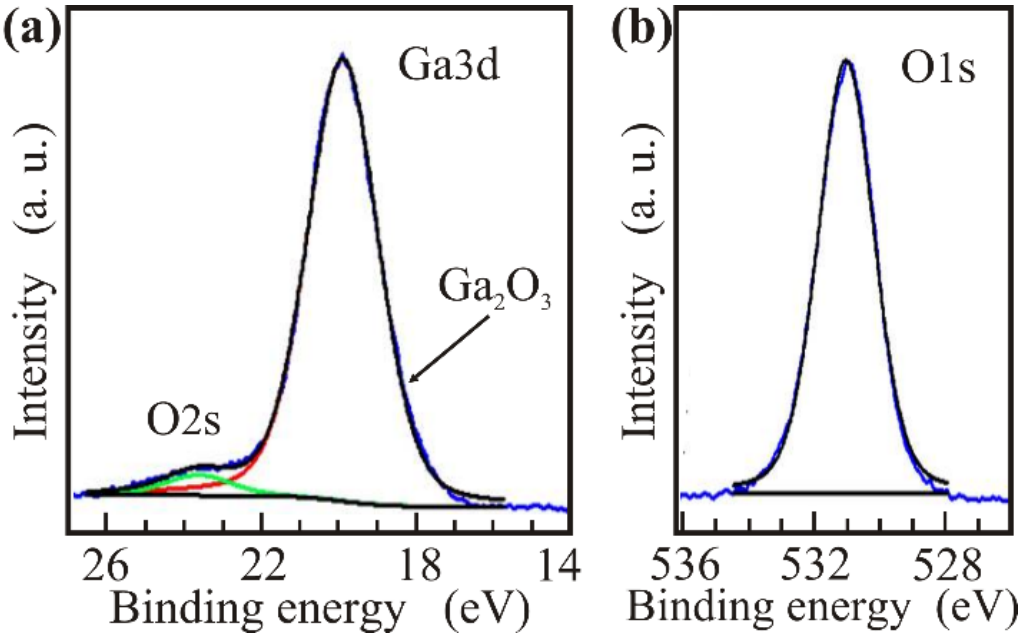

Figure 3.11: (a) Ga 3d core level high resolution spectrum of β-Ga_2O_3 thin films grown at 750°C with additional oxygen which shifts towards higher BE compared to metallic Ga represents Ga^{3+} state. (b) O 1s core level spectra of Ga_2O_3 thin films. Blue lines denote experimental data and fitting results represented by black lines. Both fitted to single peak indicates stoichiometric composition.

The deconvolution of XPS spectra were carried out by employing a Gaussian function on a Shirley background. From figure 3.11 (a), it is clear that the measured Ga 3d peak can be fitted with a single peak at the binding energy (BE) of 19.89 eV assigned to Ga_2O_3 when grown at a substrate temperature of 750°C using oxygen plasma. The additional peak observed at 23.61 eV represents the O 2s peak. While the growth of

crystalline Ga_2O_3 can be accomplished without the use of additional oxygen when using the compound source, there is some evidence of metallic Ga in the film as can be seen from the Ga 3d spectrum in figure 3.12 (a). This spectrum is composed of two peaks apart from the O 2s peak (centered at 23.22 eV) which are attributed to Ga_2O_3 recorded at 20.05 eV and metallic Ga at 18.44 eV. In both cases a positive shifting in BE is observed for Ga_2O_3 films indicating a Ga^{3+} oxidation state.

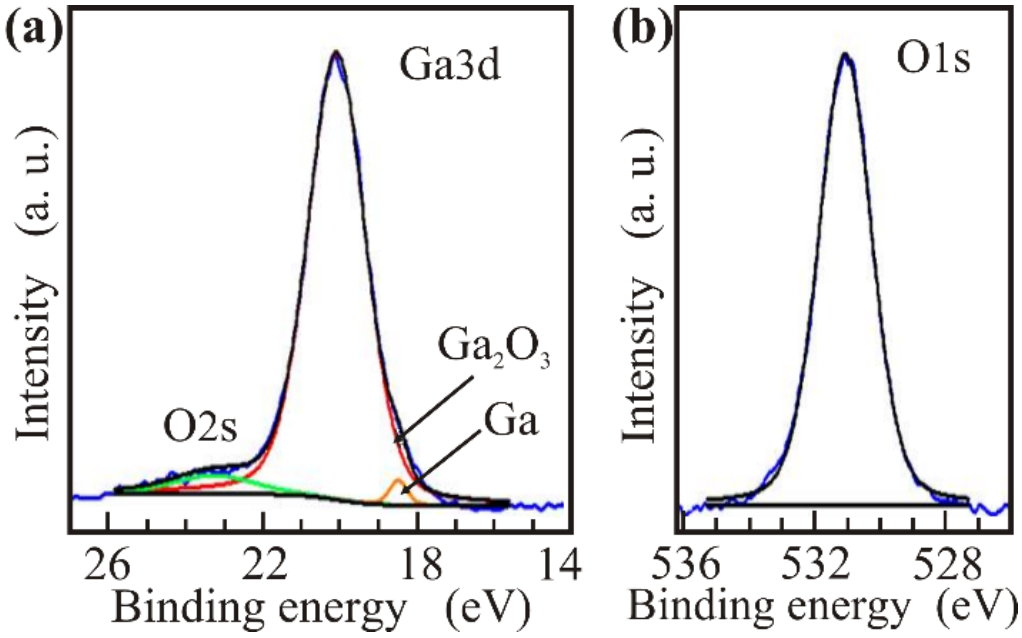

Figure 3.12: (a) Ga 3d core level high resolution spectrum of β-Ga_2O_3 thin films grown without oxygen source which is a convolution of two peaks represent Ga^{3+} state and Ga^0 state. (b) O 1s core level spectra of Ga_2O_3 thin films which is fitted to single peak. Blue lines denote experimental data and fitting results represented by black lines.

Based on the XPS analysis (figure 3.11 (a)), it can be said that it is possible to grow stoichiometric Ga_2O_3 thin films on sapphire substrate employing Ga_2O_3 compound source under optimized growth conditions which includes the use of the oxygen source because in this growth scheme, oxidized Ga is provided through compound Ga_2O_3 source. On the other hand, when Ga elemental source was used, the oxidation process was inefficient in

the growth conditions window explored in this work leading to a Ga-Ga XPS peak and a growth rate reduction (figure 3.4). When growing using the compound source without additional oxygen, the films were observed to be slightly Ga rich as expected (figure 3.12 (a)) as there is insufficient oxygen to sustain the $Ga_2O + 2O \rightarrow Ga_2O_3$ reaction resulting in the extra XPS peak assigned to Ga-Ga bonding.

Figure 3.11 (b) and 3.12 (b) show O1s core level photoelectron spectra measured from the grown films. These spectra consist of a single peak indicative of films which are composed of Ga with a predominantly single oxidation state.

In order to visualize the growth temperature influence on surface morphologies and roughness of β-Ga_2O_3 thin films grown by PAMBE, AFM micrographs were taken on various samples grown at different substrate temperatures shown in figure 3.13. AFM images were obtained over a 5×5 μm^2 scanning area at 1.5 Hz scanning frequency. They show a flat granular shape surface morphology with relatively low root mean square (rms) roughness (Table IV). PAMBE grown thin films show flat and smooth surfaces without noticeable cracks or discontinuities. Several authors reported a strong dependency of surface morphology on the growth temperature and oxygen partial pressure [10], [49], [130]. Based only on a growth temperature variation analysis at a fixed oxygen pressure, the surface morphology did not change considerably in the samples, figure 3.13 (a-d). However, at the highest substrate temperatures (850°C), the surface roughness decreased significantly. This can be understood in terms of an increased mobility of adatoms on the surface accompanied by a decrease of the film thickness and growth rate due to reduction of sticking coefficient of Ga_2O molecules [122]. The sample grown at the lowest temperature (500°C) exhibited a lower roughness but lacked a good structural quality

according to the XRD characterization shown in figure 3.9.

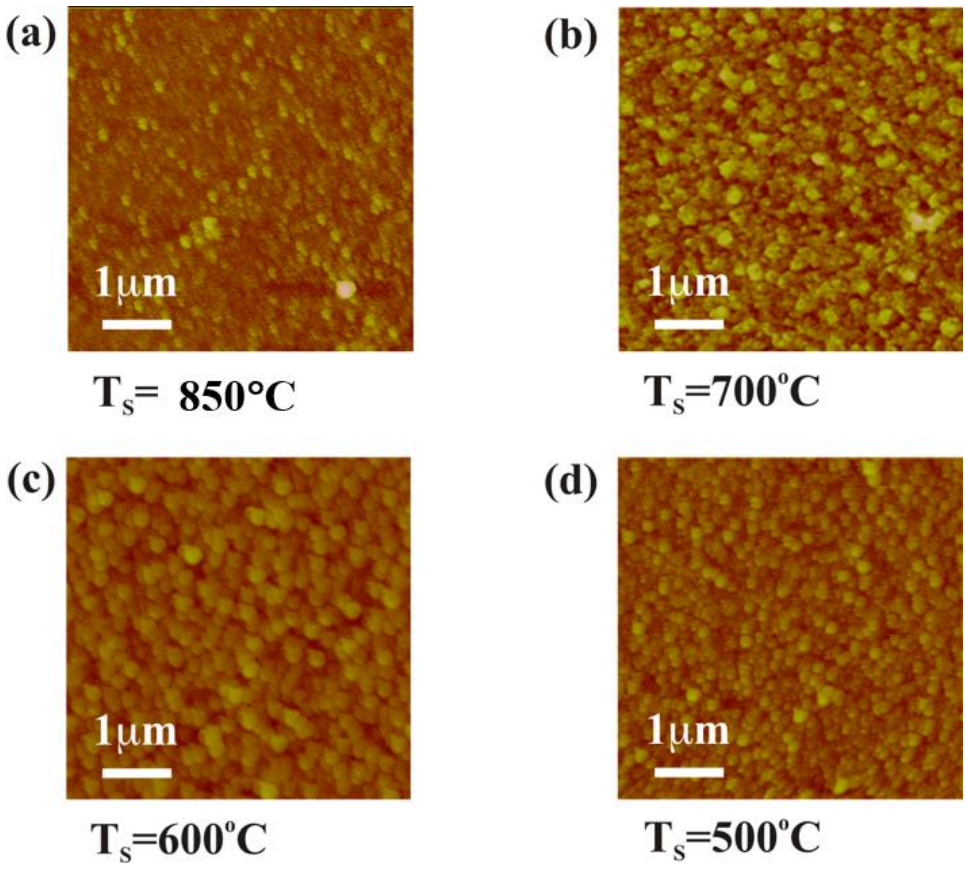

Figure 3.13: 5×5 μm^2 surface AFM images of β-Ga_2O_3 epitaxial films grown at various substrate temperatures.

In order to investigate the optical properties of β-Ga_2O_3 thin film, UV-Vis measurements were carried out. Figure 3.14 shows a plot of the transmittance spectrum vs. wavelength of the film prepared at a substrate temperature of 700°C showing a good optical transparency and exhibiting clear fringes in the visible and UV regions. The fringes are the results of thicker films. The light continuously goes under minor constructive and destructive interference on its way through the sample. This is observed only in thick films due to its small refractive index variation along thickness. The amorphous Ga_2O_3 films (grown at 500°C) exhibit (not shown in figure) increased transparency over the whole

spectra except at the band edge where absorption of the incident radiation becomes more apparent [130]. This is a very important feature for specific application such as antireflection and dielectric coatings of solar cells [131]. To formulate a quantitative structure-property relationship and to understand the microstructural effect on the optical properties, an analysis of the transmission spectra is also performed. Since β-Ga_2O_3 is a direct band gap material [49], [127], [132] the absorption spectra obey a power law of the form

$$(\alpha h\nu) = B(h\nu - E_g)^{1/2}$$

where hν is the incident photon energy, α the absorption coefficient, B the absorption edge width parameter, and E_g the band gap. The optical absorption coefficient could be determined as [130]:

$$\alpha = [1/t] ln[T/(1-R)^2]$$

where T is the transmittance, R the reflectance, and t the film thickness. A plot of $(\alpha h\nu)^2$ vs hν plots show (figure 3.14 inset) a linear relationship in the high absorption region which suggesting a direct bandgap for the Ga_2O_3 films [127], [132]. whose values could be found by extrapolating the liner region of the plot to hυ = 0. The E_g variations for Ga_2O_3 films grown at various substrate temperature are shown in Table IV. The E_g values of the grown Ga_2O_3 films are around 5 eV with the amorphous film grown at 500°C showing showing the highest E_g value of 5.1 eV. The obtained higher values of E_g at low temperature for Ga_2O_3 films may be due to the non-stoichiometric and/or amorphous nature which could contribute to disorder, leading to a slightly higher band gap measured for the films grown at 500°C, in agreement with previous studies [130]. The calculated bandgap energies obtained in this study are comparable with previously reported values for β-Ga_2O_3 [27],

[127], [128], [132].

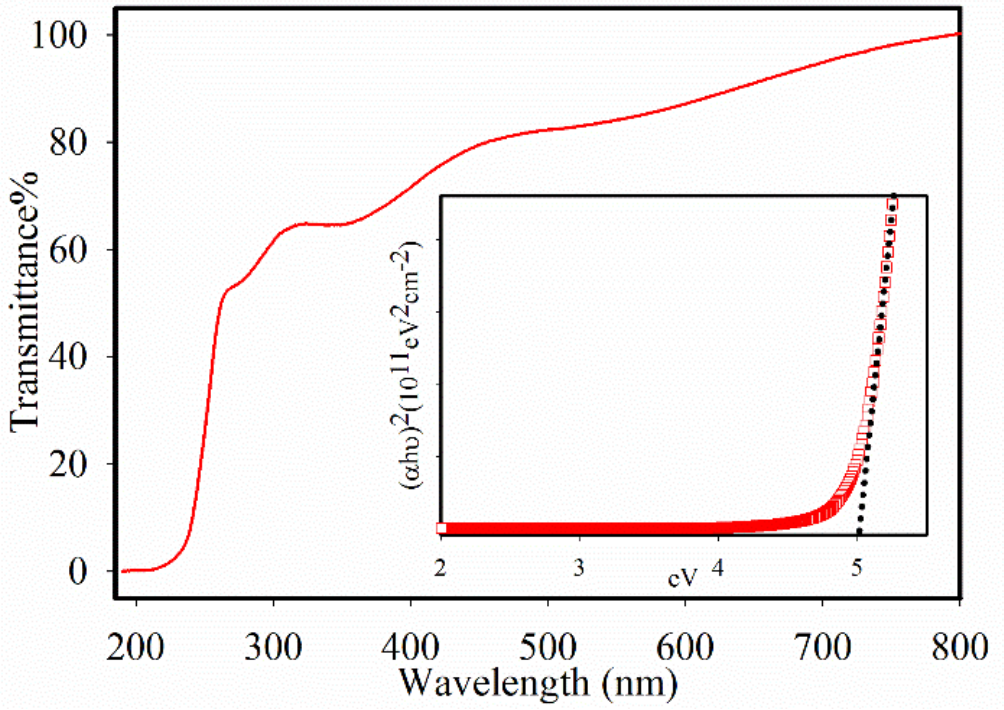

Figure 3.14: Transmission spectrum of Ga_2O_3 thin film grown at 700°C. The inset is a plot of $(\alpha h\upsilon)^2$ vs photon energy at different substrate temperature where α and $h\upsilon$ represent the absorption coefficient and photon energy, respectively. By extrapolating α to 0, the optical bandgap was obtained.

The complex index of refraction and thickness of the films were measured by obtaining the ellipsometric parameters Ψ and Δ at room temperature for different wavelengths (200-1000 nm) and incident angles (65°-85° with 5-degree interval). An optical model based on regression analysis and the Mean Squared Error (MSE) were used to determine the refractive index, film thickness and surface roughness. The details of the fitting and modelling could be found in previous section. The measured film thicknesses and calculated refractive index (n) (at a wavelength of 6328 Å) for β-Ga_2O_3 films are both compiled in Table 4. The thickness and the modelled surface roughness of the films showed consistency with the measured results from profilometer and values of rms roughness from

the AFM measurement respectively. The resulting refractive indixes are closely related to the film growth temperature. The lowest value (1.79) was obtained for the growth at 850°C is probably due to the decrease in film thickness. The rerfactive index monotonically increased up to 1.92 when the substrate temperature was decreased to 500°C. It is worth noting that the refractive indixes in this work are in agreement with reported values in the literature for β-Ga_2O_3 [27], [42], [128]. Thus, films with greater refractive index exhibit a higher bandgap energy are structurally more amorphous and transparent to UV light.

Table 4: Material characteristics of Ga_2O_3 thin films grown at various substrate temperature.

Substrate Temperature (°C)	Bandgap (eV)	Thickness (nm)	Refractive index at 632 nm	RMS Roughness (nm)
850	4.98	15.89	1.79	0.88
750	5.03	150.5	1.89	3.07
700	5.02	161.0	1.91	2.71
600	5.05	33.75	1.90	3.40
500	5.10	26.23	1.92	1.75

3.4 Growth of β-Ga_2O_3 by PLD

3.4.1 Experimental

As observed during the growth by MBE, the properties of the β-Ga_2O_3 thin films are influenced by both the substrate temperature and oxygen pressure. Therefore, using PLD in which there is a wider range of growth conditions possible, an investigation of the film properties will be studied and compared to those grown by MBE. β-Ga_2O_3 thin films were grown on c-plane sapphire substrate (a quarter of 2-inch wafer) with a stoichiometric ceramic Ga_2O_3 target (99.999% purity) as the source. Prior to growth, the sapphire substrate was cleaned with organic solvents (acetone and isopropanol alcohol)

ultrasonically and then rinsed in deionized water and blow dried with nitrogen gas. To explore the influence of the substrate temperature and oxygen pressure on the growth, the substrate temperatures and oxygen pressures were varied from 400 to 800°C and 1×10^{-3} to 1×10^{-1} torr respectively. As an ablation source, a KrF excimer laser (λ=248 nm) was used with fixed repetition rate of 10 Hz and laser power of 200 mJ. During growth, the target and the substrate were rotated for film uniformity and the target-substrate distance was fixed at 5 cm for the. A post growth annealing was performed at 700°C temperature in the absence of oxygen.

3.4.2 Results and Discussion

The substrate temperature and oxygen pressure have different roles in a PLD depositions process. The effect of substrate temperature is identical to other growth processes such as increased surface atoms mobility with high substrate temperature which can result in the structure of the films having improved crystallinity. The purpose of oxygen is to supply the necessary atoms needed for oxidation of the anions and influencing the shape of the plume during growth.

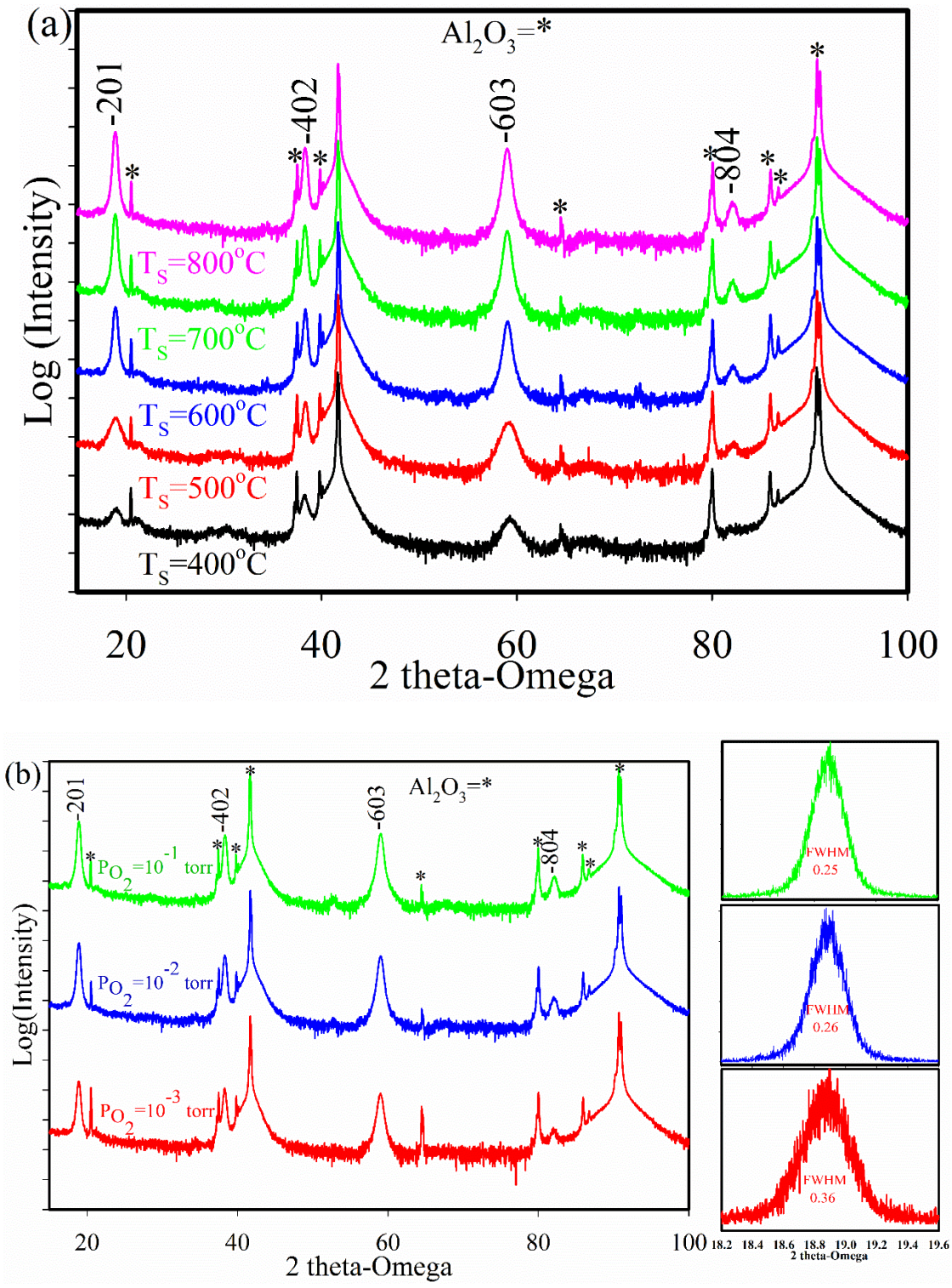

Figure 3.15: XRD measurements of β-Ga_2O_3 thin films grown by PLD for (a) substrate temperature (T_S) from 400-800°C, (b) oxygen pressure (P_{O_2}) from 10^{-3}-10^{-1} torr.

Figure 3.15 (a) shows the XRD measurements for the β-Ga_2O_3 thin films at various substrate temperatures (T_S) from 400-800°C with an oxygen pressure of 10^{-2} torr while figure 3.15 (b) shows the XRD sprectra at various oxygen pressure (P_{O_2}) from 10^{-3} to 10^{-1} torr with the substrate temperature of 800°C grown on sapphire substrate. Figures 3.15 show the films are epitaxially grown $(\bar{2}01)$ oriented on the substrate as the only diffraction peaks found correspond to $(\bar{2}01)$, $(\bar{4}02)$, $(\bar{6}03)$ and $(\bar{8}04)$ peaks of β-Ga_2O_3 apart from the substrate peaks. At low substrate temperature, the films exhibit degraded crystallinity since there is not sufficient energy for the adatoms to migrate on the surface as evidence by the reduction of XRD peak intensities. However, the thickness of the films remained constant in contrast to MBE growth where the films shows a decreased film thickness with decreasing substrate temperature. When the substrate temperature was increased above 500°C, the crystallinity of the film increased because of the increase surface energy increased present. On the other hand, with the higher oxygen pressure the peak intensity increased as the films are given more additional oxygen atoms leading to higher growth rate. From figure 3.15 (b) showing the rocking curves of β-Ga_2O_3 thin films with different oxygen pressures, it is clear that there is a minimum oxygen pressure for maintaining the crystal quality of the films. Moreover, during the gallium oxide formation in gas phase, the content of Ga in the films are preserved with the help of oxygen pressure. By interacting with the plume species, oxygen oxidize those species causing additional heat and energy that leads to a complete crystallization of the Ga_2O_3 thin films.

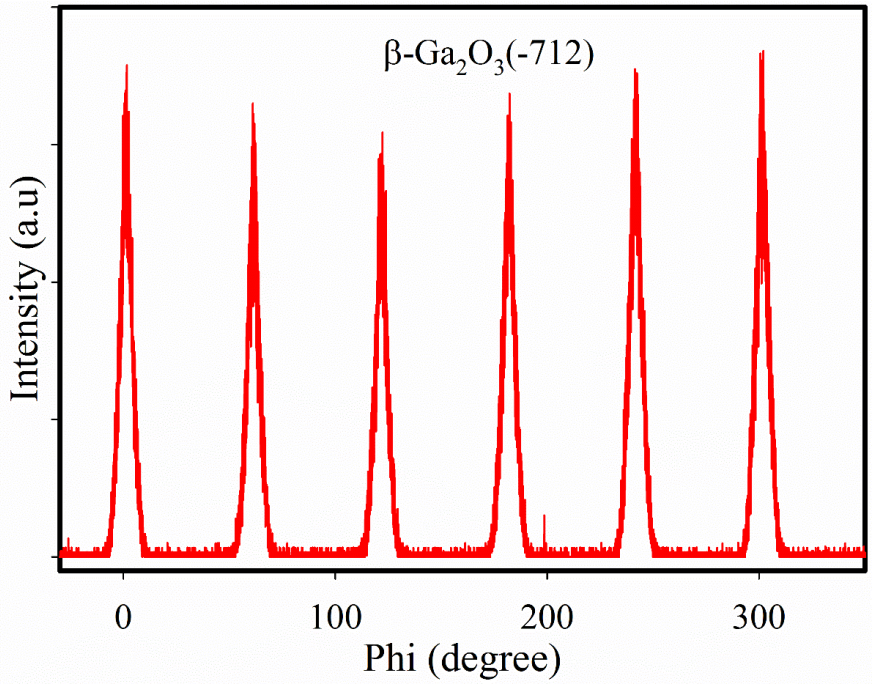

Figure3.16: XRD Φ-scan for {$\bar{7}$12}diffraction peak of β-Ga_2O_3 grown by PLD.

Figure 3.16 shows the in-plane phi (Φ) scan for β-Ga_2O_3 {$\bar{7}$12} diffraction plane grown at 700°C substrate temperature with oxygen pressure of 10^{-2} torr. Six peaks apart from each other by 60° for β-Ga_2O_3 {$\bar{7}$12} plane are present because of the hexagonal crystal system of sapphire. Originally, monoclinic β-Ga_2O_3 {$\bar{7}$12} plane has dipole in-plane rotational symmetry [49], [133]. However, sapphire (0001) has threefold rotational symmetry, so that, the rotational domains appeared in the grown films leading to sixfold rotational symmetry by growing epitaxially in three different directions same as the result found for MBE growth [49].

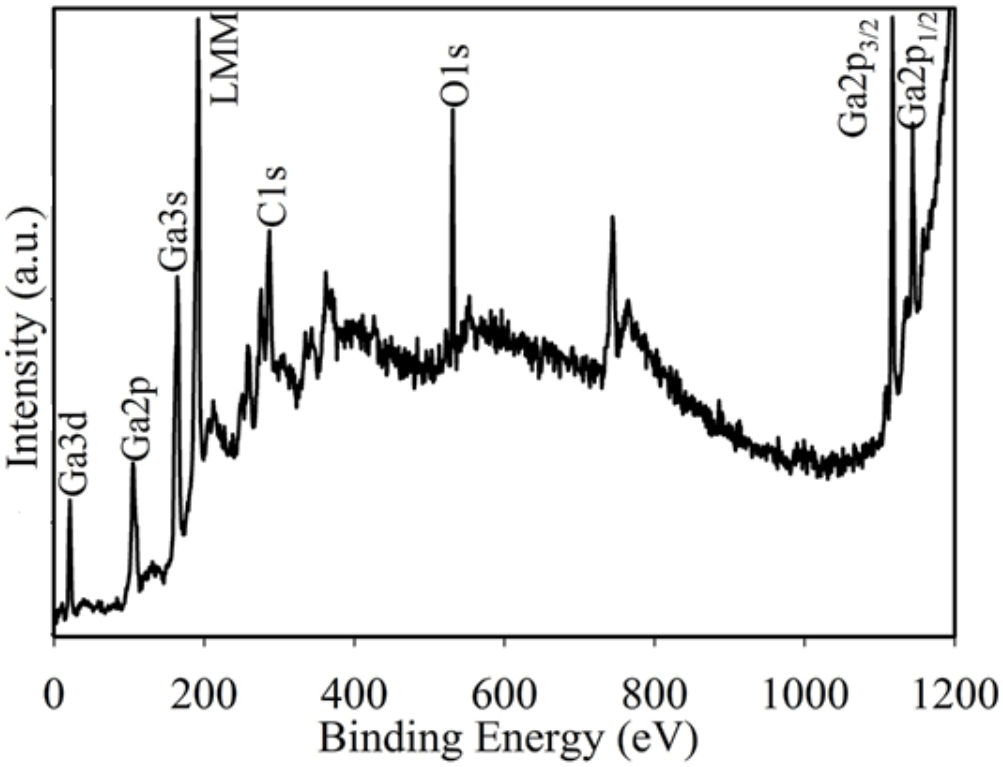

Figure 3.17: XPS survey scans β-Ga_2O_3 films grown by PLD.

Figure 3.17 shows the XPS survey scan of a typical PLD grown films which includes the oxygen peak and Ga related peaks along with carbon peak. The β-Ga_2O_3 films were grown at 800°C substrate temperature with oxygen partial pressure of 10^{-2} torr. The peak of C 1s is present since the sample was exposed to air during transferring sample from PLD growth chamber to XPS instrument which caused an accumulation of hydrocarbons. Ga 2p region was selected to determine the oxidation state of Ga (Fig. 3.18).

By means of Gaussian function on a Shirley background, XPS spectrum deconvolution was done as shown in figure 3.18 (a) and (b). The measured Ga 2p peak has been shown for the oxygen pressure of 10^{-3} and 10^{-1} torr. The Ga 2p peaks are the convolution of two peaks located at 1117.9 eV and 1116.75 eV corresponding to Ga_2O_3 and metallic Ga. These Ga core level peak exhibits shifting towards positive binding energy

indicating Ga^{3+} oxidation state. From the figure 3 (a) and (b), it is clear that the oxygen vacancies decrease with increasing oxygen pressure leading to an improvement in stoichiometric composition of Ga_2O_3 thin films [42], [106].

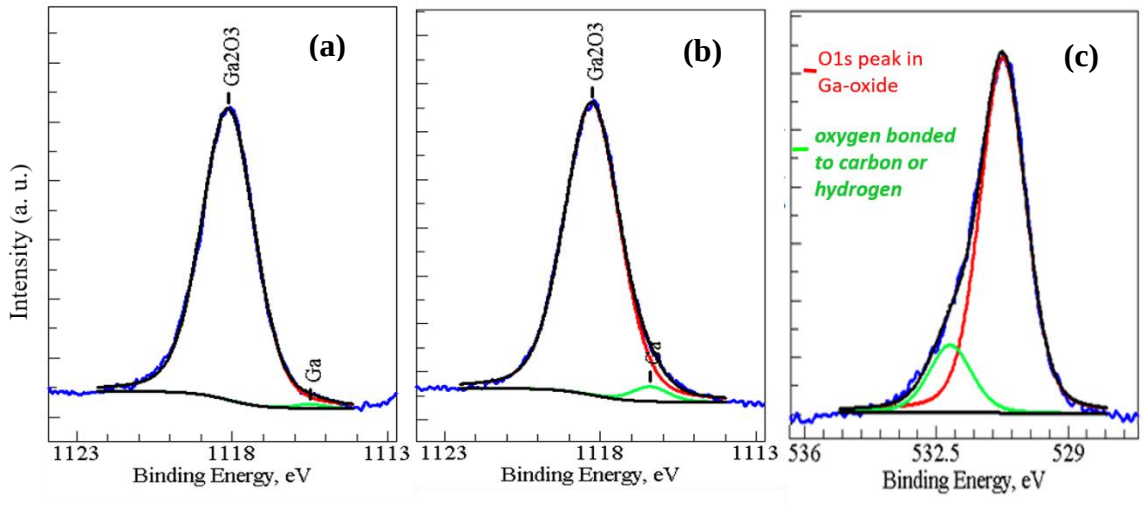

Figure 3.18: XPS of Ga 2p core level spectra of grown β-Ga_2O_3 thin films by PLD with different pressure (a) $P_{O_2} = 10^{-1}$ torr and (b) $P_{O_2} = 10^{-3}$ torr, (c) O1s core level apectrum. Experimental data is represented by blue lines.

Figure 3.18 (c) shows the O 1s peak which is a convolution of two peaks where one peak is from Ga_2O_3 represents bonding of Ga-O where Ga oxidation state is in highest position (Ga^{3+}) and another is from oxygen-carbon bond (carbonyl) or oxygen-hydrogen bond (hydroxyl) that adsorbed onto the surface as the samples were exposed to air before the measurements [42].

AFM measurements were carried out to understand the influence of substrate temperature and oxygen pressure on surface morphology and surface roughness of β-Ga_2O_3 thin films grown by PLD. Figure 3.19 (a-c) show the AFM images of the films for various oxygen pressure which were acquired at 1.5 Hz scanning frequency over 5×5 μm^2 scanning area. With lower oxygen pressure, the grain size becomes smaller leading to a decrease in

the surface roughness. However, oxygen pressure of 10^{-2} torr shows the highest surface roughness. The influence of the substrate temperature on morphology is shown in figure 3.20 (a-e). When substrate temperature is higher than 500°C, the surface roughness decreases with decreasing substrate temperature. Highest roughness value was obtained for the substrate temperature of 800°C as expected because it was found that films with higher thickness has higher surface roughness [134] when grown by PLD.

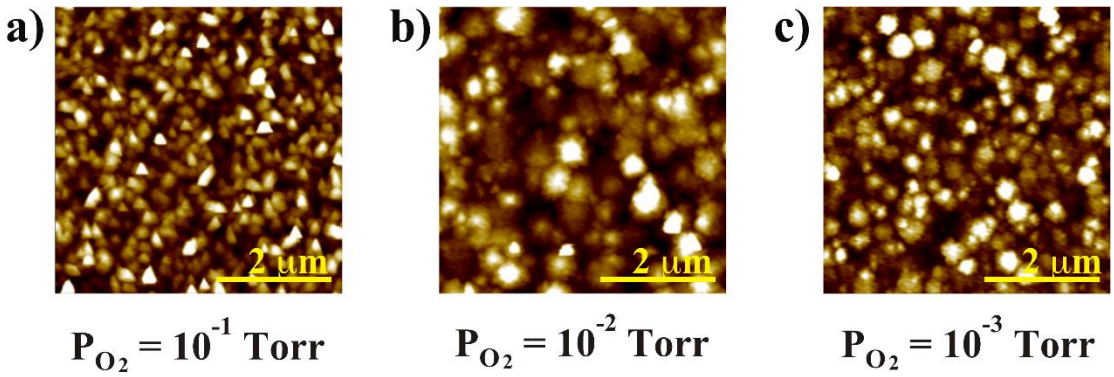

Figure 3.19: 5×5 μm^2 surface AFM images of β-Ga_2O_3 epitaxial films grown at various oxygen pressure by PLD.

Figures 3.19 and 3.20 show that the surface morphology and surface roughness of the films are strongly dependent on both the substrate temperatures and oxygen pressures [49], [130]. The surface morphology of the films changes with substrate temperature probably because of changing the energy or mobility of the adatoms. At lower substrate temperature, adatom migration length and diffusion on the surface of the substrate is small resulting in more 3D growth [135] and poor crystallinity which is in agreement with the XRD results (3.15 (a)). As the growth temperature increases, the adatoms have sufficient mobility or energy for the coalescence of the various nuclei giving a higher degree of crystallinity according to the XRD results.

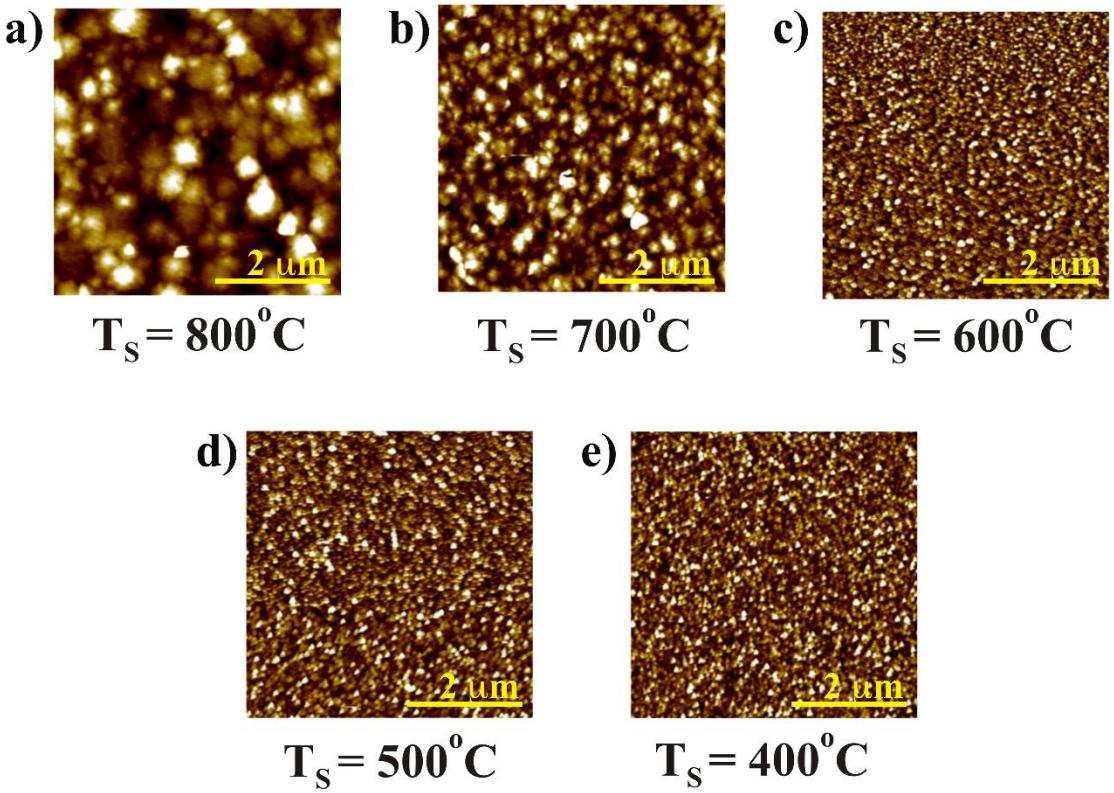

Figure 3.20: 5×5 μm^2 surface AFM images of β-Ga_2O_3 epitaxial films grown at various substrate temperatures by PLD.

In order to explore the optical properties, UV-Vis transmittance measurements of β-Ga_2O_3 thin films grown by PLD were carried out for different oxygen pressure from 10^{-3} to 10^{-1} torr for a substrate temperature of 800°C (figure 3.21) and various substrate temperatures from 400-800°C (figure 3.22 (a)) with an oxygen partial pressure of 10^{-2} torr. All the films presented in figure 3.21 and 3.22 (a) showed significant absorption with > 70% transmittance in the visible and UV region. When the oxygen partial pressure is 10^{-3} torr, there is more unoxidized Ga as shown in XPS measurements (figure 3.18 (b)) which results in changing the transparency compared to samples that have Ga that is completely oxidized (higher oxygen). It is not clear why the optical transparency decreases at higher growth temperatures but it may be related to the crystal quality with amorphous material

showing higher transparency. This is in contrast to Zhang *et al* [49] who found that the transparency increases with growth temperature.

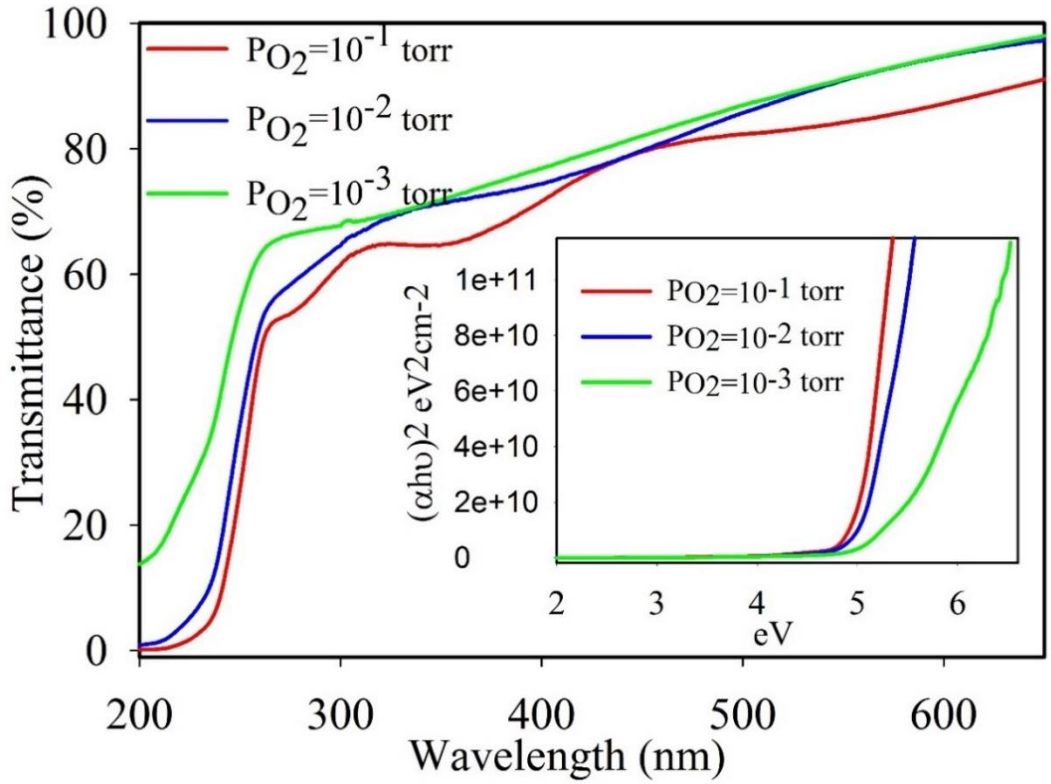

Figure 3.21: Transmittance spectra of β-Ga_2O_3 films grown with various oxygen pressure by PLD and inset is the bandgap of the corresponding films.

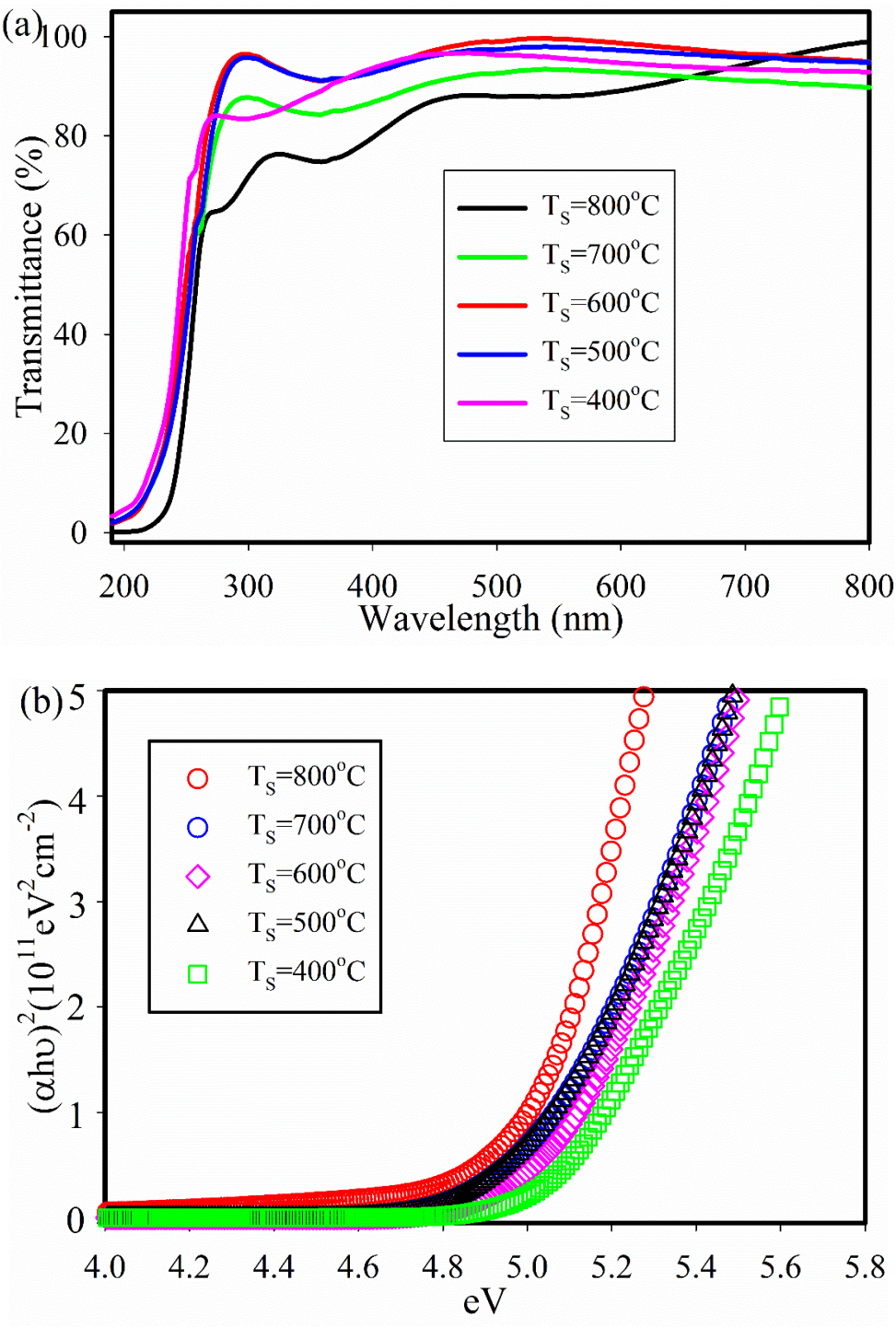

Figure 3.22: (a) Transmittance spectra of β-Ga_2O_3 films grown with various substrate temperature by PLD and (b) the bandgap of the corresponding films.

The bandgaps of the films (figure 3.21-inset and figure 3.22 (b)) were determined by using Tauc-plot analysis which has been described in the previous section of MBE growth. The bandgap of the films decreases as the oxygen pressure increases probably due to the increase stoichiometry of the films grown at higher oxygen with the bandgap obtained at high oxygen pressure is close to the value for bulk Ga_2O_3. The bandgap obtained for samples growth at higher substrate temperature are closely matched to the bandgap of bulk Ga_2O_3 material as shown in figure 3.22 (b). This may also be due to improved nucleation resulting in higher degree of crystallinity of the films. These results are in contrast to those obtained by Zhang et al. [49] who determined that the bandgaps were lower for samples grown at lower substrate temperatures. They suggest that the bandgap is lower for non-stoichiometric composition. The bandgaps of the grown films for various oxygen pressure and substrate temperature has been given in table V and VI. The bandgap found in this study compatible to other report published previously [27], [42], [48].

The measurements of complex index of refraction and thickness of the β-Ga_2O_3 films were carried out by using ellipsometric parameters Ψ and Δ for the wavelengths from 200-1000nm with the incident angles of 65-85° at room temperature. Cauchy transparent model was used to estimate the refractive index, film thickness and surface roughness by minimizing the Mean Squared Error (MSE). Details study on the fitting and modelling have been explained in previous section. The thickness of the films are decreases with decreasing the oxygen pressure which shows the consistancy with XRD results that growth rate and thickness depend on oxygen pressure. The refractive indexes obtained in this study nearly identical with different oxygen pressure and comparable to the value of other growth

methods discussed in this work. Table 5 and 6 show the optical properties of various oxygen pressure and susbtrate temperature.

Table 5: Optical properties of Ga_2O_3 thin films grown at various oxygen pressure by PLD.

Oxygen pressure (P_{O_2})	**Bandgap (eV)**	**Thickness (nm)**	**Refractive index (at wavelength of 6328 Å)**
10^{-1}torr	4.98	237.24	1.91
10^{-2}torr	5.0	170.11	1.91
10^{-3}torr	5.12	64.77	1.93

Table 6: Optical properties of Ga_2O_3 thin films grown at various substrate temperature by PLD.

Substrate temperature (°C)	**Bandgap (eV)**	**Thickness (nm)**	**Refractive index (at wavelength of 6328 Å)**
800	4.9	162.70	1.91
700	5.0	116.15	1.91
600	5.05	138.47	1.93
500	5.0	143.54	1.92
400	5.12	150.24	1.93

IV. GROWTH AND CHARACTERIZATION OF $(AlGa)_2O_3$ AND $(InGa)_2O_3$ ALLOYS

4.1 Introduction

Bandgap engineering is one of the important features for heterostructure electronic and optical device applications which is constructed by making alloys with two or more binary materials having different bandgaps. The achievement of β-Ga_2O_3 thin films and its alloys allow for bandgap engineering that can be used in device optimization and designing having great flexibility. The bandgap of β-Ga_2O_3 alloying with In_2O_3 and Al_2O_3 can be tuned from 3.5 to 8.6 eV which will enable a range of potential applications including wavelength-tunable optoelectronic devices, solid-state lighting and high electron mobility transistors (HEMTs) [73], [136]. Specifically, β-Ga_2O_3 based high power HEMTs are promising due to the large bandgap leading to an expectation of high electric breakdown voltage. It will also be possible to fabricate $Ga_2O_3/(In_xGa_{1-x})_2O_3/Ga_2O_3$ and $(Al_yGa_{1-y})_2O_3/Ga_2O_3/(Al_yGa_{1-y})_2O_3$ defect free heterostructures and quantum wells [73], [137]. The reason of using In and Al is that In, Ga, and Al belong to same column III element group and the chemical formula of their oxides form are stated as M_2O_3, where M=In, Ga, or Al, and have similar electronic structures [136], [138], [139]. However, the crystal structures of In_2O_3, β-Ga_2O_3 and Al_2O_3 are different and those being cubic bixbyite, monoclinic, or hexagonal respectively which will also that depend the conditions for their fabrication. Depending on the content of In and Al, phase separation is exhibited by both $(In_xGa_{1-x})_2O_3$ and $(Al_yGa_{1-y})_2O_3$ alloys [73]. The reported solubility limits of In_2O_3 and Al_2O_3 in β-Ga_2O_3 are x= 0.44 [67] and y= 0.78 [67] respectively in the powder state. Therefore, the quality of the crystal of $(In_xGa_{1-x})_2O_3$ and $(Al_yGa_{1-y})_2O_3$ alloy is expected to

be similar to other alloys such as AlInGaP, AlInGaAs, AlInGaSb, and AlInGaN [73] for certain values of x and y. In addition, $(InGa)_2O_3$ can be used as a transparent conducting oxide there is a reduction in the resistivity compared to undoped β-Ga_2O_3, while optical absorption coefficient will be very low in the visible range making suitable for the applications such as coatings on transparent substrates including plastic, fused silica, glass, and semiconductors [140], [141]. Various growth methods are utilized to grow $(InGa)_2O_3$ and $(AlGa)_2O_3$ thin films including plasma-assisted molecular beam epitaxy (PAMBE) [71], [73], [142], pulsed laser deposition (PLD) [136], [138], [143], metal organic chemical vapor deposition (MOCVD) [144] and sol-gel method [144]. Oshima *et al.* [71] reported the MBE growth of $(InGa)_2O_3$ thin films on sapphire substrate with an indium content of <0.35 but did not report any bandgap information. Fan *et al*. [144] have grown $(InGa)_2O_3$ thin films on sapphire substrate by MOCVD where they reported on the structural and photoluminescence properties of the films. On the other hand, Oshima *et al.* [73] reported on the plasma-assisted MBE growth of β-$(AlGa)_2O_3$ film on (100) β-Ga_2O_3 substrate where they have shown coherent growth which maintains the β phase for Al content of up to 0.61. Fabi *et al.* [138] have grown $(AlGa)_2O_3$ thin films on sapphire substrate by PLD and reported the structural properties and bandgap engineering. There are very few investigations on the development of the devices based on β-Ga_2O_3 with $(In_xGa_{1-x})_2O_3$ and $(Al_yGa_{1-y})_2O_3$ alloy.

PLD is a promising growth technology for high quality thin films including alloy compound thin films because it can transfer complete compositional consistency, that is stoichiometry, from the target to the deposited thin films. The atomic layer growth can be controlled by the simple adjustment of the laser power and repetition rate and the growth

can be monitored by *in-situ* reflection high energy electron diffraction (RHEED). Moreover, the growth at low substrate temperature is suitable with this technique because the adatoms surface mobility can be improved due to the high kinetic energies of source particles [136], [138].

4.2 Experimental

The growth of $(InGa)_2O_3$ and $(AlGa)_2O_3$ were carried out by PLD technique with the base pressure of $<5\times10^{-9}$ torr using a turbo pump. Single polished quarter of 2 in. c-plane sapphire substrate has been used which was cleaned ultrasonically with organic solvents (acetone and isopropanol alcohol) followed by rinsing in deionized water and blow dried with nitrogen gas before growth. The substrate temperature was 700°C with the fixed oxygen pressure of 2.5×10^{-2} torr. The targets were made from Ga_2O_3 (99.999%), Al_2O_3 (99.999%) and In_2O_3 (99.999%) powder with different In (mole ratio of In/(Ga+In): y=0.1, 0.6, 0.8, 1.0) and Al content (mole ratio of Al/(Ga+Al): y=0.1, 0.5, 0.75, 1.0) were used as source materials. A KrF excimer laser (λ = 248 nm) was utilized for laser ablation with the repetition rate of 10 Hz and the pulsed laser energy of 200 mJ for $(InGa)_2O_3$ and Ga_2O_3 thin films and 400 mJ for $(AlGa)_2O_3$ thin films respectively. After the growth, the films were annealed at 700°C temperature in vacuum without oxygen. The distance between the target and substrate was about 5 cm and during the deposition process, the substrate as well as the target were rotated to improve the film uniformity by reducing the crater formation on the target.

4.2 Results and Discussion

The two theta-omega (2θ-ω) XRD scan of $(InGa)_2O_3$ is shown in figure 4.1 (a) for various In (x) content in the films grown at a substrate temperature of 700°C on

sapphire substrate. Figure 4.1 (a) exhibits four different peaks other than peaks from (0001) sapphire substrate for the film with In content of x= 0.1. These diffraction peaks correspond to $(\bar{2}01)$, $(\bar{4}02)$, $(\bar{6}03)$and $(\bar{8}04)$ plane of β-Ga_2O_3. Any peak corresponds to In_2O_3 structure has not been detected in the XRD patterns indicating the film $(In_{0.1}Ga_{0.9})_2O_3$ exhibits the monoclinic structure of β-Ga_2O_3 which is in agreement with similar studies [136], [139], [144]. When the In content further increased to x= 0.6, diffraction peaks related to cubic $(InGa)_2O_3$ has been observed at 30° and 35° corresponding to In_2O_3 (222) and (400) with monoclinic structured $(\bar{2}01)$ plane oriented β-Ga_2O_3 which implies existence of mixed phases in the film. However, for higher In content (>0.6), only the peaks corresponding to (222) and (444) plane of In_2O_3 has been detected indicates the cubic structure of $(InGa)_2O_3$ thin films. Moreover, high resolution XRD patterns shown in figure 4.1 (b) and (c) for (444) plane of In_2O_3 cubic structure and $(\bar{6}03)$ plane of β-Ga_2O_3. From this figure, it is clearly observed that with increasing Ga content, the (444) peak shifts to higher angle and when In content increases, the $(\bar{6}03)$ peak shift towards lower angle [136], [139], [144]. The reason behind this is the higher ionic radius of In^{3+} (0.81 Å) compare to Ga^{3+} (0.62 Å) and as a result, when more In^{3+} ions into the lattice of Ga_2O_3 with the increase of In content, the lattice constant increases [140]. This is also the case for higher In content (x=0.8 and 1.0) suggesting the replacement of Ga^{3+} ions by In^{3+} ions in the lattice increases the lattice constant of $(In_xGa_{1-x})_2O_3$ with increasing the value of x in the film. In summary, it can be said that, the structure of $(InGa)_2O_3$ thin films changes from monoclinic to mixed phase and then to cubic phase with increasing In content in the film.

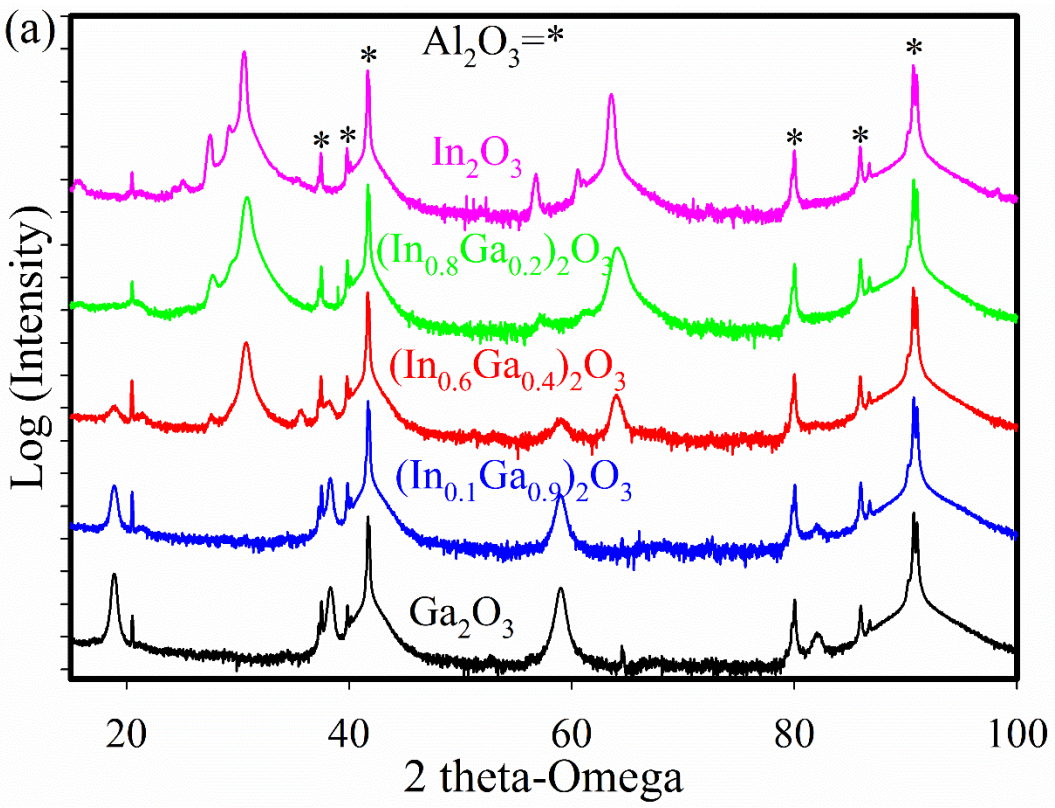
(a)
Al2O3=*
In2O3
(In0.8Ga0.2)2O3
(In0.6Ga0.4)2O3
(In0.1Ga0.9)2O3
Ga2O3
Log (Intensity)
20
40
60
80
100
2 theta-Omega

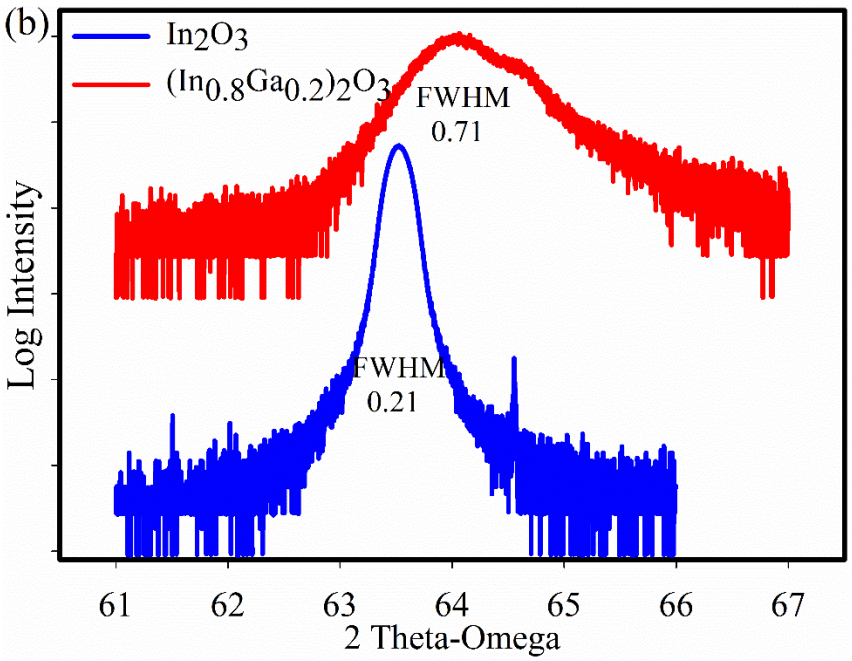
(b)
In2O3
(In0.8Ga0.2)2O3
FWHM
0.71
FWHM
0.21
Log Intensity
61
62
63
64
65
66
67
2 Theta-Omega

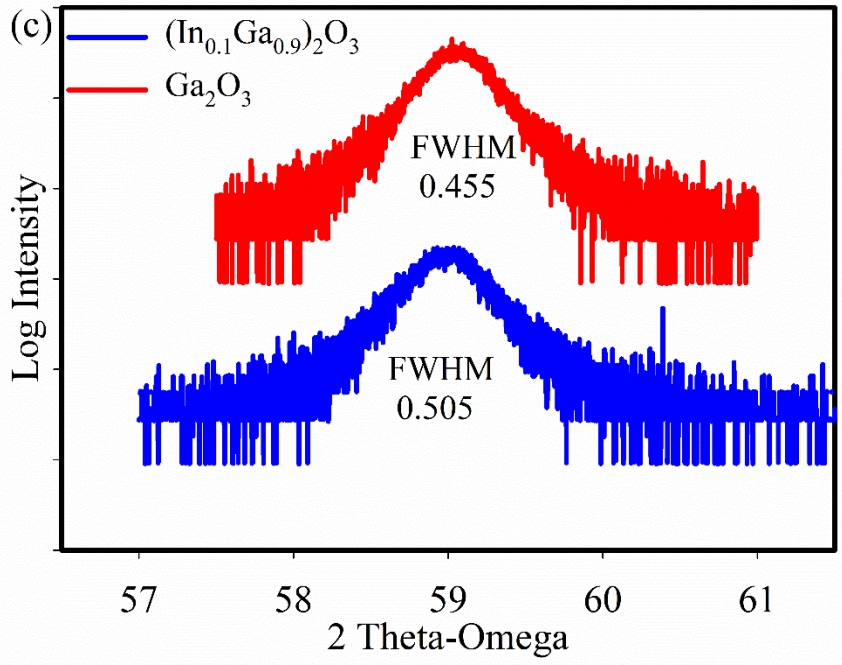

Figure 4.1: (a) (2θ-ω) XRD scan of $(InGa)_2O_3$, (b) rocking curve of In_2O_3 and $(In_{0.8}Ga_{0.2})_2O_3$, (c) rocking curve of In_2O_3 and $(In_{0.1}Ga_{0.9})_2O_3$.

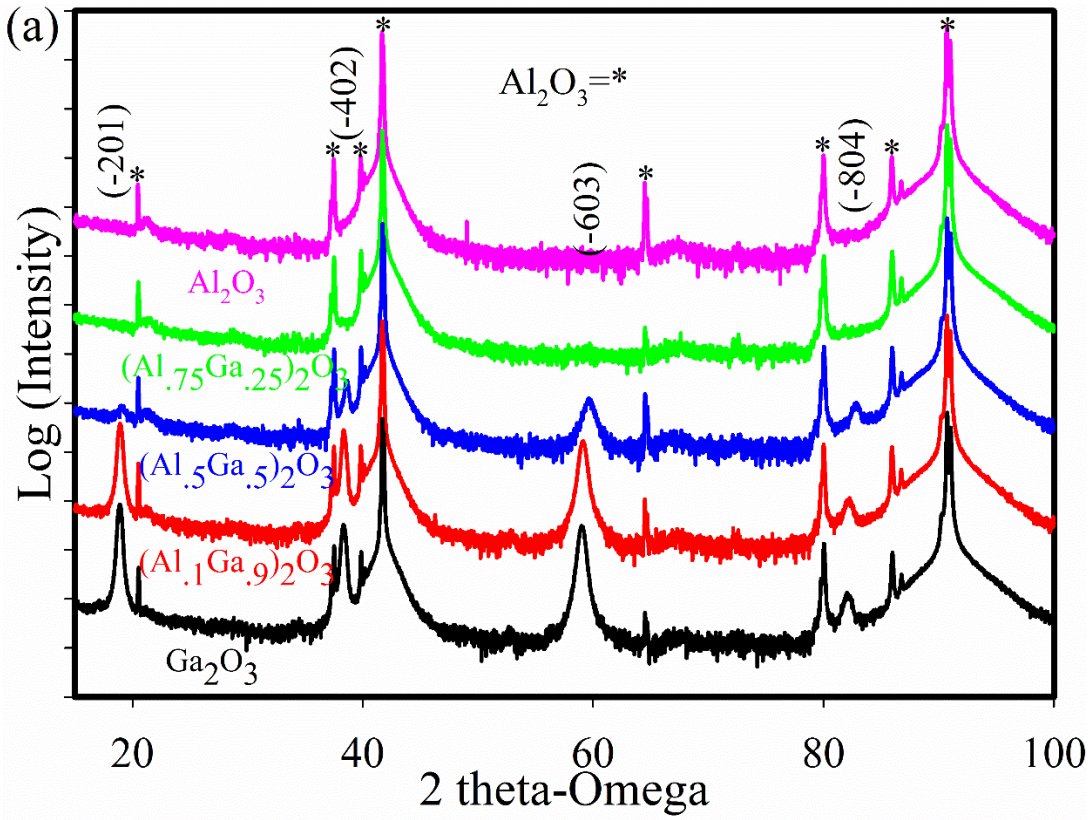

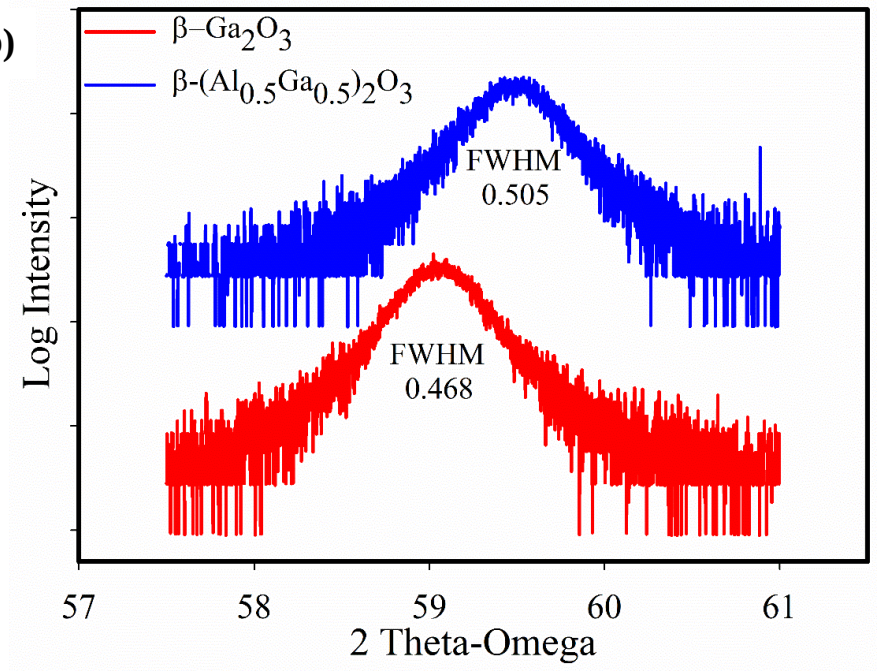

Figure 4.2: Figure 4.1: (a) (2θ-ω) XRD scan of $(AlGa)_2O_3$, (b) rocking curve of Ga_2O_3 and $(Al_{0.2}Ga_{0.8})_2O_3$.

Figure 4.2 (a) represents the XRD spectra of 2θ-ω scans for $(Al_yGa_{1-y})_2O_3$ thin films grown with various Al content (y). Four different peaks are observed corresponding to $(\bar{2}01)$, $(\bar{4}02)$, $(\bar{6}03)$and $(\bar{8}04)$ for y up to 0.50 represent the same monoclinic crystal structure as β-Ga_2O_3. For Al composition of 0.50 the peaks corresponding the monoclinic phase is reduced suggesting a mixed phase that includes corundum. When the Al content increases to 0.75, other than peaks from substrate no other peak has been observed indicates the collapse of the monoclinic crystal structure. This reduction of the monoclinic phase with higher Al content also been observed in other similar work [73], [74], [138]. With the increment of Al content in the grown film, the $(\bar{6}03)$ peak monotonically shifts to higher angle because of the smaller ionic radius of Al^{3+} compare to Ga^{3+} resulting in a smaller lattice constant. In addition, the high resolution XRD patterns (figure 4.2 (b)) of $(\bar{6}03)$ peak from the monoclinic structure show a shifting of the diffraction peaks towards higher

angle which confirms the inclusion of Al atoms into the Ga_2O_3 crystal lattice and the formation of ternary $(AlGa)_2O_3$ solid solution.

The transmittance spectra analysis was carried out to understand the effect of Al content in $(AlGa)_2O_3$ films on the optical properties. Figure 4.3 (a) shows the transmittance spectra of $(AlGa)_2O_3$ films with various Al content (y) in the films. All the samples exhibit transmittance in visible and UV region above 80%. The fundamental absorption of light causes a sharp edge of absorption in UV region for $(AlGa)_2O_3$ thin films which shifts to shorter wavelengths as the Al composition increases. When Al content (y) is higher than 75%, the absorption edge cannot be determined due to the instrument limitation.

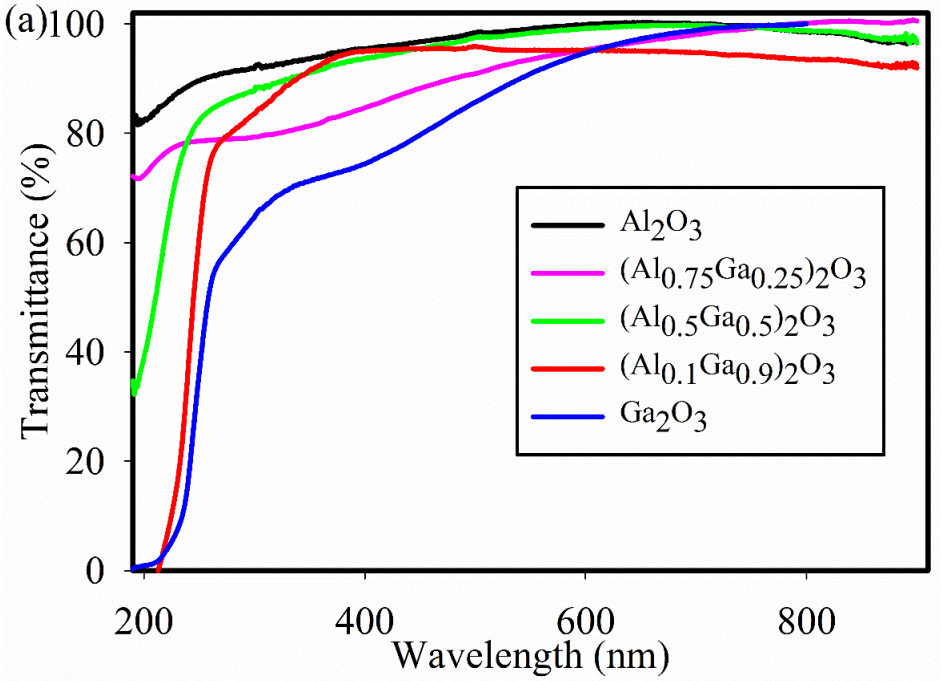

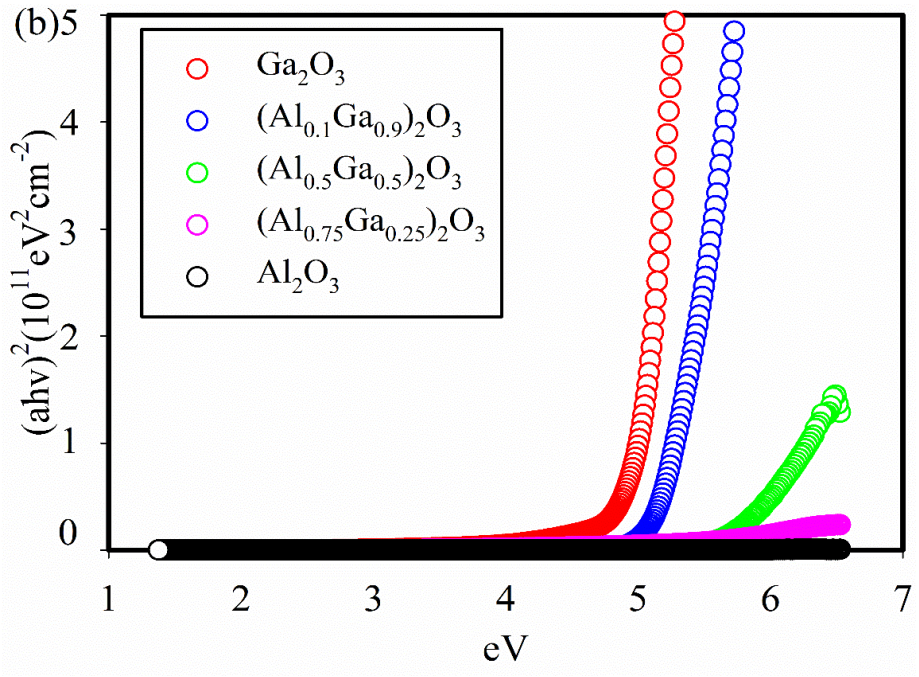

Figure 4.3: (a) Transmittance spectra for various Al content in $(AlGa)_2O_3$, (b) the bandgap of the corresponding films.

Similar to the procedure used to determine the bandgap of Ga_2O_3, the plot of $(\alpha h\nu)^2$ vs $h\nu$ as shown in figure 4.3 (b) is used to determine the bandgap of $(AlGa)_2O_3$ films by the extrapolation of the linear region of the plot to $h\nu = 0$ [10], [138], [143]. However, the bandgap of $(AlGa)_2O_3$ films could be determined only for the Al content of $y \leq 0.50$ because the transmittance spectra for other composition were incomplete. The bandgap of the grown $(AlGa)_2O_3$ thin films for Al content of 10% and 50% are 5.25 and 5.80 eV which are comparable the what has been measured by Zhang *et al.* [138].

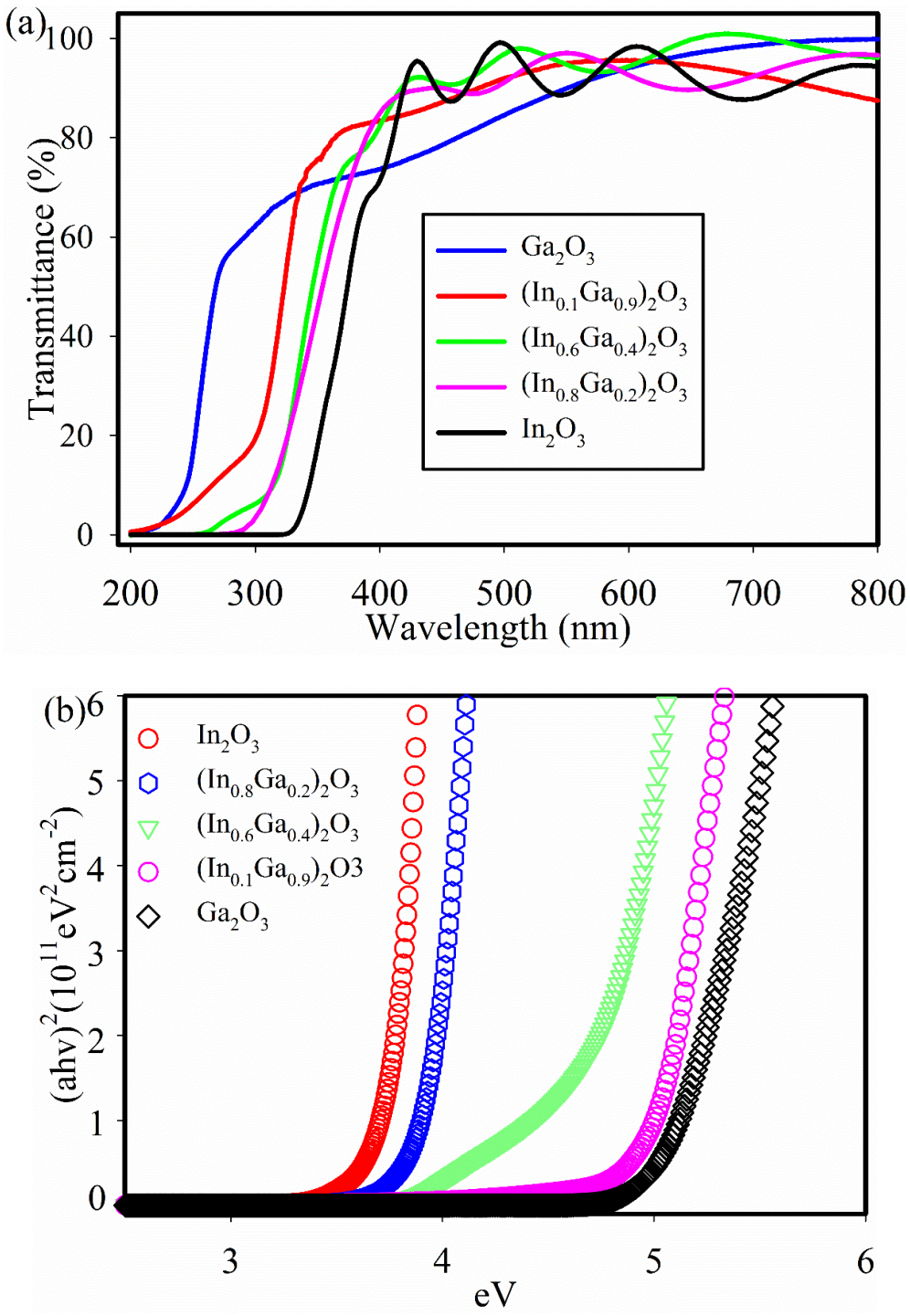

Figure 4.4: (a) Transmittance spectra for various In content in $(InGa)_2O_3$, (b) the bandgap of the corresponding films.

Figure 4.4 (a) shows the transmittance spectra for $(InGa)_2O_3$ films with different In content (x) in the films where it clearly exhibited the sharp absorption edges. In contrast to $(AlGa)_2O_3$ films, the absorption edge for $(InGa)_2O_3$ films shifts to longer λ with increasing In content (x) showing a decrease in the bandgap. The transmittance for $(InGa)_2O_3$ films is more than 80% in visible range. Figure 4.4 (b) shows a plot of $(\alpha h\nu)^2$ vs hν where it is noticed a sharp increase of absorption coefficient at the photon energy from 3.6-5.1 eV based on In content. At the high absorption region, these linear relationships suggesting a direct bandgap for the $(InGa)_2O_3$ thin films. As described, by the extrapolation of the linear portion of the plots to $h\nu = 0$, the bandgap of $(InGa)_2O_3$ thin films were determined for various In content. The obtained bandgap decrease linearly with increasing In content in the films [136], [144]–[147]. The results of $(AlGa)_2O_3$ and $(InGa)_2O_3$ indicates the bandgap of $(InAlGa)_2O_3$ thin films can be controlled by varying the Al and In content in the films leading to the flexibility in designing the opto-electronic and photonic devices based on $(InAlGa)_2O_3$ thin films in the short wavelength region.

V. DEVICE FABRICATION AND ELECTRICAL CHARACTERIZATION

5.1 Fabrication of a DUV Photodetector

To determine the electrical properties of the deposited thin films a metal-semiconductor-metal (MSM) Deep-Ultraviolet (DUV) photodetector was fabricated by depositing Au (100 nm)/Ti (50 nm) circular electrodes on the β-Ga_2O_3 thin film through a shadow mask by e-beam evaporation followed by 10 min thermal annealing at 450°C in an Ar atmosphere. The film was grown by MBE using gallium oxide compound source at 700°C. A low-pressure mercury (wavelength of 254 nm) UV lamp and a black light (wavelength of 405 nm) were used as the light sources at a fixed distance of ~5 cm away from the devices to evaluate UV photoresponse of the β-Ga_2O_3 thin films.

5.1.1 Electrical Characterization

The room temperature current-voltage (I-V) characteristics of the device is shown in figure 5.1 where it is clearly observed that with increasing bias voltage, current increases linearly under both dark and illuminated conditions suggesting Au/Ti forms a good ohmic contact. The possible reason behind this is the large surface states at the surface of Ga_2O_3 and hence, carriers can easily tunnel through the surface metal/oxide barrier [148]. The dark current was measured to be 4.25 nA at the bias voltage of 10 V with a large detector resistance of 1.4 GΩ. When the black light is used to illuminate the detector, the current increased to 56 nA which is not very significant compared to the dark current indicative of the non-sensitivity of β-Ga_2O_3 thin films to 405 nm wavelength light (figure 5.1(a)). Rather, this small current increment with black light is probably due to the phonon response of the light and sample interaction [128]. Conversely, the detector shows significant

increase of current of 5.6 μA at the bias voltage of 10 V when illuminated under UV lamp with 254nm wavelength with the photo-to-dark current ratio of the detector of >1000. This characteristic implies that under 254 nm light irradiation, the resistance of the β-Ga_2O_3 thin films based photodetector has decreased considerably.

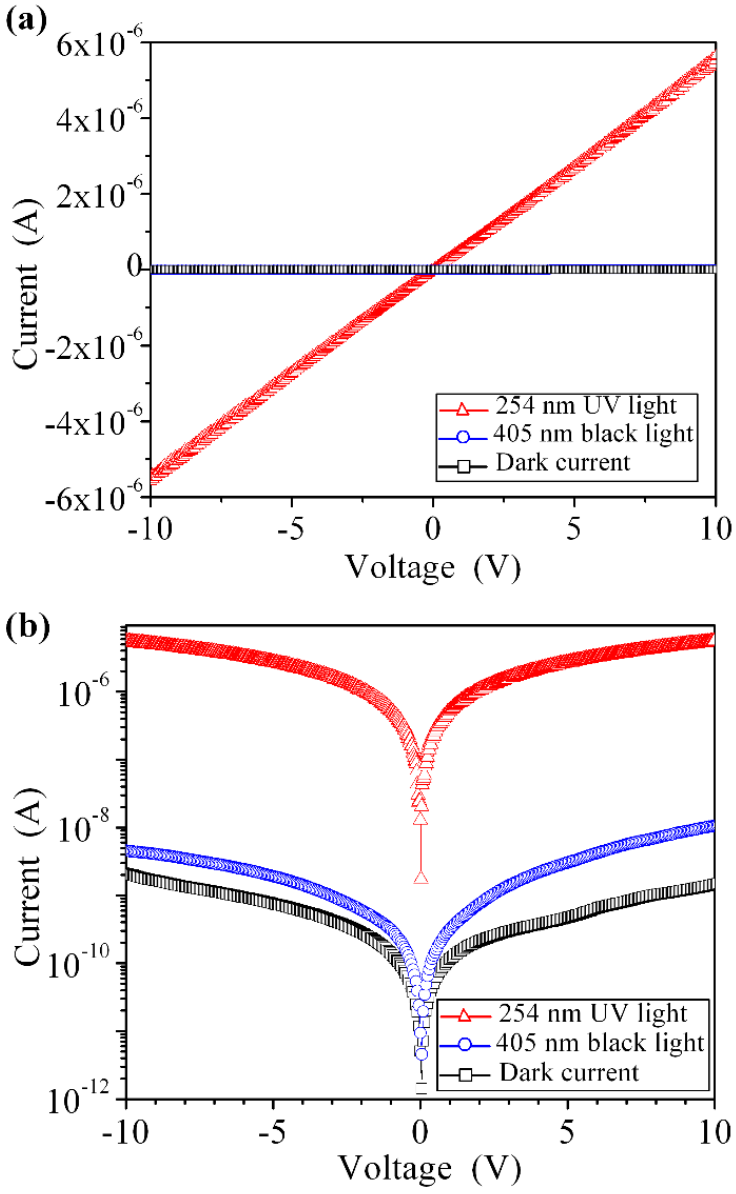

Figure 5.1: The I-V characteristics curve of the β-Ga_2O_3 based DUV photodetector in dark, under black light (wavelength of 405 nm), and under 254 nm light irradiation in room temperature where (a) and (b) plots represent the linear and logarithmic coordinate respectively.

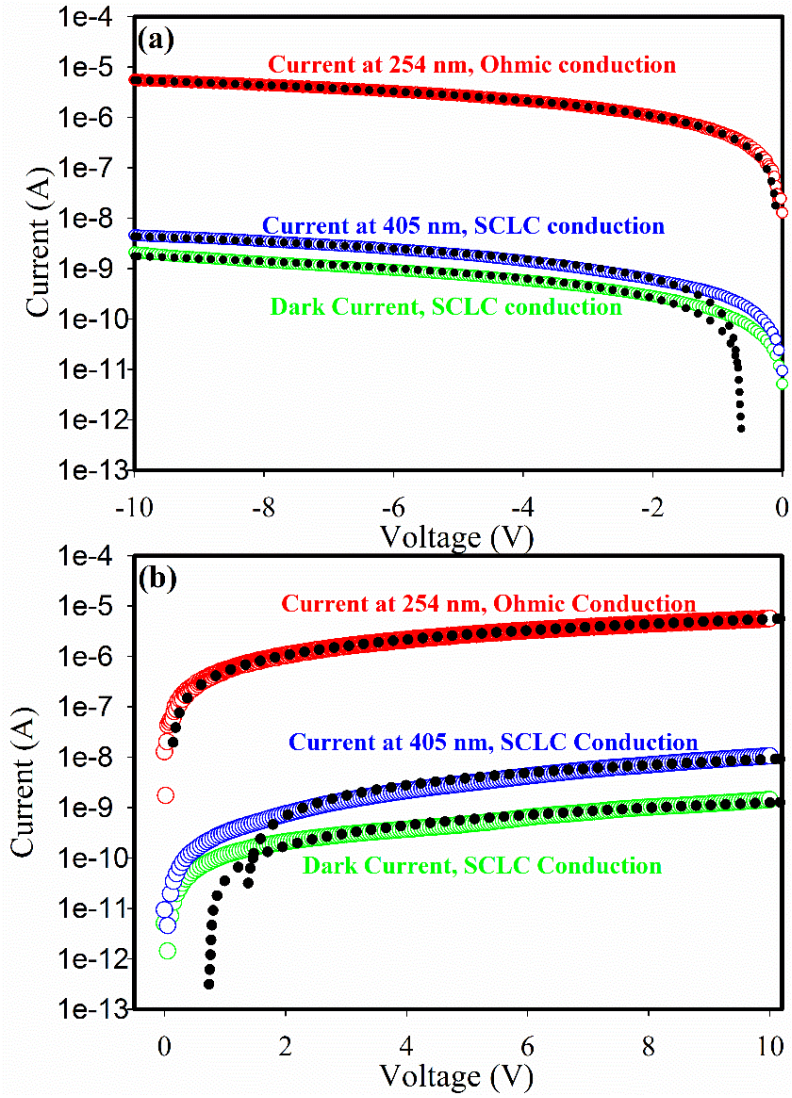

Figure 5.2: Carrier injection mechanism of β-Ga_2O_3 based DUV photodetector in dark, under black light (wavelength of 405 nm), and under 254 nm light irradiation in room temperature where (a) negative voltage sweep and (b) positive voltage sweep.

To examine the current conduction mechanism of MSM-DUV photodetectors, I-V characteristics were analyzed with popular carrier injection methods to find the best fit such as ohmic conduction ($I \alpha V$), thermionic emission ($\ln I \alpha V$), space charge limited conduction ($I \alpha V^a$, where $a \geq 2$), Poole-Frenkel emission [$\ln(I/V) \alpha V^{1/2}$] and Fowler-Nordheim tunneling [$I \alpha V^2 \exp(-E_a/V)$, where E_a is the kinetic energy of the charge

carriers] [149]–[152]. In this device, conduction mechanisms were determined by fitting the I-V curves for both the negative and positive voltage regions are depicted in figure 5.2 (a) and (b). For 405 nm illumination and dark current, space charge limited conduction (SCLC) mechanism is primarily responsible for current conduction between ±2 to ±10 V where most of the charge carriers are injected from the ohmic contact in a small voltage regions (0 to ±2 V) [151]. However, it was found that only ohmic current dominates during 254 nm UV illumination for the voltage range 0±10 V where most of the charge carriers are generated photoelectrons from β-Ga_2O_3 [151]. This phenomenon suggests that β-Ga_2O_3 thin films can be potential candidates for high performance UV photodetector applications.

To evaluate the performance of the detector, the time-dependent photoresponse of the photodetector under 254 nm light illumination was determined by applying light pulse at 1 V bias voltage and the results are shown in figure 5.3 (a). The photodetector exhibits good reproducibility and high robustness by showing almost identical response after numerous illumination cycles. The photocurrent increases rapidly to a stable value of ~ 7.5 nA and then abruptly decreases to a value of ~ 0.16 nA when the 254 nm illumination is turned on and off respectively. The approximate dark current (~ 0.16 nA) is low and favorable for practical detectors.

Detailed comparative and quantitative analysis of the response and recovery time to 254 nm illumination was investigated by fitting the photoresponse curve with a biexponential relaxation equation given by the following formula:

$$I = I_o + Ae^{-t/\tau_1} + Be^{-t/\tau_2}$$

Where I_o is the steady state photocurrent, t is the time, A and B are the constant, τ_1 and τ_2 are two relaxation time constants. Figure 5.3 (b) shows excellent fitting of the

photoresponse processes where τ_r is the time constants for the rising edge and τ_d is the time constants for the decay edge. Under 254 nm illumination the current rise and decay sharply with rise time constant, τ_r of 6s and the decay time constant, τ_d of 5s as shown in figure 9(b) which is comparable to other published results [27], [153]–[155].

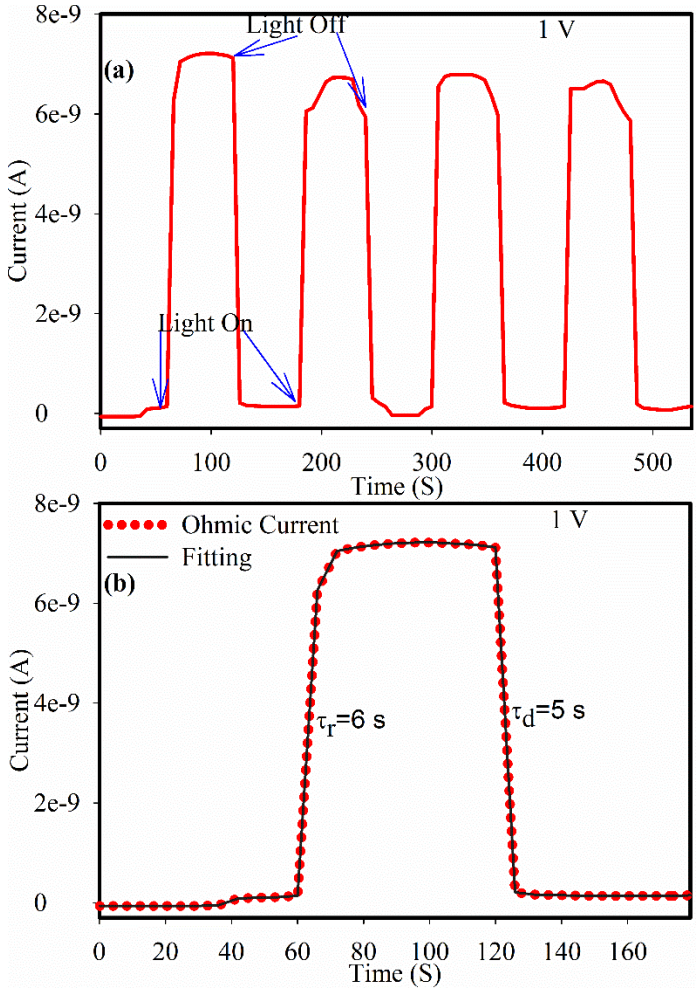

Figure 5.3: (a) Time-dependent photo response of the β-Ga_2O_3 thin films photodetector to 254 nm illumination. (b) Enlarged view of the rise/decay edges and the corresponding exponential fitting.

5.2 Electrical Properties of $(InGa)_2O_3$ Alloy

Electrical properties of $(InGa)_2O_3$ alloy has been determined by depositing Au (100 nm)/Ti (50 nm) circular electrodes on the $(In_{0.6}Ga_{0.4})_2O_3$ and $(In_{0.8}Ga_{0.2})_2O_3$ thin film,

grown by PLD, through a shadow mask using e-beam evaporation. After that, the samples were thermally annealed at 450°C for 2 min in the presence of Ar gas.

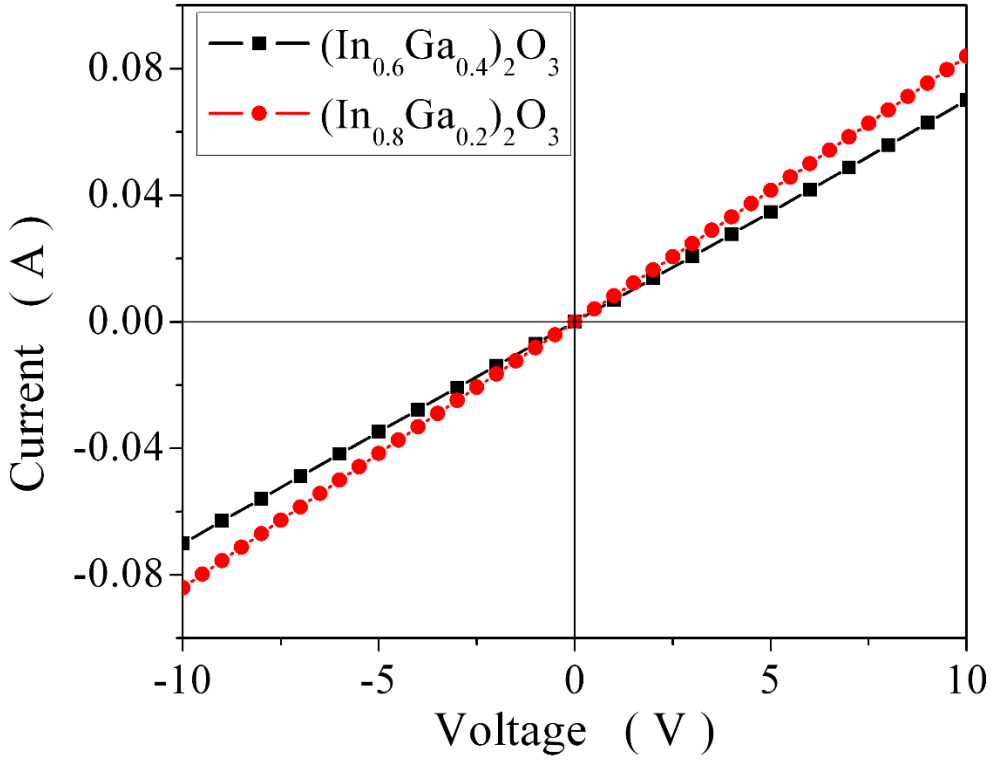

Figure 5.4: I-V characteristics for $(In_{0.6}Ga_{0.4})_2O_3$ and $(In_{0.8}Ga_{0.2})_2O_3$ thin film.

Figure 5.4 shows the I-V measurements for $(In_{0.6}Ga_{0.4})_2O_3$ and $(In_{0.8}Ga_{0.2})_2O_3$ thin film at room temperature where it is clearly observed that the current increases linearly with increasing voltage for both the films indicative of good ohmic contacts. The I-V curve shows that $(In_{0.8}Ga_{0.2})_2O_3$ exhibits obvious higher current with higher mobility (see later) than $(In_{0.6}Ga_{0.4})_2O_3$ films as increasing the In content in the film decreases the bandgap as shown in previous chapter. This reduced optical bandgap of the alloys is responsible for increasing the density of the surface state [156]. Moreover, the resistivity of In_2O_3 is very low because of shallow oxygen vacancies donors with the ionization energy ~0.08±0.02 eV [156]–[159]. The current measured for $(In_{0.6}Ga_{0.4})_2O_3$ film is 30 mA and for

$(In_{0.8}Ga_{0.2})_2O_3$ film is 70 mA at the bias voltage of 10 V respectively. When In content increases, the mobility also increases and the mobility for $(In_{0.6}Ga_{0.4})_2O_3$ and $(In_{0.8}Ga_{0.2})_2O_3$ film are 14.1 and 20 $cm^2V^{-1}s^{-1}$ respectively. It is worth to note that resistivity distribution strongly depends on the In content of the alloys. Electrical properties of the alloys are given in Table 7. More study is needed to optimize the electrical properties of $(InGa)_2O_3$ alloys with growth conditions.

Table 7: Electrical properties of $(InGa)_2O_3$

Alloy	**Mobility ($cm^2v^{-1}s^{-1}$)**	**Resistivity (Ω.cm)**	**Carrier concentration (cm^{-3})**
$(In_{0.6}Ga_{0.4})_2O_3$	14.1	1.243×10^{-3}	3.558×10^{20}
$(In_{0.8}Ga_{0.2})_2O_3$	20.5	1.24×10^{-3}	2.448×10^{20}

VI. CONCLUSION AND FUTURE WORK

6.1 Conclusion

In this research work, the growth and characterization of wide bandgap semiconductor β-Ga_2O_3 thin films and its alloys have been investigated. These represent potential candidates for a number of applications including high temperature sensors, luminescent phosphors, antireflection coatings, and UV optoelectronics and low loss and high-voltage switching devices such as high-breakdown Schottky diodes. Single crystal β-Ga_2O_3 thin films were grown on c-plane sapphire substrate using two different techniques including molecular beam epitaxy and pulsed laser deposition. Two different methods have been used when using MBE technique: one method used a compound Ga_2O_3 source with oxygen plasma while the second used elemental Ga source with oxygen plasma. For the elemental Ga source, lower growth rate was found for β-Ga_2O_3 thin films because of the formation and desorption of Ga_2O molecules. In order to solve that problem, a compound Ga_2O_3 source has been used which allowed for the deposition of the films with and without an additional oxygen source. Oxide growth has also been carried out by PLD technique to explore the influence of substrate temperature and oxygen pressure on the β-Ga_2O_3 thin films. The growth of two different alloys $(InGa)_2O_3$ and $(AlGa)_2O_3$ has been investigated to tune the bandgap of the oxide thin films from 3.5-8.6 eV for several applications such as wavelength-tunable optoelectronic devices, solid-state lighting and high electron mobility transistors (HEMTs). A metal-semiconductor-metal structured deep-ultraviolet photodetector based on β-Ga_2O_3 thin films has been demonstrated which exhibited high resistance as well as small dark current and was highly sensitive to UV light with wavelength of 254 nm. This points to β-Ga_2O_3 thin films as a potential candidate for deep-

ultraviolet photodetectors. The electrical properties of $(In_{0.6}Ga_{0.4})_2O_3$ and $(In_{0.8}Ga_{0.2})_2O_3$ alloys were measured it was found that mobility increases with increasing In content in the alloys.

6.2 Publications related to this research

1. Ghose, Susmita, Md Shafiqur Rahman, Juan Salvador Rojas-Ramirez, Manuel Caro, Ravi Droopad, Abraham Arias, and Nicola Nedev. *"Structural and optical properties of β-Ga_2O_3 thin films grown by plasma-assisted molecular beam epitaxy."* Journal of Vacuum Science & Technology B, Nanotechnology and Microelectronics: Materials, Processing, Measurement, and Phenomena 34, no. 2 (2016): 02L109.

2. Susmita Ghose, Md. Shafiqur Rahman, Liang Hong, Juan S. Rojas-Ramirez, Hanbyul Jin, Kibog Park, Robert Klie and Ravi Droopad, *"Growth and Characterization of β-Ga_2O_3 thin film by Molecular Beam Epitaxy for Deep-UV photodetector",* (Submitted).

3. Susmita Ghose, M. S. Rahman, Khem Barel, J. S. Rojas-Ramirez, R. Droopad, *"Structural, optical and electrical properties of $(InGa)_2O_3$ and $(AlGa)_2O_3$ alloys grown by pulsed laser deposition",* (Manuscript in preparation).

4. Rahman, Md Shafiqur, **Susmita Ghose**, Liang Hong, Juan S. Rojas-Ramirez, R. Droopad, *"$BiFeO_3/La_{0.7}Sr_{0.3}MnO_3$ superlattice hetero-structures for enhanced interface induced properties"*, (Manuscript in preparation).

5. Rahman, Md Shafiqur, **Susmita Ghose**, Liang Hong, Pradip Dhungana, Abbas Fahami, Javad R. Gatabi, Juan S. Rojas-Ramirez et al. *"Integration of $BiFeO_3/La_{0.7}Sr_{0.3}$ MnO_3 heterostructures with III–V semiconductors for low-power non-volatile memory and multiferroic field effect transistors."* Journal of Materials Chemistry C 4, no. 43 (2016): 10386-10394.

6. Rahman, Md Shafiqur, **Susmita Ghose**, Javad R. Gatabi, Juan S. Rojas-Ramirez, R. K. Pandey, and Ravi Droopad. *"Heteroepitaxial growth and characterization of $BiFeO_3$ thin films on GaAs."* Materials Research Express 3, no. 10 (2016): 106408.

6.3 Future Work

- **Study and analysis for the doping of β-Ga_2O_3:**

β-Ga_2O_3 can be doped with Si or Sn to investigate the electrical properties of β-Ga_2O_3 in order to make a metal oxide semiconductor FET. However, there is a need for the development of a suitable p-type dopant.

- **Integration with GaN and β-Ga_2O_3 films by MBE:**

For epitaxial growth of GaN as well as related III-nitrides, β-Ga_2O_3 is a promising candidate as a substrate because of lower lattice mismatch between β-Ga_2O_3 and GaN. For future research, high-quality GaN epilayer can be deposited on monoclinic β-Ga_2O_3 by molecular beam epitaxy (MBE) to investigate and verify further the efficiency of using β-Ga_2O_3 as a substrate of GaN and the heterointegration of these 2 material systems.

- **Ga_2O_3 Homoepitaxial films grown on β-Ga_2O_3 ($\bar{2}01$) substrate:**

Homoepitaxial β-Ga_2O_3 thin film growth on β-Ga_2O_3 ($\bar{2}01$) substrate and the dependency of ($\bar{2}01$) β-Ga_2O_3 growth rates and surface structure on growth condition can be explored. Besides that, a comparison on the optical and electrical properties between homoepitaxial and heteroepitaxial growth by MBE and PLD should be investigated.

REFERENCES

[1] T. C. Lovejoy, *III-VI semiconductors and oxides: Electronic structure, surface morphology, and transition metal doping of gallium selenide, indium selenide, and gallium oxide*. 2010.

[2] D.-S. Tsai, C.-A. Lin, W.-C. Lien, H.-C. Chang, Y.-L. Wang, and J.-H. He, "Ultra-high-responsivity broadband detection of Si metal–semiconductor–metal schottky photodetectors improved by ZnO nanorod arrays," *ACS Nano*, vol. 5, no. 10, pp. 7748–7753, 2011.

[3] D. Walker and M. Razeghi, "The development of nitride-based UV photodetectors," *Optoelectron. Rev.*, vol. 8, no. 1, pp. 25–42, 2000.

[4] T.-C. Wei, D.-S. Tsai, P. Ravadgar, J.-J. Ke, M.-L. Tsai, D.-H. Lien, C.-Y. Huang, R.-H. Horng, and J.-H. He, "See-Through $\ hbox {Ga} _ {2}\ hbox {O} _ {3} $ Solar-Blind Photodetectors for Use in Harsh Environments," *IEEE J. Sel. Top. Quantum Electron.*, vol. 20, no. 6, pp. 112–117, 2014.

[5] E. Monroy, F. Omnès, and F. Calle, "Wide-bandgap semiconductor ultraviolet photodetectors," *Semicond. Sci. Technol.*, vol. 18, no. 4, p. R33, 2003.

[6] G. L. Harris, *Properties of silicon carbide*, no. 13. Iet, 1995.

[7] M. Henini, "Properties, Processing and Applications of Gallium Nitride and Related Semiconductors: JH Edgar, S. Strite, I. Akasaki, H. Amano, C. Wetzel (Eds.); INSPEC, The Institution of Electrical Engineers, ISBN 0-85296-818-3." Elsevier, 2000.

[8] M. H. Gowda, "Optical Characterization of Wide-band gap Bulk crystals and Epitaxial layers," 2008.

[9] M. Higashiwaki, K. Sasaki, A. Kuramata, T. Masui, and S. Yamakoshi, "Development of gallium oxide power devices," *Phys. status solidi*, vol. 211, no. 1, pp. 21–26, 2014.

[10] S. Ghose, M. S. Rahman, J. S. Rojas-Ramirez, M. Caro, R. Droopad, A. Arias, and N. Nedev, "Structural and optical properties of β-Ga2O3 thin films grown by plasma-assisted molecular beam epitaxy," *J. Vac. Sci. Technol. B, Nanotechnol. Microelectron. Mater. Process. Meas. Phenom.*, vol. 34, no. 2, p. 02L109, 2016.

[11] A. Walsh, A. B. Kehoe, D. J. Temple, G. W. Watson, and D. O. Scanlon, "PbO2: from semi-metal to transparent conducting oxide by defect chemistry control.," *Chem. Commun. (Camb).*, vol. 49, no. 5, pp. 448–50, 2013.

[12] A. Walsh, J. L. F. Da Silva, and S.-H. Wei, "Origins of band-gap renormalization in degenerately doped semiconductors," *Phys. Rev. B*, vol. 78, no. 7, p. 75211, 2008.

[13] N. F. Mott, "Metal-insulator transition," *Rev. Mod. Phys.*, vol. 40, no. 4, p. 677, 1968.

[14] S. Calnan, "Applications of oxide coatings in photovoltaic devices," *Coatings*, vol. 4, no. 1, pp. 162–202, 2014.

[15] M. Grundmann, A. Rahm, and H. von Wenckstern, "Transparent Conductive Oxides," *Phys. Status Solidi A*, vol. 212, no. 7, p. 1408, 2015.

[16] M. Higashiwaki, K. Sasaki, A. Kuramata, T. Masui, and S. Yamakoshi, "Gallium oxide (Ga2O3) metal-semiconductor field-effect transistors on single-crystal β-Ga2O3 (010) substrates," *Appl. Phys. Lett.*, vol. 100, no. 1, p. 13504, 2012.

[17] T. Oishi, Y. Koga, K. Harada, and M. Kasu, “High-mobility β-Ga2O3 () single crystals grown by edge-defined film-fed growth method and their Schottky barrier diodes with Ni contact,” *Appl. Phys. Express*, vol. 8, no. 3, p. 31101, 2015.
[18] D. Splith, S. Müller, F. Schmidt, H. Von Wenckstern, J. J. van Rensburg, W. E. Meyer, and M. Grundmann, “Determination of the mean and the homogeneous barrier height of Cu Schottky contacts on heteroepitaxial β-Ga2O3 thin films grown by pulsed laser deposition,” *Phys. status solidi*, vol. 211, no. 1, pp. 40–47, 2014.
[19] K. Sasaki, M. Higashiwaki, A. Kuramata, T. Masui, and S. Yamakoshi, “$\ hbox {Ga} _ {2}\ hbox {O} _ {3} $ Schottky Barrier Diodes Fabricated by Using Single-Crystal $\ beta $–$\ hbox {Ga} _ {2}\ hbox {O} _ {3} $(010) Substrates,” *IEEE electron device Lett.*, vol. 34, no. 4, pp. 493–495, 2013.
[20] H. Aida, K. Nishiguchi, H. Takeda, N. Aota, K. Sunakawa, and Y. Yaguchi, “Growth of β-Ga2O3 single crystals by the edge-defined, film fed growth method,” *Jpn. J. Appl. Phys.*, vol. 47, no. 11R, p. 8506, 2008.
[21] E. G. Víllora, K. Shimamura, Y. Yoshikawa, K. Aoki, and N. Ichinose, “Large-size β-Ga 2 O 3 single crystals and wafers,” *J. Cryst. Growth*, vol. 270, no. 3, pp. 420–426, 2004.
[22] M. Higashiwaki, K. Sasaki, H. Murakami, Y. Kumagai, A. Koukitu, A. Kuramata, T. Masui, and S. Yamakoshi, “Recent progress in Ga2O3 power devices,” *Semicond. Sci. Technol.*, vol. 31, no. 3, p. 34001, 2016.
[23] K. Sasaki, M. Higashiwaki, A. Kuramata, T. Masui, and S. Yamakoshi, “MBE grown Ga2O3 and its power device applications,” *J. Cryst. Growth*, vol. 378, pp. 591–595, 2013.
[24] P. Marie, X. Portier, and J. Cardin, “Growth and characterization of gallium oxide thin films by radiofrequency magnetron sputtering,” *Phys. status solidi*, vol. 205, no. 8, pp. 1943–1946, 2008.
[25] Y. An, X. Chu, Y. Huang, Y. Zhi, D. Guo, P. Li, Z. Wu, and W. Tang, “Au plasmon enhanced high performance β-Ga 2 O 3 solar-blind photo-detector,” *Prog. Nat. Sci. Mater. Int.*, vol. 26, no. 1, pp. 65–68, 2016.
[26] H. Hosono, “Recent progress in transparent oxide semiconductors: Materials and device application,” *Thin Solid Films*, vol. 515, no. 15, pp. 6000–6014, 2007.
[27] D. Guo, Z. Wu, P. Li, Y. An, H. Liu, X. Guo, H. Yan, G. Wang, C. Sun, and L. Li, “Fabrication of β-Ga 2 O 3 thin films and solar-blind photodetectors by laser MBE technology,” *Opt. Mater. Express*, vol. 4, no. 5, pp. 1067–1076, 2014.
[28] M. Zhong, Z. Wei, X. Meng, F. Wu, and J. Li, “High-performance single crystalline UV photodetectors of β-Ga 2 O 3,” *J. Alloys Compd.*, vol. 619, pp. 572–575, 2015.
[29] R. Kumaran, T. Tiedje, S. E. Webster, S. Penson, and W. Li, “Epitaxial Nd-doped α-(Al 1− x Ga x) 2 O 3 films on sapphire for solid-state waveguide lasers,” *Opt. Lett.*, vol. 35, no. 22, pp. 3793–3795, 2010.
[30] T. Oshima, T. Nakazono, A. Mukai, and A. Ohtomo, “Epitaxial growth of γ-Ga 2 O 3 films by mist chemical vapor deposition,” *J. Cryst. Growth*, vol. 359, pp. 60–63, 2012.

[31] S. I. Stepanov, V. I. Nikolaev, V. E. Bougrov, and A. E. Romanov, “GALLIUM OXIDE: PROPERTIES AND APPLICA A REVIEW,” *Rev. Adv. Mater. Sci*, vol. 44, pp. 63–86, 2016.
[32] S. Geller, “Crystal Structure of β-Ga2O3,” *J. Chem. Phys.*, vol. 33, no. 3, pp. 676–684, 1960.
[33] J. A. Kohn, G. Katz, and J. D. Broder, “Characterization of β-Ga 2 O 3 and its Alumina Isomorph, θ-Al 2 O 3,” *Am. Miner.*, vol. 42, pp. 398–407, 1957.
[34] G. M. Wolten and A. B. Chase, “Determination of the point group of β-Ga2O3 from morphology and physical properties,” *J. Solid State Chem.*, vol. 16, no. 3–4, pp. 377–383, Jan. 1976.
[35] J. Åhman, G. Svensson, and J. Albertsson, “A reinvestigation of β-gallium oxide,” *Acta Crystallogr. Sect. C Cryst. Struct. Commun.*, vol. 52, no. 6, pp. 1336–1338, 1996.
[36] T. Onuma, S. Fujioka, T. Yamaguchi, M. Higashiwaki, K. Sasaki, T. Masui, and T. Honda, “Correlation between blue luminescence intensity and resistivity in β-Ga2O3 single crystals,” *Appl. Phys. Lett.*, vol. 103, no. 4, p. 41910, 2013.
[37] N. Ueda, H. Hosono, R. Waseda, and H. Kawazoe, “Synthesis and control of conductivity of ultraviolet transmitting beta-Ga2O3 single crystals,” *Appl. Phys. Lett.*, vol. 70, pp. 3561–3563, 1997.
[38] J. B. Varley, J. R. Weber, A. Janotti, and C. G. Van de Walle, “Oxygen vacancies and donor impurities in ß-Ga 2 O 3,” *Appl. Phys. Lett.*, vol. 97, p. 142106, 2010.
[39] J. B. Varley, A. Janotti, C. Franchini, and C. G. Van de Walle, “Role of self-trapping in luminescence and p-type conductivity of wide-band-gap oxides,” *Phys. Rev. B*, vol. 85, no. 8, p. 81109, 2012.
[40] K. Sasaki, A. Kuramata, T. Masui, E. G. Víllora, K. Shimamura, S. Yamakoshi, and E. G. Villora, “Device-Quality b-Ga2O2 Epitaxial Films Fabricated by Ozone Molecular Beam Epitaxy,” *Appl. Phys. Express*, vol. 5, no. 3, p. 35502, 2012.
[41] R. K. Ramachandran, J. Dendooven, J. Botterman, S. P. Sree, D. Poelman, J. A. Martens, H. Poelman, and C. Detavernier, “Plasma enhanced atomic layer deposition of Ga2O3 thin films,” *J. Mater. Chem. A*, vol. 2, no. 45, pp. 19232–19238, 2014.
[42] C. V Ramana, E. J. Rubio, C. D. Barraza, A. Miranda Gallardo, S. McPeak, S. Kotru, and J. T. Grant, “Chemical bonding, optical constants, and electrical resistivity of sputter-deposited gallium oxide thin films,” *J. Appl. Phys.*, vol. 115, no. 4, p. 43508, 2014.
[43] D. H. Kim, S. H. Yoo, K. S. An, H. S. Yoo, and Y. Kim, “Chemical Vapor Deposition of Ga~ 2O~ 3 Thin Films on Si Substrates,” *Bull. Chem. Soc.*, vol. 23, no. 2, pp. 225–228, 2002.
[44] D.-S. Wuu, S.-L. Ou, R.-H. Horng, P. Ravadgar, T.-Y. Wang, and H.-Y. Lee, “Growth and characterization of Ga 2 O 3 on sapphire substrates for UV sensor applications,” in *SPIE OPTO*, 2012, p. 826317.
[45] S. L. Ou, D. S. Wuu, Y. C. Fu, S. P. Liu, R. H. Horng, L. Liu, and Z. C. Feng, “Growth and etching characteristics of gallium oxide thin films by pulsed laser deposition,” *Mater. Chem. Phys.*, vol. 133, no. 2–3, pp. 700–705, 2012.

[46] E. G. Víllora, K. Shimamura, K. Kitamura, and K. Aoki, “Rf-plasma-assisted molecular-beam epitaxy of β-Ga 2 O 3,” *Appl. Phys. Lett.*, vol. 88, no. 3, p. 31105, 2006.
[47] M.-Y. Tsai, O. Bierwagen, M. E. White, and J. S. Speck, “β-Ga 2 O 3 growth by plasma-assisted molecular beam epitaxy a,” *J. Vac. Sci. Technol. A Vacuum, Surfaces, Film.*, vol. 28, no. 2, pp. 354–359, 2010.
[48] F.-P. Yu, S.-L. Ou, and D.-S. Wuu, “Pulsed laser deposition of gallium oxide films for high performance solar-blind photodetectors,” *Opt. Mater. Express*, vol. 5, no. 5, pp. 1240–1249, 2015.
[49] F. B. Zhang, K. Saito, T. Tanaka, M. Nishio, and Q. X. Guo, “Structural and optical properties of Ga2O3 films on sapphire substrates by pulsed laser deposition,” *J. Cryst. Growth*, vol. 387, pp. 96–100, 2014.
[50] S.-A. Lee, J.-Y. Hwang, J.-P. Kim, S.-Y. Jeong, and C.-R. Cho, “Dielectric characterization of transparent epitaxial Ga 2 O 3 thin film on n-Ga N⁄ Al 2 O 3 prepared by pulsed laser deposition,” *Appl. Phys. Lett.*, vol. 89, no. 18, p. 182906, 2006.
[51] G. V Chaplygin and S. A. Semiletov, “Preparation, structure and electrical properties of epitaxial films of Ga2O3 on sapphire substrates,” *Thin Solid Films*, vol. 32, no. 2, pp. 321–324, 1976.
[52] H. Ohta, M. Orita, M. Hirano, K. Ueda, and H. Hosono, “Epitaxial growth of transparent conductive oxides,” *Int. J. Mod. Phys. B*, vol. 16, no. 01n02, pp. 173–180, 2002.
[53] S. Nakagomi and Y. Kokubun, “Crystal orientation of β-Ga 2 O 3 thin films formed on c-plane and a-plane sapphire substrate,” *J. Cryst. Growth*, vol. 349, no. 1, pp. 12–18, 2012.
[54] P. Ravadgar, R.-H. Horng, S.-D. Yao, H.-Y. Lee, B.-R. Wu, S.-L. Ou, and L.-W. Tu, “Effects of crystallinity and point defects on optoelectronic applications of β-Ga 2 O 3 epilayers,” *Opt. Express*, vol. 21, no. 21, pp. 24599–24610, 2013.
[55] V. Gottschalch, K. Mergenthaler, G. Wagner, J. Bauer, H. Paetzelt, C. Sturm, and U. Teschner, “Growth of β-Ga2O3 on Al2O3 and GaAs using metal-organic vapor-phase epitaxy,” *Phys. status solidi*, vol. 206, no. 2, pp. 243–249, 2009.
[56] J. Robertson and B. Falabretti, “Electronic structure of transparent conducting oxides,” in *Handbook of Transparent Conductors*, Springer, 2011, pp. 27–50.
[57] S. B. Zhang, S.-H. Wei, and A. Zunger, “A phenomenological model for systematization and prediction of doping limits in II-VI and I-III-VI2 compounds,” *J. Appl. Phys.*, vol. 83, no. 6, pp. 3192–3196, 1998.
[58] N. Suzuki, S. Ohira, M. Tanaka, T. Sugawara, K. Nakajima, and T. Shishido, “Fabrication and characterization of transparent conductive Sn-doped β-Ga2O3 single crystal,” *Phys. status solidi*, vol. 4, no. 7, pp. 2310–2313, 2007.
[59] S. I. Maximenko, L. Mazeina, Y. N. Picard, J. A. Freitas Jr, V. M. Bermudez, and S. M. Prokes, “Cathodoluminescence studies of the inhomogeneities in Sn-doped Ga2O3 nanowires,” *Nano Lett.*, vol. 9, no. 9, pp. 3245–3251, 2009.
[60] E. G. Víllora, K. Shimamura, Y. Yoshikawa, T. Ujiie, and K. Aoki, “Electrical conductivity and carrier concentration control in ß-Ga 2 O 3 by Si doping,” *Appl. Phys. Lett.*, vol. 92, p. 202120, 2008.

[61] D. Gogova, G. Wagner, M. Baldini, M. Schmidbauer, K. Irmscher, R. Schewski, Z. Galazka, M. Albrecht, and R. Fornari, "Structural properties of Si-doped β-Ga 2 O 3 layers grown by MOVPE," *J. Cryst. Growth*, vol. 401, pp. 665–669, 2014.
[62] L. L. Liu, M. K. Li, D. Q. Yu, J. Zhang, H. Zhang, C. Qian, and Z. Yang, "Fabrication and characteristics of N-doped β-Ga2O3 nanowires," *Appl. Phys. A*, vol. 98, no. 4, pp. 831–835, 2010.
[63] Y. Tomm, J. M. Ko, a Yoshikawa, and T. Fukuda, "Floating zone growth of beta-Ga2O3: A new window material for optoelectronic device applications," *Sol. Energy Mater. Sol. Cells*, vol. 66, no. 1–4, pp. 369–374, 2001.
[64] H. Kawazoe, H. Yanagi, K. Ueda, and H. Hosono, "Transparent p-type conducting oxides: design and fabrication of pn heterojunctions," *Mrs Bull.*, vol. 25, no. 8, pp. 28–36, 2000.
[65] W. Guo, Y. Guo, H. Dong, and X. Zhou, "Tailoring the electronic structure of β-Ga2O3 by non-metal doping from hybrid density functional theory calculations," *Phys. Chem. Chem. Phys.*, vol. 17, pp. 5817–5825, 2015.
[66] F. P. Sabino, L. N. de Oliveira, and J. L. F. Da Silva, "Role of atomic radius and d-states hybridization in the stability of the crystal structure of M 2 O 3 (M= Al, Ga, In) oxides," *Phys. Rev. B*, vol. 90, no. 15, p. 155206, 2014.
[67] D. D. Edwards, P. E. Folkins, and T. O. Mason, "Phase Equilibria in the Ga2O3In2O3 System," *J. Am. Ceram. Soc.*, vol. 80, no. 1, pp. 253–257, 1997.
[68] A. F. Pasquevich, M. Uhrmacher, L. Ziegeler, and K. P. Lieb, "Hyperfine interactions of Cd 111 in Ga 2 O 3," *Phys. Rev. B*, vol. 48, no. 14, p. 10052, 1993.
[69] L. Binet, G. Gauthier, C. Vigreux, and D. Gourier, "Electron magnetic resonance and optical properties of Ga 2− 2x In 2x O 3 solid solutions," *J. Phys. Chem. Solids*, vol. 60, no. 10, pp. 1755–1762, 1999.
[70] A. Wang, N. L. Edleman, J. R. Babcock, T. J. Marks, M. A. Lane, P. R. Brazis, and C. R. Kannewurf, "Growth, microstructure, charge transport, and transparency of random polycrystalline and heteroepitaxial metalorganic chemical vapor deposition-derived gallium–indium–oxide thin films," *J. Mater. Res.*, vol. 17, no. 12, pp. 3155–3162, 2002.
[71] T. Oshima and S. Fujita, "Properties of Ga2O3-based (Inx Ga1–x) 2O3 alloy thin films grown by molecular beam epitaxy," *Phys. status solidi*, vol. 5, no. 9, pp. 3113–3115, 2008.
[72] W.-T. Lin, C.-Y. Ho, Y.-M. Wang, K.-H. Wu, and W.-Y. Chou, "Tunable growth of (Ga x In 1− x) 2 O 3 nanowires by water vapor," *J. Phys. Chem. Solids*, vol. 73, no. 7, pp. 948–952, 2012.
[73] T. Oshima, T. Okuno, N. Arai, Y. Kobayashi, and S. Fujita, "β-Al2xGa2-2xO3 Thin Film Growth by Molecular Beam Epitaxy," *Jpn. J. Appl. Phys.*, vol. 48, no. 7R, p. 70202, 2009.
[74] H. Ito, K. Kaneko, and S. Fujita, "Growth and band gap control of corundum-structured α-(AlGa) 2O3 thin films on sapphire by spray-assisted mist chemical vapor deposition," *Jpn. J. Appl. Phys.*, vol. 51, no. 10R, p. 100207, 2012.
[75] T. Kamimura, K. Sasaki, M. H. Wong, D. Krishnamurthy, A. Kuramata, T. Masui, S. Yamakoshi, and M. Higashiwaki, "Band alignment and electrical properties of Al2O3/β-Ga2O3 heterojunctions," *Appl. Phys. Lett.*, vol. 104, no. 19, p. 192104, 2014.

[76] Y. Hori, C. Mizue, and T. Hashizume, “Process conditions for improvement of electrical properties of Al2O3/n-GaN structures prepared by atomic layer deposition,” *Jpn. J. Appl. Phys.*, vol. 49, no. 8R, p. 80201, 2010.
[77] M. T. Nichols, W. Li, D. Pei, G. A. Antonelli, Q. Lin, S. Banna, Y. Nishi, and J. L. Shohet, “Measurement of bandgap energies in low-k organosilicates,” *J. Appl. Phys.*, vol. 115, no. 9, p. 94105, 2014.
[78] A. Y. Cho, “Film deposition by molecular-beam techniques,” *J. Vac. Sci. Technol.*, vol. 8, no. 5, pp. S31–S38, 1971.
[79] A. Y. Cho and J. R. Arthur, “Molecular beam epitaxy,” *Prog. solid state Chem.*, vol. 10, pp. 157–191, 1975.
[80] D. G. Schlom, L. Chen, X. Pan, A. Schmehl, and M. A. Zurbuchen, “A thin film approach to engineering functionality into oxides,” *J. Am. Ceram. Soc.*, vol. 91, no. 8, pp. 2429–2454, 2008.
[81] M. Henini, *Molecular beam epitaxy: from research to mass production*. Newnes, 2012.
[82] R. F. C. Farrow, *Molecular beam epitaxy: applications to key materials*. Elsevier, 1995.
[83] A. A. Demkov and A. B. Posadas, *Integration of functional oxides with semiconductors*. Springer, 2014.
[84] C. E. C. Wood, D. Desimone, K. Singer, and G. W. Wicks, “Magnesium-and calcium-doping behavior in molecular-beam epitaxial III-V compounds,” *J. Appl. Phys.*, vol. 53, no. 6, pp. 4230–4235, 1982.
[85] E. H. C. Parker, *The technology and physics of molecular beam epitaxy*. Plenum Press New York, 1985.
[86] T. Y. Kometani and W. Wiegmann, “Measurement of Ga and Al in a molecular-beam epitaxy chamber by atomic absorption spectrometry (AAS),” *J. Vac. Sci. Technol.*, vol. 12, no. 4, pp. 933–936, 1975.
[87] D. M. Mattox, “Handbook of Physical Vapor Deposition (PVD) Processing, Film Formation, Adhesion, Surface Preparation and Contamination Control, 1998.” and.
[88] M. N. R. Ashfold, F. Claeyssens, G. M. Fuge, and S. J. Henley, “Pulsed laser ablation and deposition of thin films,” *Chem. Soc. Rev.*, vol. 33, no. 1, pp. 23–31, 2004.
[89] R. Kelly, A. Miotello, D. B. Chrisey, and G. K. Hubler, “Pulsed Laser Deposition of Thin Films,” *by DB Chrisey GK Hubler (Wiley, New York, 1994) p*, vol. 55, 1994.
[90] X. D. Wu, T. Venkatesan, A. Inam, X. X. Xi, Q. Li, W. L. McLean, C. C. Chang, D. M. Hwang, R. Ramesh, and L. Nazar, “Pulsed Laser Deposition of High T c Superconducting thin Films: Present and Future,” *MRS Online Proc. Libr. Arch.*, vol. 191, 1990.
[91] D. Dijkkamp, T. Venkatesan, X. D. Wu, S. A. Shaheen, N. Jisrawi, Y. H. Min-Lee, W. L. McLean, and M. Croft, “Preparation of Y-Ba-Cu oxide superconductor thin films using pulsed laser evaporation from high T c bulk material,” *Appl. Phys. Lett.*, vol. 51, no. 8, pp. 619–621, 1987.
[92] “Solutions | PASCAL CO., LTD.” [Online]. Available: http://www.pascal-co-ltd.co.jp/solutions/index.html. [Accessed: 07-Jun-2017].

[93] M. G. Norton and C. B. Carter, “On the optimization of the laser ablation process for the deposition of YBa 2 Cu 3 O 7− δ thin films,” *Phys. C Supercond.*, vol. 172, no. 1, pp. 47–56, 1990.
[94] A. Ichimiya and P. I. Cohen, *Reflection high-energy electron diffraction*. Cambridge University Press, 2004.
[95] J. H. Haeni, C. D. Theis, and D. G. Schlom, “RHEED intensity oscillations for the stoichiometric growth of SrTiO 3 thin films by reactive molecular beam epitaxy,” *J. Electroceramics*, vol. 4, no. 2, pp. 385–391, 2000.
[96] I. Bozovic and J. N. Eckstein, “Analysis of Growing Films of Complex Oxides by RHEED.,” *Mrs Bull.*, vol. 20, no. 5, pp. 32–38, 1995.
[97] S. A. Chambers, “Epitaxial growth and properties of thin film oxides,” *Surf. Sci. Rep.*, vol. 39, no. 5, pp. 105–180, 2000.
[98] B. D. Cullity, “Element of X-ray Diffraction, Addison-Wesley Reading,” *MA Google Sch.*, 1978.
[99] J. B. Nelson and D. P. Riley, “An experimental investigation of extrapolation methods in the derivation of accurate unit-cell dimensions of crystals,” *Proc. Phys. Soc.*, vol. 57, no. 3, p. 160, 1945.
[100] B. E. Warren, “X-ray Diffraction. Dover,” *New York*, vol. 253, 1990.
[101] S. Hüfner, *Photoelectron spectroscopy: principles and applications*. Springer Science & Business Media, 2013.
[102] P. Van der Heide, *X-ray photoelectron spectroscopy: an introduction to principles and practices*. John Wiley & Sons, 2011.
[103] “EAgLE.” [Online]. Available: http://www.eagle-regpot.eu/EAgLE-Equipment_XPS.html. [Accessed: 07-Jun-2017].
[104] J. H. Thomas III, C. E. Bryson III, and T. R. Pampalone, “X-ray photoelectron spectroscopy surface charge buildup used to study residue in deep features on integrated circuits,” *J. Vac. Sci. Technol. B Microelectron. Process. Phenom.*, vol. 6, no. 4, pp. 1081–1086, 1988.
[105] J. H. Thomas, C. E. Bryson, and T. R. Pampalone, “X-ray photoelectron spectroscopy and surface charge build-up used to study residue on aluminum contacts on integrated circuits,” *Surf. interface Anal.*, vol. 14, no. 1-2, pp. 39–45, 1989.
[106] W. Priyantha, G. Radhakrishnan, R. Droopad, and M. Passlack, “In-situ XPS and RHEED study of gallium oxide on GaAs deposition by molecular beam epitaxy,” *J. Cryst. Growth*, vol. 323, no. 1, pp. 103–106, 2011.
[107] R. Waser, *Nanoelectronics and information technology*. John Wiley & Sons, 2012.
[108] “Scanning Probe Microscopy.” [Online]. Available: http://www.solid.unito.it/Strumentazione/SPM/SPM_index.html. [Accessed: 08-Jun-2017].
[109] S. Morita, F. J. Giessibl, E. Meyer, and R. Wiesendanger, *Noncontact atomic force microscopy*, vol. 3. Springer, 2015.
[110] G. Binnig, C. F. Quate, and C. Gerber, “Atomic force microscope,” *Phys. Rev. Lett.*, vol. 56, no. 9, p. 930, 1986.
[111] F. J. Giessibl, “Advances in atomic force microscopy,” *Rev. Mod. Phys.*, vol. 75, no. 3, p. 949, 2003.

[112] G. M. McClelland, R. Erlandsson, and S. Chiang, “Atomic force microscopy: General principles and a new implementation,” in *Review of Progress in Quantitative Nondestructive Evaluation*, Springer, 1987, pp. 1307–1314.
[113] J. A. Woollam, B. D. Johs, C. M. Herzinger, J. N. Hilfiker, R. A. Synowicki, and C. L. Bungay, “Overview of variable-angle spectroscopic ellipsometry (VASE): I. Basic theory and typical applications,” in *Optical Metrology*, 1999, pp. 3–28.
[114] H. G. Tompkins and W. A. McGahan, *Spectroscopic ellipsometry and reflectometry: a user’s guide*. Wiley, 1999.
[115] J. B. de Lima Filho and Á. A. Hidalgo, “Film thickness by interference pattern and optical characterization of polyaniline by spectroscopic ellipsometry,” *Synth. Met.*, vol. 223, pp. 80–86, 2017.
[116] H. Fujiwara, *Spectroscopic ellipsometry: principles and applications*. John Wiley & Sons, 2007.
[117] D. E. Aspnes, J. B. Theeten, and F. Hottier, “Investigation of effective-medium models of microscopic surface roughness by spectroscopic ellipsometry,” *Phys. Rev. B*, vol. 20, no. 8, p. 3292, 1979.
[118] G. E. Jellison Jr, “Spectroscopic ellipsometry data analysis: measured versus calculated quantities,” *Thin Solid Films*, vol. 313, pp. 33–39, 1998.
[119] G. E. Jellison, “Data analysis for spectroscopic ellipsometry,” *Thin Solid Films*, vol. 234, no. 1–2, pp. 416–422, 1993.
[120] H.-H. Perkampus, H.-C. Grinter, and T. L. Threlfall, *UV-VIS Spectroscopy and its Applications*. Springer, 1992.
[121] L. Guo, X. Shen, G. Zhu, and K. Chen, “Preparation and gas-sensing performance of In 2 O 3 porous nanoplatelets,” *Sensors Actuators B Chem.*, vol. 155, no. 2, pp. 752–758, 2011.
[122] P. Vogt and O. Bierwagen, “Reaction kinetics and growth window for plasma-assisted molecular beam epitaxy of Ga2O3: Incorporation of Ga vs. Ga2O desorption,” *Appl. Phys. Lett.*, vol. 108, no. 7, p. 72101, 2016.
[123] E. Korhonen, F. Tuomisto, D. Gogova, G. Wagner, M. Baldini, Z. Galazka, R. Schewski, and M. Albrecht, “Electrical compensation by Ga vacancies in Ga2O3 thin films,” *Appl. Phys. Lett.*, vol. 106, no. 24, p. 242103, 2015.
[124] S. Raghavan, T. Schumann, H. Kim, J. Y. Zhang, T. A. Cain, and S. Stemmer, “High-mobility BaSnO3 grown by oxide molecular beam epitaxy,” *APL Mater.*, vol. 4, no. 1, p. 16106, 2016.
[125] R. Droopad, K. Rajagopalan, J. Abrokwah, L. Adams, N. England, D. Uebelhoer, P. Fejes, P. Zurcher, and M. Passlack, “Development of GaAs-based MOSFET using molecular beam epitaxy,” *J. Cryst. Growth*, vol. 301, pp. 139–144, 2007.
[126] S. Müller, H. von Wenckstern, D. Splith, F. Schmidt, and M. Grundmann, “Control of the conductivity of Si-doped β-Ga2O3 thin films via growth temperature and pressure,” *Phys. status solidi*, vol. 211, no. 1, pp. 34–39, 2014.
[127] M. Rebien, W. Henrion, M. Hong, J. P. Mannaerts, and M. Fleischer, “Optical properties of gallium oxide thin films,” *Appl. Phys. Lett.*, vol. 81, no. 2, pp. 250–252, 2002.
[128] T. Oshima, T. Okuno, and S. Fujita, “Ga2O3 thin film growth on c-plane sapphire substrates by molecular beam epitaxy for deep-ultraviolet photodetectors,” *Jpn. J. Appl. Phys.*, vol. 46, no. 11R, p. 7217, 2007.

[129] G. Sinha, K. Adhikary, and S. Chaudhuri, “Effect of annealing temperature on structural transformation of gallium based nanocrystalline oxide thin films and their optical properties,” *Opt. Mater. (Amst).*, vol. 29, no. 6, pp. 718–722, 2007.
[130] S. S. Kumar, E. J. Rubio, M. Noor-A-Alam, G. Martinez, S. Manandhar, V. Shutthanandan, S. Thevuthasan, and C. V Ramana, “Structure, morphology, and optical properties of amorphous and nanocrystalline gallium oxide thin films,” *J. Phys. Chem. C*, vol. 117, no. 8, pp. 4194–4200, 2013.
[131] F. K. Shan, G. X. Liu, W. J. Lee, G. H. Lee, I. S. Kim, and B. C. Shin, “Structural, electrical, and optical properties of transparent gallium oxide thin films grown by plasma-enhanced atomic layer deposition,” *J. Appl. Phys.*, vol. 98, no. 2, p. 23504, 2005.
[132] M. Orita, H. Ohta, M. Hirano, and H. Hosono, “Deep-ultraviolet transparent conductive beta-Ga2O3 thin films,” *Appl. Phys. Lett.*, vol. 77, p. 4166, 2000.
[133] Y. Lv, J. Ma, W. Mi, C. Luan, Z. Zhu, and H. Xiao, “Characterization of β-Ga 2 O 3 thin films on sapphire (0001) using metal-organic chemical vapor deposition technique,” *Vacuum*, vol. 86, no. 12, pp. 1850–1854, 2012.
[134] D. H. A. Blank, M. E. Bijlsma, R. Moerman, H. Rogalla, F. J. B. Stork, and A. Roshko, “Surface roughness and height-height correlations dependence on thickness of YBaCuO thin films,” *J. Alloys Compd.*, vol. 251, no. 1–2, pp. 31–33, 1997.
[135] C. V Ramana, R. J. Smith, O. M. Hussain, and C. M. Julien, “On the growth mechanism of pulsed-laser deposited vanadium oxide thin films,” *Mater. Sci. Eng. B*, vol. 111, no. 2, pp. 218–225, 2004.
[136] F. Zhang, K. Saito, T. Tanaka, M. Nishio, and Q. Guo, “Wide bandgap engineering of (GaIn) 2 O 3 films,” *Solid State Commun.*, vol. 186, pp. 28–31, 2014.
[137] B. W. Krueger, C. S. Dandeneau, E. M. Nelson, S. T. Dunham, F. S. Ohuchi, and M. A. Olmstead, “Variation of Band Gap and Lattice Parameters of β−(AlxGa1−x) 2O3 Powder Produced by Solution Combustion Synthesis,” *J. Am. Ceram. Soc.*, vol. 99, no. 7, pp. 2467–2473, 2016.
[138] F. Zhang, K. Saito, T. Tanaka, M. Nishio, M. Arita, and Q. Guo, “Wide bandgap engineering of (AlGa) 2O3 films,” *Appl. Phys. Lett.*, vol. 105, no. 16, p. 162107, 2014.
[139] S. Fujita and K. Kaneko, “Epitaxial growth of corundum-structured wide band gap III-oxide semiconductor thin films,” *J. Cryst. Growth*, vol. 401, pp. 588–592, 2014.
[140] T. Minami, Y. Takeda, T. Kakumu, S. Takata, and I. Fukuda, “Preparation of highly transparent and conducting Ga2O3–In2O3 films by direct current magnetron sputtering,” *J. Vac. Sci. Technol. A Vacuum, Surfaces, Film.*, vol. 15, no. 3, pp. 958–962, 1997.
[141] J. M. Phillips, J. Kwo, G. A. Thomas, S. A. Carter, R. J. Cava, S. Y. Hou, J. J. Krajewski, J. H. Marshall, W. F. Peck, and D. H. Rapkine, “Transparent conducting thin films of GaInO3,” *Appl. Phys. Lett.*, vol. 65, no. 1, pp. 115–117, 1994.

[142] S. W. Kaun, F. Wu, and J. S. Speck, "β-(AlxGa1− x) 2O3/Ga2O3 (010) heterostructures grown on β-Ga2O3 (010) substrates by plasma-assisted molecular beam epitaxy," *J. Vac. Sci. Technol. A*, vol. 33, no. 4, p. 41508, 2015.
[143] Q. Feng, X. Li, G. Han, L. Huang, F. Li, W. Tang, J. Zhang, and Y. Hao, "(AlGa) 2 O 3 solar-blind photodetectors on sapphire with wider bandgap and improved responsivity," *Opt. Mater. Express*, vol. 7, no. 4, pp. 1240–1248, 2017.
[144] F. Yang, J. Ma, C. Luan, L. Kong, and Z. Zhu, "Structural and Photoluminescence Properties of Ga2-2xIn2xO3 Films Prepared on Alpha-Al2O3 (0001) by MOCVD," in *Photonics and Optoelectronics (SOPO), 2011 Symposium on*, 2011, pp. 1–5.
[145] C. Janowitz, V. Scherer, M. Mohamed, A. Krapf, H. Dwelk, R. Manzke, Z. Galazka, R. Uecker, K. Irmscher, R. Fornari, M. Michling, D. Schmeißer, J. R. Weber, J. B. Varley, and C. G. Van De Walle, "Experimental electronic structure of In2O3 and Ga2O3," *New J. Phys.*, vol. 13, 2011.
[146] Y. Kokubun, T. Abe, and S. Nakagomi, "Sol–gel prepared (Ga1− xInx) 2O3 thin films for solar-blind ultraviolet photodetectors," *Phys. status solidi*, vol. 207, no. 7, pp. 1741–1745, 2010.
[147] V. I. Vasyltsiv, Y. I. Rym, and Y. M. Zakharko, "Optical absorption and photoconductivity at the band edge of β-Ga2− xInxO3," *Phys. status solidi*, vol. 195, no. 2, pp. 653–658, 1996.
[148] S. P. Chang, S.-J. Chang, Y. Z. Chiou, C. Y. Lu, T. K. Lin, Y. C. Lin, C. F. Kuo, and H.-M. Chang, "ZnO photoconductive sensors epitaxially grown on sapphire substrates," *Sensors Actuators A Phys.*, vol. 140, no. 1, pp. 60–64, 2007.
[149] M. S. Rahman, S. Ghose, L. Hong, P. Dhungana, A. Fahami, J. R. Gatabi, J. S. Rojas-Ramirez, A. Zakhidov, R. F. Klie, and R. K. Pandey, "Integration of BiFeO 3/La 0.7 Sr 0.3 MnO 3 heterostructures with III–V semiconductors for low-power non-volatile memory and multiferroic field effect transistors," *J. Mater. Chem. C*, vol. 4, no. 43, pp. 10386–10394, 2016.
[150] S. Kundu, M. Clavel, P. Biswas, B. Chen, H.-C. Song, P. Kumar, N. N. Halder, M. K. Hudait, P. Banerji, and M. Sanghadasa, "Lead-free epitaxial ferroelectric material integration on semiconducting (100) Nb-doped SrTiO3 for low-power non-volatile memory and efficient ultraviolet ray detection," *Sci. Rep.*, vol. 5, p. 12415, 2015.
[151] F.-C. Chiu, "A review on conduction mechanisms in dielectric films," *Adv. Mater. Sci. Eng.*, vol. 2014, 2014.
[152] S. M. Jilani, T. D. Gamot, P. Banerji, and S. Chakraborty, "Studies on resistive switching characteristics of aluminum/graphene oxide/semiconductor nonvolatile memory cells," *Carbon N. Y.*, vol. 64, pp. 187–196, 2013.
[153] D. Y. Guo, Z. P. Wu, Y. H. An, X. C. Guo, X. L. Chu, C. L. Sun, L. H. Li, P. G. Li, and W. H. Tang, "Oxygen vacancy tuned Ohmic-Schottky conversion for enhanced performance in β-Ga2O3 solar-blind ultraviolet photodetectors," *Appl. Phys. Lett.*, vol. 105, no. 2, p. 23507, 2014.
[154] A. S. Pratiyush, S. Krishnamoorthy, S. V. Solanke, Z. Xia, R. Muralidharan, S. Rajan, and D. N. Nath, "High Responsivity in Molecular Beam Epitaxy (MBE) grown\b {eta}-Ga2O3 Metal Semiconductor Metal (MSM) Solar Blind Deep-UV Photodetector," *arXiv Prepr. arXiv1702.04470*, 2017.

[155] Y. Qu, Z. Wu, M. Ai, D. Guo, Y. An, H. Yang, L. Li, and W. Tang, “Enhanced Ga 2 O 3/SiC ultraviolet photodetector with graphene top electrodes,” *J. Alloys Compd.*, vol. 680, pp. 247–251, 2016.
[156] W. Cui, X. L. Zhao, Y. H. An, D. Y. Guo, X. Y. Qing, Z. P. Wu, P. G. Li, L. H. Li, C. Cui, and W. H. Tang, “Direct charge carrier injection into Ga2O3 thin films using an In2O3 cathode buffer layer: their optical, electrical and surface state properties,” *J. Phys. D. Appl. Phys.*, vol. 50, no. 13, p. 135109, 2017.
[157] L.-C. Chen, C.-H. Tien, and W.-C. Liao, “A phosphor-free white light-emitting diode using In2O3: Tb transparent conductive light converter,” *J. Phys. D. Appl. Phys.*, vol. 44, no. 16, p. 165101, 2011.
[158] H. Wang, D. Zhang, Y. Luo, X. Zhao, F. Luo, L. Huang, Y. Li, and W. Wang, “Fabrication and study of laser-damage-resistant transparent conductive W-doped In2O3 films,” *J. Phys. D. Appl. Phys.*, vol. 44, no. 21, p. 215101, 2011.
[159] J. Gan, X. Lu, J. Wu, S. Xie, T. Zhai, M. Yu, Z. Zhang, Y. Mao, S. C. I. Wang, and Y. Shen, “Oxygen vacancies promoting photoelectrochemical performance of In2O3 nanocubes,” *Sci. Rep.*, vol. 3, p. 1021, 2013.